Part II

Rotor Flap-Lag

pp. 69-151

Expanded Figures - Geometry

$$\psi = \Omega t$$
$$\dot{\psi} = \Omega$$

$$R\cos\beta$$
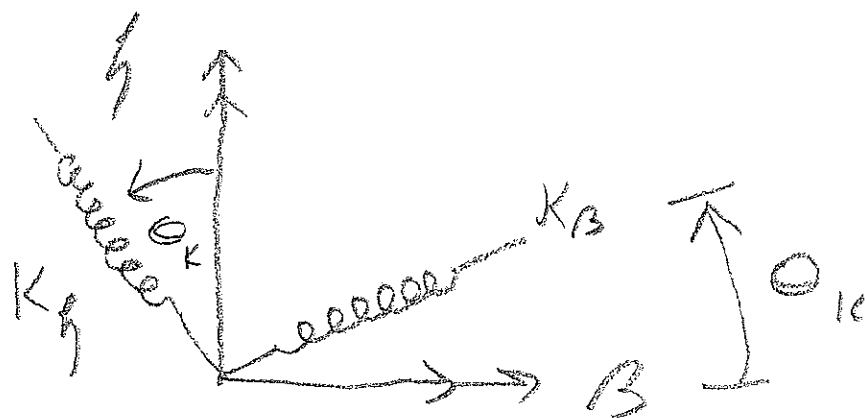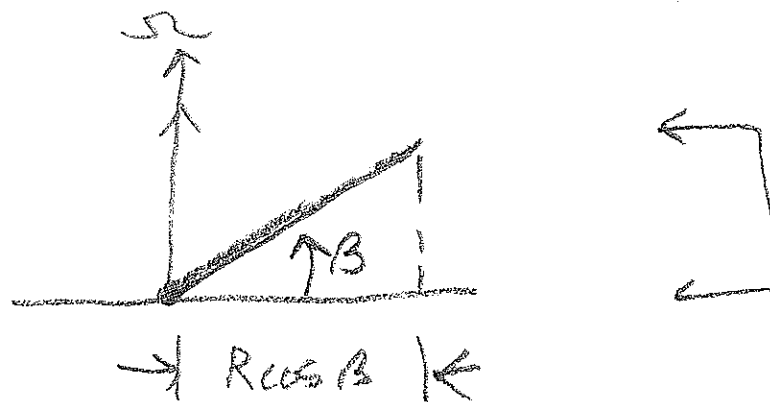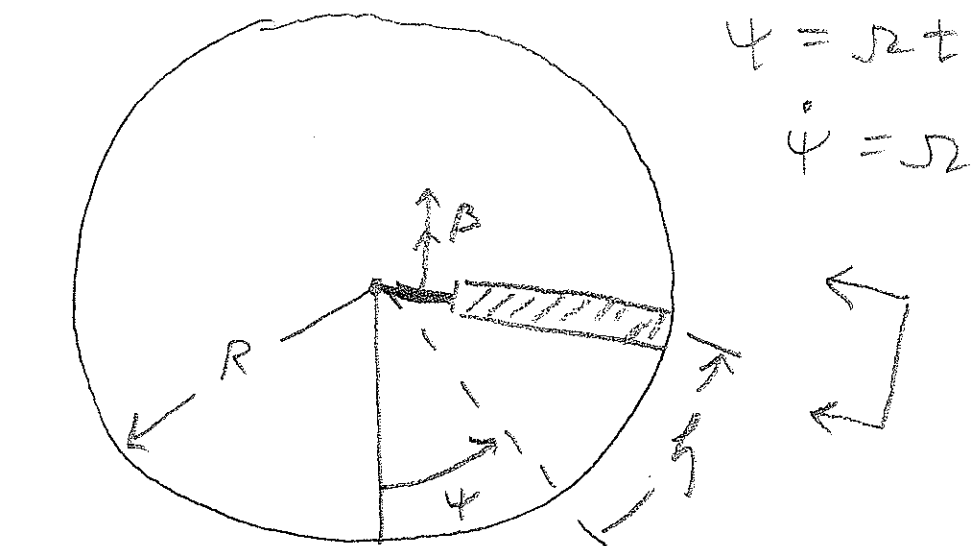
$$K_B, K_\eta \text{ torsional springs}$$

69b

FLAP-LAG EQUATIONS

$$T = \tfrac{1}{2}I \left[\left(\dot{\psi} + \dot{\zeta} \right)^2 \cos^2 \beta + \dot{\beta}^2 \right]$$

$$V = \tfrac{1}{2}K_\beta \left[(\beta - \beta_{pc}) \cos \theta_k - \zeta \sin \theta_k \right]^2$$

$$+ \tfrac{1}{2}K_\zeta \left[\zeta \cos \theta_k + (\beta - \beta_{pc}) \sin \theta_k \right]^2$$

$$\delta W = M_\beta \delta\beta + M_\zeta \cos\beta \, \delta\zeta$$

$$\frac{\partial T}{\partial \dot{\beta}} = I\dot{\beta} \qquad \frac{\mathrm{d}}{\mathrm{d}t}\frac{\partial T}{\partial \dot{\beta}} = I\ddot{\beta}$$

$$\frac{\mathrm{d}T}{\mathrm{d}\beta} = -I \left(\Omega + \dot{\zeta} \right)^2 \cos\beta \sin\beta$$

$$\frac{\mathrm{d}T}{\mathrm{d}\dot{\zeta}} = I \left(\Omega + \dot{\zeta} \right) \cos^2 \beta, \qquad \frac{\partial T}{\partial \zeta} = 0$$

$$\frac{\mathrm{d}}{\mathrm{d}t}\frac{\mathrm{d}T}{\mathrm{d}\dot{\zeta}} = I\ddot{\zeta}\cos^2\beta - 2I\dot{\beta}\cos\beta\sin\beta \left(\Omega + \dot{\zeta} \right)$$

$$\frac{\partial V}{\partial \beta} = K_\beta \left[(\beta - \beta_{pc})\cos^2\theta_k - \zeta\cos\theta_k\sin\theta_k \right] + K_\zeta \left[(\beta - \beta_{pc})\sin^2\theta_k + \zeta\cos\theta_k\sin\theta_k \right]$$

$$\frac{\partial V}{\partial \zeta} = K_\beta \left[-(\beta - \beta_{pc})\cos\theta_k\sin\theta_k - \zeta\sin^2\theta_k \right] + K_\zeta \left[(\beta - \beta_{pc})\cos\theta_k\sin\theta_k + \zeta\cos^2\theta_k \right]$$

$$\frac{\mathrm{d}}{\mathrm{d}t}\frac{\partial T}{\partial \dot{\beta}} - \frac{\partial T}{\partial \beta} + \frac{\partial V}{\partial \beta} = M_\beta$$

$$\frac{\mathrm{d}}{\mathrm{d}t}\frac{\partial T}{\partial \dot{\zeta}} - \frac{\partial T}{\partial \zeta} + \frac{\partial V}{\partial \zeta} = M_\zeta \cos\beta$$

$$I\ddot{\beta} + I\left(\Omega + \dot{\zeta}\right)^2 \cos\beta\sin\beta + \beta\left[K_\beta\cos^2\theta_k + K_\zeta\sin^2\theta_k\right]$$
$$- \beta_{pc}\left[K_\beta\cos^2\theta_k + K_\zeta\sin^2\theta_k\right] + \zeta\cos\theta_k\sin\theta_k\left[-K_\beta + K_\zeta\right] = M_\beta$$

$$I\ddot{\zeta}\cos^2\beta - 2\Omega I\dot{\beta}\cos\beta\sin\beta + \zeta\left[K_\beta\sin^2\theta_k + K_\zeta\cos^2\theta_k\right]$$
$$+ (-\beta_{ps} + \beta)\cos\theta_k\sin\theta_k\left[-K_\beta + K_\zeta\right] = M_\zeta\cos\beta$$

Linearize and non-dimensionalize
$$\beta = \beta_o + \overline{\beta}, \quad \zeta = \zeta_o + \overline{\zeta}$$
$$\cos\beta = 1, \quad \sin\beta = \beta_o + \overline{\beta}, \quad \sin\theta_k = R\theta, \quad \cos\theta_k = 1$$
$$1 + \frac{K_\beta}{\Omega^2 I} = p^2, \quad \frac{K_\zeta}{\Omega^2 I} = \omega_\zeta^2, \quad \Delta = R\theta\left(\omega_\zeta^2 - p^2 + 1\right)$$

$$-\begin{Bmatrix} \omega_\beta^2 \\ \Delta \end{Bmatrix}\beta_{pc} + \begin{bmatrix} p^2 & \Delta \\ \Delta & \omega_\zeta^2 \end{bmatrix}\begin{Bmatrix} \beta_o \\ \zeta_o \end{Bmatrix} = \begin{Bmatrix} \overline{M}_\beta \\ \overline{M}_\zeta \end{Bmatrix}$$
steady part of nondimensional Loads
$$\begin{Bmatrix} \overset{**}{\overline{\beta}} \\ \overset{**}{\overline{\zeta}} \end{Bmatrix} + \begin{bmatrix} 0 & 2\beta_o \\ -2\beta_o & 0 \end{bmatrix}\begin{Bmatrix} \overset{*}{\overline{\beta}} \\ \overset{*}{\overline{\zeta}} \end{Bmatrix} + \begin{bmatrix} p^2 & \Delta \\ \Delta & \omega_\zeta^2 \end{bmatrix}\begin{Bmatrix} \overline{\beta} \\ \overline{\zeta} \end{Bmatrix} = \begin{Bmatrix} \widetilde{M}_\beta \\ \widetilde{M}_\zeta \end{Bmatrix}$$
(perturbation loads)

$$\overline{M}_\beta + \widetilde{M}_\beta = \int_0^1 \frac{F_\beta R^2}{\Omega^2 I}r\mathrm{d}r$$

$$\overline{M}_\zeta + \widetilde{M}_\zeta = \int_0^1 \frac{F_\zeta R^2}{\Omega^2 I_y}r\mathrm{d}r$$

$$\sqcup_T = \left(\Omega + \dot{\zeta}\right)x\cos\beta, \quad \frac{\sqcup_T}{\Omega R} = \left(1 + \overset{*}{\zeta}\right)r$$

$$\sqcup_p = v_i + \dot{\beta}x, \quad \frac{\sqcup_p}{\Omega R} = \left(\phi + \overset{*}{\beta}\right)r$$

$$\phi \approx \frac{\sigma a}{12}\left[-1 + \sqrt{1 + \frac{24\theta}{\sigma a}}\right]$$

71

$$F_\beta = \frac{\rho ac}{2}\left[U_T^2\theta - U_p U_T\right] \qquad \text{order } \epsilon$$

$$F_\zeta = -\frac{\rho ac}{2}\left[U_T^2\frac{C_D}{a} + U_p\,U_T\,\theta - U_p^2\right] \qquad \text{order } \epsilon^2$$

$$\overline{M}_\beta = \frac{\gamma}{8}\left(\theta - \phi\right), \quad \overline{M}_\zeta = -\frac{\gamma}{8}\left(\frac{C_D}{a} + \theta\phi - \phi^2\right)$$

$$\widetilde{M}_\beta = \frac{\gamma}{8}\left(2\overset{*}{\zeta}\theta - \overset{*}{\zeta}\phi - \overset{*}{\beta}\right)$$

$$\widetilde{M}_\zeta = -\frac{\gamma}{8}\left(2\overset{*}{\zeta}\frac{C_D}{a} + \overset{*}{\zeta}\theta\phi + \theta\overset{*}{\beta} - 2\phi\overset{*}{\beta}\right)$$

$$\text{static}: \quad \beta_o = \frac{p^2-1}{p^2}\beta_{pc} + \frac{\gamma}{8p^2}\left(\theta - \phi\right)$$

$$\zeta_o = \text{negligible}$$

Dynamic $\left(n = \frac{\gamma}{8}\right)$

$$\left\{\begin{matrix}\overset{**}{\overline{\beta}}\\\overline{\zeta}\end{matrix}\right\} + \begin{bmatrix} n & 2\beta_o - n\left(2\theta - \phi\right)\\ -2\beta_o + n\left(\theta - 2\phi\right) & 2\frac{C_D}{a}n + n\theta\phi\end{bmatrix}\left\{\begin{matrix}\overset{*}{\overline{\beta}}\\\overline{\zeta}\end{matrix}\right\} + \begin{bmatrix}p^2 & \Delta\\ \Delta & w_\zeta^2\end{bmatrix}\left\{\begin{matrix}\overline{\beta}\\\overline{\zeta}\end{matrix}\right\} = \left\{\begin{matrix}0\\0\end{matrix}\right\}$$

pitch-flap and pitch-lag coupling
Note: If $\theta \Rightarrow \theta_o + \theta_\beta\beta + \theta_\zeta\zeta$

$K_{11} = \overline{p}^2 \Rightarrow p^2 - \frac{\gamma}{8}\theta_\beta$

$K_{12} \Rightarrow \Delta - \frac{\gamma}{8}\theta_\zeta$

$K_{21} \Rightarrow \Delta + \frac{\gamma}{8}\phi\theta_\beta$

$K_{22} = \omega_\zeta^2 + \frac{\gamma}{8}\theta_\zeta\phi$

$$\boxed{\beta_o = \frac{\overline{p}^2 - 1}{\overline{p}^2}\beta_{pc} + \frac{\gamma}{8\overline{p}^2}\left(\theta_o - \phi\right)}$$

Linear Flap-Lag Dynamics of Hingeless Helicopter Rotor Blades in Hover

Robert A. Ormiston and **Dewey H. Hodges,**
Research Scientists
Ames Directorate
U. S. Army Air Mobility Research & Development Laboratory
Ames Research Center
Moffett Field, California

The linear stability characteristics of rotor blade flap-lag oscillations in the hovering flight condition are examined. The present study is focused on the effects of pre-cone, variable elastic coupling, pitch-lag coupling, and the aerodynamics of induced inflow. Together with an improved perturbation analysis for deriving the equations these factors are shown to significantly influence the flap-lag stability characteristics of hingeless rotor blades. Routh's criteria are used to derive several fundamental flap-lag stability relations, and emphasize the utility of simplified rotor blade modeling for understanding complex dynamic phenomena. In order to validate the approximate rigid blade equations, elastic blade modal equations are presented together with comparative solutions. The results indicate a high degree of accuracy for the approximate equations when the elastic coupling is included. Finally, the approximate equations are used to illustrate the influence of elastic coupling on the response characteristics of hingeless rotors.

NOMENCLATURE

a	=	two-dimensional lift curve slope
A, A_{approx}, C	=	induced flow parameters, Eqs. (7, 41).
b	=	number of blades
c	=	blade chord, ft
c_{d_0}	=	profile drag coefficient
$C_\beta, C_{\dot\beta}, C_\zeta, C_{\dot\zeta}$	=	lead moment coefficients
dD, dL, dF_z, dF_y	=	local lift and drag forces; flap and lead components, lb/ft
E	=	Young's modulus, lb/in^2
F	=	Routh's discriminant, Eq. (9)
$F_\beta, F_{\dot\beta}, F_\zeta, F_{\dot\zeta}$	=	flap moment coefficients
D	=	drag parameter $2c_{d_0}/a$
I	=	blade inertia, $1/3 mR^3$, slug-ft^2
I_1, I_2	=	blade section principal moments of inertia
K_{β_H}, K_{ζ_H}	=	flap and lead-lag spring rates at hub, ft-lb/rad, Fig. 14
K_{β_B}, K_{ζ_B}	=	flap and lead-lag spring rates at blade root, ft-lb/rad, Fig. 14
K_β, K_ζ	=	total flap and lead-lag hinge spring rates at $\theta = 0$, ft-lb/rad, Eq. (43)
K_{vv}, K_{ww}, K_{wv}	=	elastic blade stiffness parameters, Eqs. (56–58)
m	=	blade mass distribution, slug/ft
n	=	number of elastic blade flap and in-plane modes
$M_{\beta aero}, M_{\zeta aero}$	=	flap and lead aerodynamic moments, Eqs. (39, 40)
p, P, q	=	rotating flap and lead-lag frequency parameters, Eqs. (11, 25, 27, 51)
R	=	blade radius, ft; also, variable elastic coupling parameter, Eq. (47)
R_{vc}	=	elastic coupling parameter, Eq. (51)
s	=	Laplace transform variable, sec^{-1}
T	=	rotor blade tension, lb
u, v, w	=	displacements in x, y, z direction measured from undeformed positions, ft
U_P, U_T	=	relative normal and tangential airfoil velocities, fps, Eq. (34)
v_i	=	induced velocity, fps
V, V_T	=	velocity, velocity of blade tip, $R\Omega$, fps
V_n, W_n	=	generalized coordinates for modal equations
W	=	lead-lag frequency parameter, Eqs. (11, 25, 27)
x, y, z	=	rotating coordinates
z, Z	=	elastic coupling parameters, Eqs. (51, 25)
β	=	flapping angular displacement of blade measured from plane of rotation, rad
$\beta_{pc}, \beta_{pc_I}, \beta_{pc_w}$	=	pre-cone parameters, Eqs. (17, 18)
γ	=	Lock number, $\rho ac R^4/I$
Δ	=	elastic coupling parameter, Eq. (46)

2

73

ζ	=	inplane, or lead-lag angular displacement of blade, rad
η	=	Lock number parameter, $\gamma/8$
η_m	=	structural damping parameter
θ	=	blade pitch angle, rad
$\theta_{\min}$	=	minimum θ for neutral stability for given p
θ^*	=	absolute minimum θ for neutral stability
θ_ζ	=	kinematic pitch-lag coupling parameter
ξ	=	nondimensional radial coordinate, x/R
ρ	=	air density, slugs/ft³
σ	=	rotor solidity, $bc/\pi R$
σ_ζ	=	real part of inplane mode eigenvalue, sec^{-1}
ϕ, ϕ_i	=	inflow angle, $\phi = \tan^{-1} U_P/U_T$, $\phi_i = v_i/\Omega x$
ϕ_{v_n}, ϕ_{w_n}	=	mode shapes for modal equations
Ω	=	coordinate system angular velocity, rad/sec
ω	=	imaginary part of eigenvalue, rad/sec
$\omega_\beta, \omega_\zeta$	=	flap and lead-lag non-rotating frequency, Eq. (51), rad/sec
$(\dot{\ })$	=	$d(\ )/dt$
$(\ )'$	=	$\partial(\ )/\partial x$
$(\ )_0, \Delta(\ )$	=	steady state and perturbation variables
$(\bar{\ })$	=	nondimensionalized by R for lengths, V_r for velocities Ω for frequencies.

THE GROWING acceptance of hingeless rotors for conventional and compound helicopters has intensified the need for fundamental research on rotor blade stability. This is because the small aerodynamic and structural damping of the lead-lag motion can lead to unstable rotor blade oscillations. The lack of a lead-lag hinge and the desire for simplicity usually preclude the use of auxilliary viscous dampers which are normally used to augment damping of articulated rotor blades.

The fundamental stability characteristics of hingeless rotor blades can be studied by retaining only the flap and lead-lag degrees of freedom of a single blade. Several researchers have already studied this problem,[1-5] however, the subject of flap-lag stability is not yet adequately understood. In particular, the effects of aerodynamics, pre-cone, elastic coupling, and kinematic pitch-lag coupling were either not included, incorrectly derived, or not systematically investigated. In addition, in nearly all cases only simplified mechanical representations of fully elastic hingeless rotor blades such as centrally hinged rigid blades with spring restraint were employed.

The present study was therefore undertaken to address these factors in detail. In order to determine the accuracy of the approximate equations for centrally hinged, rigid blades used by previous investigators, the exact multimode elastic blade equations are also derived and results for both formulations compared. The analysis is restricted to the hover condition which greatly simplifies the problem by eliminating the periodic coefficients of the forward flight equations. Further simplification is obtained by excluding the torsional degree of freedom. Although torsional motion is important for rotor blade stability, its inclusion is beyond the scope of the present study.

BASIC FLAP-LAG EQUATIONS

The approximate perturbation equations derived in the Appendix for the centrally hinged rigid blade with spring restraint, may be used to examine the source of potentially destabilizing flap-lag coupling. The homogeneous equations for the basic configuration (without pre-cone or elastic coupling) can be written,

$$\begin{bmatrix} s^2 + F_{\dot\beta}s + F_\beta & -sF_\zeta \\ -sC_{\dot\beta} & s^2 + C_{\dot\zeta}s + C_\zeta \end{bmatrix} \begin{Bmatrix} \Delta\beta \\ \Delta\zeta \end{Bmatrix} = 0 \quad (1)$$

The coupling coefficients of interest are obtained from Eq. (50)

$$F_\zeta = \gamma/8(2\theta - A) - 2\beta_0 \quad (2)$$

$$C_{\dot\beta} = 2\beta_0 - \gamma/8(\theta - 2A) \quad (3)$$

where the coning

$$\beta_0 = [\gamma/8](\theta - A)/p^2, \quad p^2 = \bar\omega_\beta^2 + 1 \quad (4)$$

The first coefficient, F_ζ, combines the aerodynamic flap moment due to lead velocity with the opposing centrifugal flap moment due to centrifugal forces, $2\beta_0$. The second coefficient, $C_{\dot\beta}$, consists of a Coriolis lead moment due to flapping velocity opposed by a small aerodynamic moment. The product, $F_\zeta C_{\dot\beta}$ represents the potentially destabilizing flap-lag coupling. Approximating the induced inflow parameter A by $\theta/2$ (see below) yields the following simplified expression

$$F_\zeta C_{\dot\beta} = [(\gamma/8)\theta]^2[^3/_2 - 1/p^2]/p^2 \quad (5)$$

The destabilizing portion ($^3/_2$) is caused by the product of aerodynamic and Coriolis moments while the product of centrifugal and Coriolis moments ($1/p^2$) is stabilizing. Furthermore, the flap-lag coupling is proportional to θ^2 and is a maximum when $p = \sqrt{^4/_3}$. This flapping frequency is typical of present hingeless rotor helicopters. It may also be observed that flap-lag coupling exists for articulated rotors ($p = 1$, for zero flap hinge offset).

The induced inflow parameter A is defined in the Appendix, Eq. (41). The simple and useful approximation used above assumes that the induced inflow angle ϕ_i is given by one-half the blade pitch angle. Eq. (41) then
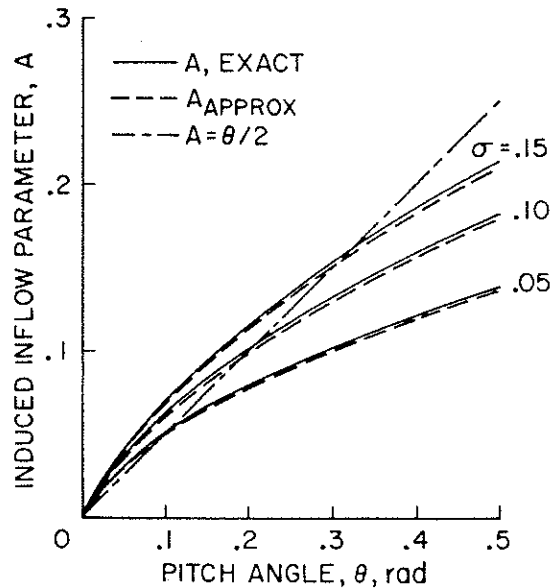
FIGURE 1. Comparison of approximations for induced inflow-parameter A.

yields $A = \theta/2$. This approximation eliminates the small aerodynamic lead moment in the lead-lag coupling coefficient $C_{\dot{\beta}}$.

Another useful but more accurate approximation for the induced inflow parameter can be derived as follows. The exact expression for A is based on non-uniform induced inflow given by blade-element momentum theory.[5] For $a = 2\pi$

$$v_i = \pi\sigma\Omega R/8[\sqrt{1 + 16\theta\xi/\pi\sigma} - 1] \qquad (6)$$

If ϕ_i is approximated by the value at $\xi = {}^3/_4$, the following equation for A results

$$A_{\mathrm{approx}} = \pi\sigma/6[\sqrt{1 + 12\theta/\pi\sigma} - 1] \qquad (7)$$

The accuracy of these two approximate expressions is compared with the exact value in Fig. 1. The effect of solidity is seen to be important and therefore limits the usefulness of $A = \theta/2$ for quantitative results. A_{approx}, however, is quite accurate and will be used for the results which follow.

A detailed examination of flap-lag stability and dynamics will now be carried out for several specific cases. For the approximate rigid blade equations these include: 1) basic flap-lag coupling, 2) the effects of pre-cone, 3) variable elastic coupling, and 4) pitch-lag coupling. Next, the results using multimode elastic blade equations are presented and compared with previous results and finally, the effects of elastic coupling on flapping response are examined.

RIGID BLADE STABILITY

Case I, No Pre-cone or Elastic Coupling

A broad view of the basic flap-lag stability characteristics of the rigid hinged blade is afforded by Fig. 2.

The nondimensional eigenvalues of Eq. (1) above are presented in the complex plane as a function of increasing collective pitch, for several values of inplane stiffness. The flap mode is stable in all cases, but the weakly damped lead-lag mode becomes unstable for inplane frequencies near p. Some idea of the magnitude of the instability may be gained from the time to double amplitude. With $\bar{\sigma}_\zeta = 0.002$ at 250 rpm, $t_{\mathrm{double}} = 13.2$ sec, which is not particularly rapid.

The neutral stability condition ($\bar{\sigma}_\zeta = 0$) will now be examined with the aid of Routh's criteria. The characteristic equation of the basic flap-lag equations is a quartic of the following form

$$As^4 + Bs^3 + Cs^2 + Ds + E = 0 \qquad (8)$$

Neutral stability occurs when Routh's discriminant vanishes, i.e.,

$$F = D(BC - AD) - B^2E = 0 \qquad (9)$$

After some manipulation the following expression for the collective pitch for neutral stability is obtained.

$$(\theta - A)^2 = \frac{P^2}{2(P-1)(2-P)} \times$$
$$\left\{ D + \frac{[D + A\theta][P - W]^2}{\eta^2[W + P(D + A\theta)][1 + D + A\theta]} \right\} \qquad (10)$$
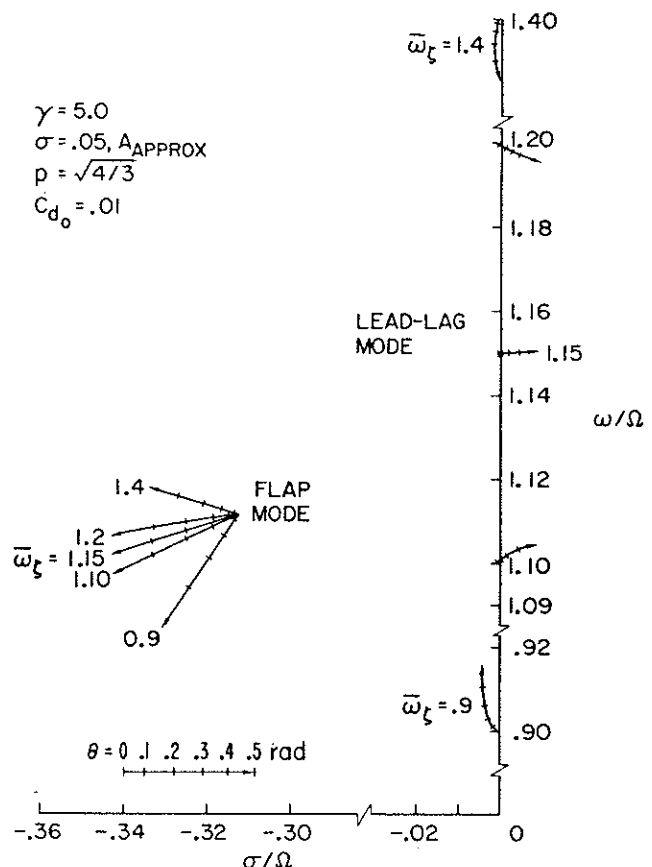

FIGURE 2. Locus of roots for increasing pitch angle, Case I, basic rigid blade equations.

where

$$D = \frac{2c_{d_0}}{a}, \; P = p^2, \; W = \bar{\omega}_\zeta{}^2, \;\; \eta = \gamma/8 \quad (11)$$

Several conclusions immediately follow since $c_{d_0} > 0$, $A\theta > 0$. First, a necessary (but not sufficient) condition for instability is that $1 < p^2 < 2$. This indicates that purely articulated rotors without hinge offset or $\delta_3 (p = 1)$ cannot be unstable. This does not mean that destabilizing flap-lag coupling is not present, but only that it can never be sufficient to cause instability. Second, for a given flap frequency (p) the minimum pitch angle for neutral stability, $\theta_{\min}$, occurs when $\bar{\omega}_\zeta = p$ and is independent of Lock number.

$$(\theta_{\min} - A)^2 = [P^2 D/2(P - 1)(2 - P)] \quad (12)$$

Finally an absolute minimum can be obtained for $p = \sqrt{4/3}$. This value will be referred to as θ^* and is dependent only on the profile drag coefficient and induced inflow parameter, A. For $a = 2\pi$

$$(\theta^* - A) = 2\sqrt{c_{d_0}/\pi}, \quad p = \bar{\omega}_\zeta = \sqrt{4/3} \quad (13)$$

This simple result specifies the lowest possible pitch angle for which any hingeless rotor blade can become unstable in pure flap-lag oscillations.

Structural damping is easily incorporated by modifying the lead-lag damping coefficient C_ζ.

$$C_\zeta = \gamma/8 \left[\frac{2c_{d_0}}{a} + 2\eta_m \frac{\bar{\omega}_\zeta}{\gamma/8} + A\theta \right] \quad (14)$$

The three terms are respectively the profile drag damping, structural damping, and induced drag damping. For typical parameters $1/2\%$ structural damping $(\eta_m = 0.005)$ is on the order of 3 times the profile drag damping which would significantly increase θ^*.
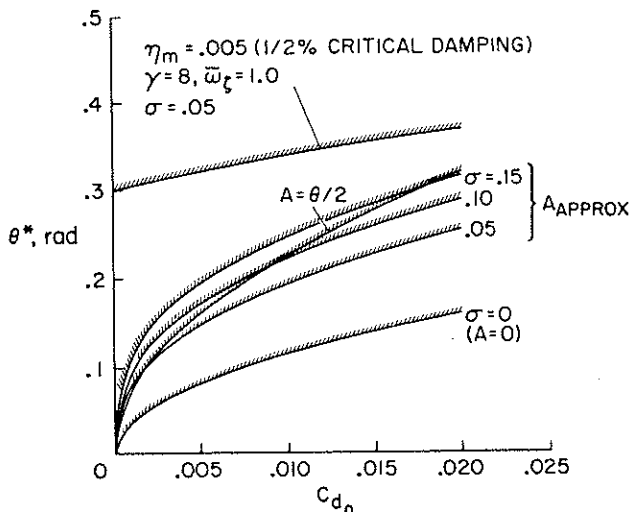

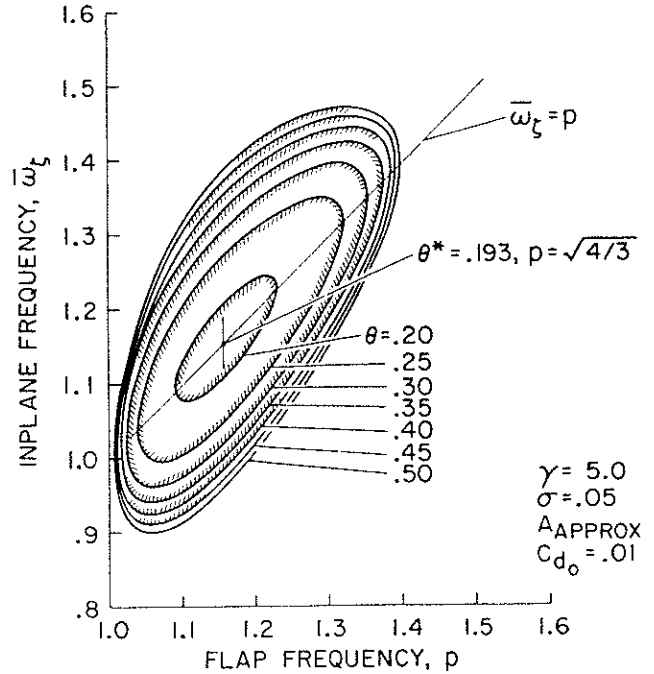FIGURE 3. Effect of profile drag, structural damping, and aerodynamics on θ^*.

FIGURE 4. Stability boundaries for basic rigid blade equations.

Figure 3 illustrates the relationship between inplane damping and θ^* given by Eq. (13) including the effects of structural damping and various approximations for the induced inflow parameter A.

A summary plot giving basic flap-lag stability boundaries as a function of the flap and lead-lag frequencies is given in Fig. 4. For a particular collective pitch, the region of instability lies within the respective contour. These results illustrate the occurrence of $\theta_{\min}$ for a given value of p when $\bar{\omega}_\zeta = p$ and θ^* when $p = \sqrt{4/3}$.

Case II, Effect of Pre-cone, No Elastic Coupling

With pre-cone, the perturbation equations are identical to those used previously although the coning now becomes

$$\beta_0 = [\gamma/8](\theta - A)/p^2 + (p^2 - 1)\beta_{pc}/p^2 \quad (15)$$

Routh's criteria yields the following expression for the collective pitch for neutral stability.

$$(\theta - A)^2 = \frac{P^2}{2(P - 1)(2 - P)} \times$$

$$\left\{ D + \frac{(D + A\theta)(P - W)^2}{\eta^2 [W + P(D + A\theta)][1 + D + A\theta]} + \right.$$

$$\frac{2\beta_{pc}(P - 1)}{\eta P^2} \left[\frac{2\beta_{pc}(P - 1)}{\eta} - \right.$$

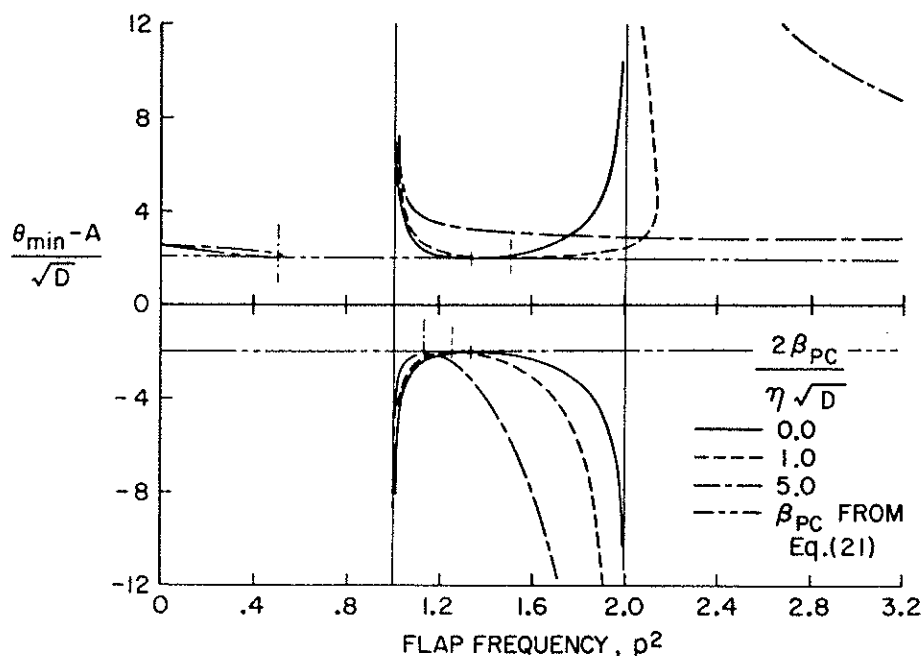$$\left. \left. (3P - 4)(\theta - A) \right] \right\} \quad (16)$$

FIGURE 5. Effect of pre-cone on the minimum pitch angle for neutral stability, $\bar{\omega}_\zeta = p$.

We will first examine the case of "ideal" pre-cone, when the aerodynamic and inertial flap moments are exactly balanced and the hinge spring supplies zero flap moment.

$$\beta_{pc_i} = [\gamma/8](\theta - A) \qquad (17)$$

Substitution into Eq. (16) indicates that instability is not possible. This is because the destabilizing flap-lag coupling is exactly cancelled by the lead-lag induced drag damping ($A\theta$ in Eq. 14). This indicates that pre-cone can be strongly stabilizing although further examination of Eq. (16) indicates that for $\beta_{pc} \neq \beta_{pc_i}$ pre-cone may also be destabilizing. The worst condition occurs when

$$\beta_{pc_\omega} = \frac{\eta}{4} \frac{(3P - 4)}{(P - 1)} (\theta - A) \qquad (18)$$

The corresponding pitch angle for neutral stability is

$$(\theta - A)^2 = 4 \left\{ D + \frac{[D + A\theta][P - W]^2}{\eta^2[W + P(D + A\theta)][1 + D + A\theta]} \right\} \qquad (19)$$

For a given flap frequency p, the least stable condition again occurs when $\bar{\omega}_\zeta = p$ but unlike basic flap-lag stability, it is independent of p. In other words $\theta_{min} = \theta^*$; Eq. (19) becomes for $a = 2\pi$

$$(\theta_{min} - A) = 2\sqrt{c_{d_0}/\pi} \qquad (20)$$

The required pre-cone for least stability then becomes

$$\beta_{pc_\omega} = [\gamma/16][(3P - 4)/(P - 1)]\sqrt{c_{d_0}/\pi} \qquad (21)$$

These results are illustrated in Fig. 5 by a plot of the normalized value of the minimum pitch angle for neutral stability, $(\theta_{min} - A)/\sqrt{D}$, as a function of the flap frequency, p. For simplicity $\bar{\omega}_\zeta = p$. For zero pre-cone the previous result for θ_{min} applies and $\theta_{min} = \theta^*$ when $p = \sqrt{4/3}$. For pre-cone variation with p according to Eq. (21) the absolute minimum θ^* occurs for any value of p. Even the previous limits $1 < p^2 < 2$ no longer apply. Also shown in Fig. 5 are stability boundaries for constant β_{pc} values. Minimum stability still occurs when $\bar{\omega}_\zeta = p$ although the positive and negative roots for θ_{min} are no longer equal. Furthermore, a sign change for β_{pc} or θ is equivalent. The general effect of pre-cone is to shift the flap frequency for least stability ($\theta_{min} = \theta^*$) away from $p = \sqrt{4/3}$. Indeed, θ^* occurs when p is given by Eq. (21). These results clearly show that pre-cone can be a destabilizing factor for flap-lag oscillations.

It may be noted that the above conclusions differ somewhat from previous results. In Ref. 2, it was concluded that for centrally hinged rigid blades in hover, destabilizing flap-lag coupling would vanish when flapping restraint vanished ($p = 1$, articulated blade) or when the blades were ideally pre-coned. As a result, flap-lag instabilities were precluded. The present study indicates that flap-lag coupling does not vanish under these conditions, for instance Eq. (5) indicates that $F_\zeta C_{\dot\beta} \neq 0$ for $p = 1$. This discrepancy can be attributed to the derivation of the aerodynamic flap and lead moments and is further discussed in the Appendix.

Case III, Variable Elastic Coupling

The applicable homogeneous equations for this case, taken from the Appendix are

$$\begin{bmatrix} s^2 + F_{\dot\beta}s + F_\beta & -sF_{\dot\zeta} + F_\zeta \\ -sC_{\dot\beta} + C_\beta & s^2 + C_{\dot\zeta}s + C_\zeta \end{bmatrix} \begin{Bmatrix} \Delta\beta \\ \Delta\zeta \end{Bmatrix} = 0 \quad (22)$$

The elastic coupling terms F_ζ and C_β produce cross coupled flap and lead-lag moments proportional to lead-lag and flap deflections respectively. Previous studies have typically neglected these terms in simplified rotor blade stability analyses. However, as will be seen below, they can have pronounced effects on the stability and dynamic characteristics of rotor blade flap-lag motion. For small pitch angles F_ζ and C_β are given by

$$R(\bar\omega_\zeta{}^2 - \bar\omega_\beta{}^2)\theta \qquad (23)$$

Elastic coupling is proportional to pitch angle and is configuration dependent by virtue of the nonrotating lead-lag and flap frequencies $\bar\omega_\zeta$, $\bar\omega_\beta$, and the variable elastic coupling parameter R.

The elastic coupling of actual hingeless rotor blades is dependent on the particular design configuration and specifically the distribution of flexibility radially inboard and outboard of the pitch bearing. As explained in the Appendix, this characteristic is introduced in the rigid blade equations by dividing the flap and lead-lag hinge springs into two separate spring systems, one inboard and the other outboard of the pitch axis. The degree of elastic coupling is denoted by R and is proportional to the fraction of flexibility present in the spring system outboard of the hinge axis.

Representative results for the locus of roots of the lead-lag mode are shown in Fig. 6. In comparison with Fig. 2 it is apparent that the degree of elastic coupling R is highly important in determining whether the effects are stabilizing or destabilizing. For full elastic coupling, $R = 1.0$, the effect is generally highly stabilizing for the range of lead-lag frequencies considered. It is suggested that the elastic coupling allows the transfer of kinetic energy from the weakly damped inplane degree of freedom to the well damped flapping mode. As a result, the inherently low aerodynamic and structural lead-lag damping can easily be augmented by more than an order of magnitude. This is significant since it implies that the inplane degree of freedom is not as susceptible to instabilities as its low inherent damping would suggest.

Further examination of Fig. 6 indicates that small amounts of elastic coupling can be destabilizing for stiff inplane ($\bar\omega_\zeta > 1$) hingeless rotors whereas soft inplane
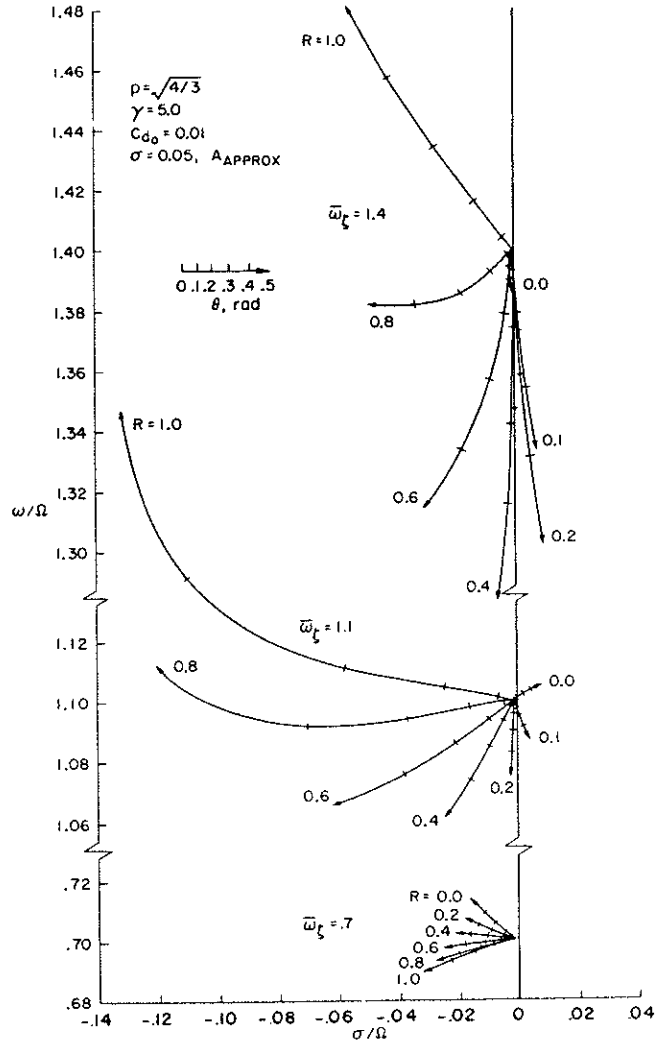

FIGURE 6. Locus of lead-lag mode roots, Case III, rigid blade equations with variable elastic coupling.

($\bar\omega_\zeta < 1$) rotor blades are only stabilized by elastic coupling. Further evidence is provided by Fig. 7 which presents stability boundaries for variable elastic coupling as a function of inplane frequency with $p = \sqrt{4/3}$. This figure clearly shows that for stiff inplane blades there exists a particular value of R for which instability can occur at moderately low pitch angles but that increased elastic coupling is strongly stabilizing. Furthermore, this minimum pitch angle is equal to θ^* given by Eq. (13) for the basic flap-lag equations.

Routh's criteria can be used to clarify these results. The equations with elastic coupling yield the following expression for the collective pitch for neutral stability.

$$(\theta - A)^2 = \frac{P^2}{2(P-1)(2-P)} \times$$

$$\left\{ D + \frac{(D + A\theta)(W - P)^2 - Z(\theta + A)(W - P)[1 - (D + A\theta)] + Z^2[(D + A\theta + 1)^2 - (\theta + A)^2]}{\eta^2(D + A\theta + 1)[W + P(D + A\theta) + Z(\theta + A)]} \right\} \quad (24)$$
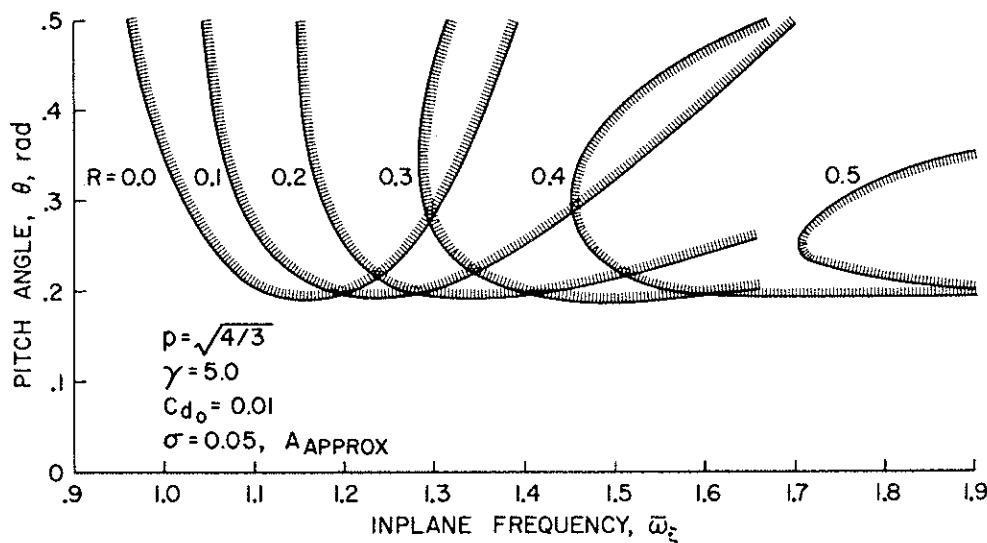
FIGURE 7. Stability boundaries for rigid blade equations with variable elastic coupling.

where

$$P = p^2, \quad W = q^2, \quad Z = z^2 \tag{25}$$

This expression neglects the effect of elastic coupling on β_0 which is consistent with dropping second order terms in the perturbation analysis. Equation (24) confirms that elastic coupling, Z, can be destabilizing; however, it can be shown that θ cannot be less than θ^*. For small pitch angles ($\theta^2 \ll 1$) Eq. (24) can be greatly simplified yielding

$$(\theta - A)^2 = \frac{P^2}{2(P-1)(2-P)} \times$$

$$\left\{ D + \frac{\left[D - \frac{(\theta-A)^2}{4} \right](W-P)^2 + \left[\frac{(\theta+A)(W-P)}{2} - R\theta(W-P+1) \right]^2}{\eta^2 W} \right\} \tag{26}$$

where now

$$P = \bar{\omega}_\beta{}^2 + 1, \quad W = \bar{\omega}_\zeta{}^2 \tag{27}$$

This equation illustrates that for the elastic coupling to be destabilizing the lead-lag frequency must be such that $W > P$ or $W < P - 1$. This confirms the results of Fig. 6 that elastic coupling can be destabilizing for stiff inplane but not soft inplane rotor blades. Furthermore, when $p = \sqrt{4/3}$ the value of R corresponding to the least stable value of lead-lag frequency can be found since $(\theta^* - A)^2 = 4D$. Equation (26) then yields

$$R = \frac{\theta^* + A}{2\theta^*} \frac{(W - 4/3)}{(W - 1/3)} \tag{28}$$

The significance of this result is that when $p = \sqrt{4/3}$, it is not necessary that $\bar{\omega}_\zeta = p$ for neutral stability to occur at $\theta = \theta^*$ as is the case without elastic coupling. In other words, rotor blade configurations with inplane frequencies differing from p are subject to the same critical stability condition if the elastic coupling is in accord with Eq. (28).

Case IV, Pitch-lag Coupling

To provide further information about hingeless rotor blade stability characteristics, a brief examination of the influence of kinematic pitch-lag coupling has been made. Since the important torsional degree of freedom is not included in the present paper, this represents a restricted but convenient way of assessing the effects of pitching motion in comparison with flap-lag and elastic coupling effects. The previous equations with elastic coupling (Case III) together with the non-homogeneous pitch angle terms given in Eq. (50) were combined using the following pitch-lag relation.

$$\Delta\theta = \theta_\zeta \Delta\zeta \tag{29}$$

Representative results for stability boundaries with respect to collective pitch are given in Fig. 8 for both stiff and soft inplane rotor blade configurations. For the soft inplane configuration, pitch-lag instability can occur only for positive values of θ_ζ. Also, the effects of elastic coupling are relatively small, in fact slightly destabilizing. The results are entirely different for the stiff inplane configuration however, where elastic coupling plays a major role. First, for $R = 0.0$, negative values of θ_ζ are destabilizing in opposition to the soft

inplane result. Second, elastic coupling is strongly stabilizing for negative θ_ζ but becomes progressively destabilizing as R increases and θ_ζ becomes positive. As a result, it appears that elastic coupling is wholly as effective as pitch-lag coupling in determining the flap-lag stability of stiff inplane rotor blades. This implies that proper combinations of these two parameters might be used to improve, or "optimize" the stability characteristics of stiff inplane configurations.

MULTI-MODE ELASTIC BLADE EQUATIONS

The basic partial differential equations for a uniform untwisted rotating beam are presented in the Appendix, together with a brief outline of the method of solution. Particular care was required to insure that centrifugal and Coriolis forces which produce the destabilizing flap-lag coupling were retained in the derivation. These forces arise from blade radial displacements and tension variations resulting from perturbation deflections and velocities respectively. These effects are normally not included in elastic rotor blade equations. In addition, they do not have direct counterparts in the approximate rigid blade equations since radial displacements and tension do not appear explicitly in those equations.

Results obtained using the elastic blade modal equations are presented in Fig. 9. The first inplane mode damping is relatively high as a result of the elastic coupling. Because the principle elastic axes of the rotor blade rotate through the pitch angle θ for the entire length of the blade, the elastic coupling is equivalent to $R = 1.0$ for the rigid blade. The effect of number of the modes retained in the equations is relatively slight as far as the first inplane mode damping is concerned. A single flap and lead-lag mode are denoted by $n = 1$, two of each mode are included for $n = 2$. To illustrate the importance of the proper derivation of the elastic equations, the damping is also shown with the radial displacement and tension perturbations neglected. This gives a very unconservative result since the destabilizing flap-lag terms are not present.

A comparison with the rigid blade damping ($R = 1.0$) shows the approximate equations to be quite ac-
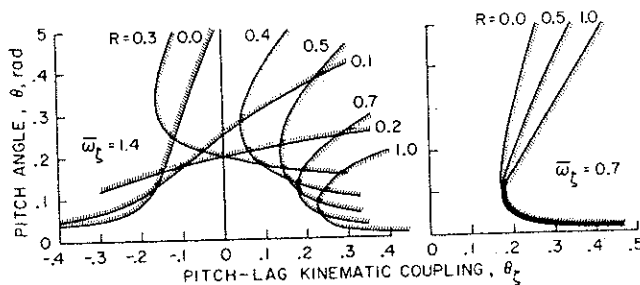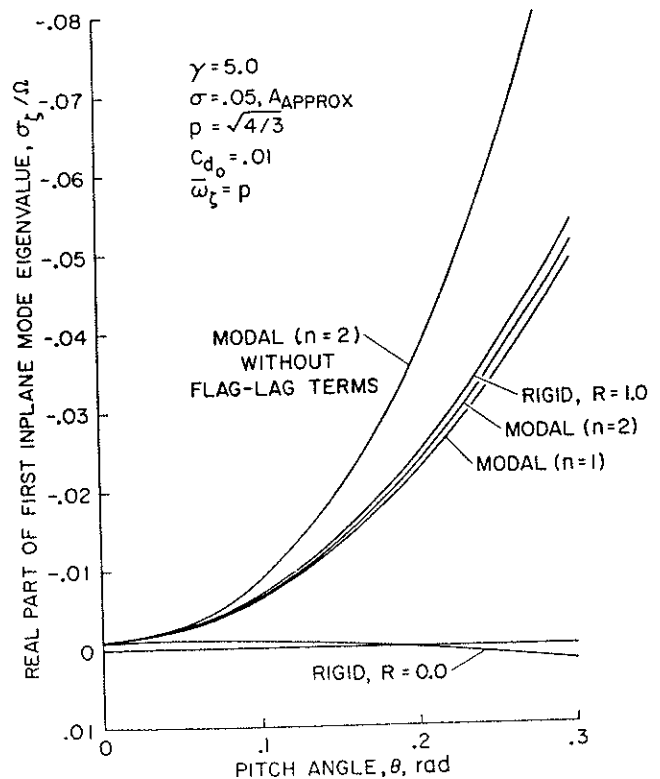
FIGURE 9. Comparison of inplane mode damping from approximate rigid blade equations and elastic blade modal equations.

curate. That this is a result of proper inclusion of elastic coupling is shown by the rigid blade result without elastic coupling ($R = 0.0$).

EFFECT OF ELASTIC COUPLING ON FLAPPING RESPONSE

In addition to modifying the flap-lag stability characteristics, elastic coupling also produces significant variations in flapping frequency as collective pitch is increased. For a hingeless rotor blade this results in a variation in the phase lag of the blade flapping response to harmonic pitch excitations. The control inputs to a rotor from the swashplate are harmonic once-per-rev pitch changes and the flapping phase lag directly determines the ratio of the resulting rotor pitch and roll moments. The implications of elastic coupling can thus be appreciated in terms of vehicle stability and control characteristics.

The magnitude of the frequency shift is shown in Fig. 10 for the rigid blade with full elastic coupling and with aerodynamics neglected. At zero pitch the flap and lead-lag modes are uncoupled, but for $\theta = 0.3$ rad significant coupling exists. Note that elastic coupling vanishes when $\bar{\omega}_\beta = \bar{\omega}_\zeta$ and the frequencies are identical for all pitch angles.

Figure 11 illustrates the flapping response phase lag from pitch excitation for cases with and without elastic coupling. In particular, for stiff inplane rotor blades the influence of elastic coupling can be quite significant.

FIGURE 8. Stability boundaries for rigid blade equations, Case IV, kinematic pitch-lag coupling and variable elastic coupling, $p = \sqrt{4/3}, \gamma = 5.0, c_{d_0} = 0.01, \sigma = 0.05$.
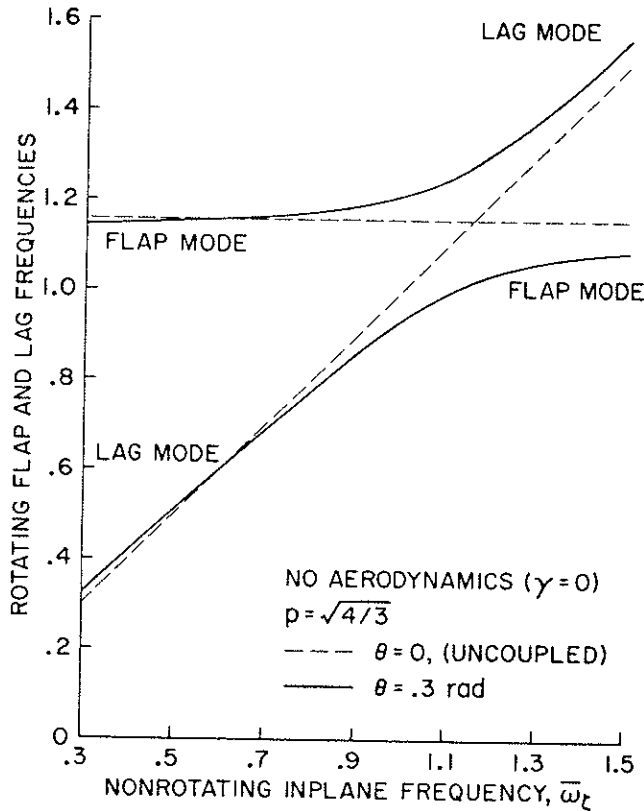
FIGURE 10. Effect of elastic coupling on rigid hinged blade flap and lead-lag frequencies without aerodynamics, $R = 1.0$.

Figure 12 further illustrates this effect as a function of collective pitch for a specific configuration.

CONCLUSIONS

The most important findings of the present study may be summarized as follows:

1) For torsionally rigid, spring restrained centrally hinged rotor blades flap-lag instability cannot occur in hover for pitch angles less than $\theta = \theta^*$.

2) Without pre-cone or elastic coupling, instability will not occur for practical pitch angles unless the inplane and flapping frequencies are reasonably close. For $\bar{\omega}_\zeta = p = \sqrt{4/3}$, neutral stability occurs at $\theta = \theta^*$.

3) Without elastic coupling the effect of pre-cone on stability may be either beneficial or detrimental. Ideal pre-cone eliminates flap-lag instability in hover.

4) Full elastic coupling virtually eliminates flap-lag instability and greatly augments the inherently low aerodynamic and structural damping of the lead-lag degree of freedom. Partial elastic coupling can be strongly destabilizing for stiff inplane rotor blades, however, and for $p = \sqrt{4/3}$ instability can occur for $\theta = \theta^*$ for a particular value of R.

5) The effects of kinematic pitch-lag coupling on flap-lag stability are highly dependent on elastic coupling for stiff inplane rotor blades, but not for soft inplane ones.

6) The flapping response phase for $1P$ pitch excitation is significantly altered by elastic coupling. This implies that coupled rotor-fuselage dynamic equations should include the rotor blade inplane degree of freedom.

7) The rigid hinged blade gives a reasonably accurate approximation of the actual elastic blade stability if the elastic coupling effects are properly accounted for.

APPENDIX

A brief derivation of the aerodynamic forces and equations of motion for both the rigid hinged blade and the elastic blade are given below. The basic x, y, z rotating coordinate system in Fig. 13 shows the positive conventions for angular (β, ζ) and linear (u, v, w) displacements (except a negative u displacement is shown).

AERODYNAMIC FORCES

The y and z components of the aerodynamic loading (lb/ft) can be written as follows

$$dF_z = dL - \phi dD \qquad dF_y = -dD - \phi dL \quad (30)$$

The elemental lift and drag forces can be written from simple strip theory. Since $\alpha = \theta - \phi$ and $\phi \simeq U_P/U_T$ for small inflow angles

$$dL = \frac{\rho ac}{2} V^2 \left(\theta - \frac{U_P}{U_T} \right) dx \qquad dD = \frac{\rho c V^2}{2} c_{d_0} dx \quad (31)$$

Combining Eqs. (30 and 31) and noting that $(U_P/U_T)^2 \ll 1$ yields

$$dF_z = \frac{\rho ac}{2} \left\{ \theta U_T^2 - \left(1 + \frac{c_{d_0}}{a} \right) U_P U_T \right\} dx \quad (32)$$

$$dF_y = -\frac{\rho ac}{2} \left\{ \frac{c_{d_0}}{a} U_T^2 + \theta U_P U_T - U_P^2 \right\} dx \quad (33)$$

Incorporating the airfoil flap and lead displacements (v, w) in the rotating coordinate system, the relative fluid velocities become

$$U_P = v_t + \dot{w} \qquad U_T = \Omega x + \dot{v} \quad (34)$$

The final equations are then obtained after discarding second order products of displacement velocities $(\dot{w}^2, \dot{v}^2, \dot{w}\dot{v})$.

$$dF_z = \frac{\rho ac}{2} \left\{ \theta \Omega^2 x^2 - \right.$$

$$\left(1 + \frac{c_{d_0}}{a} \right) \Omega x v_t + \dot{v} \left[2\Omega x \theta - v_t \left(1 + \frac{c_{d_0}}{a} \right) \right] -$$

$$\left. \Omega x \dot{w} \left(1 + \frac{c_{d_0}}{a} \right) \right\} dx \quad (35)$$
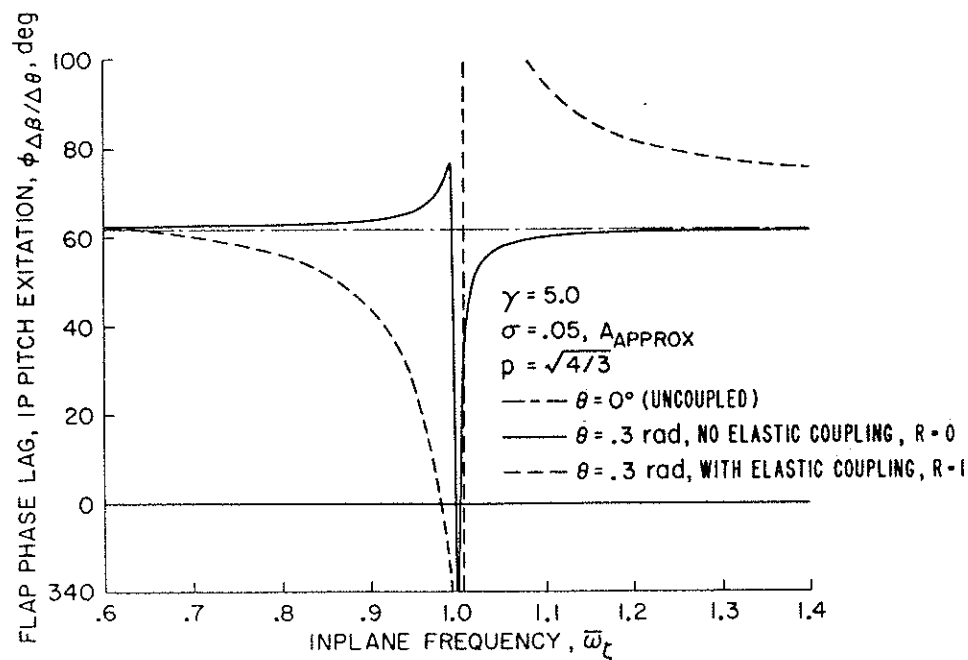
FIGURE 11. Effect of elastic coupling on flap response phase lag from pitch angle excitation, rigid blade.

$$dF_y = -\frac{\rho a c}{2} \left\{ x^2\Omega^2 \frac{c_{d_0}}{a} + \theta x \Omega v_i - v_i^2 + \right.$$

$$\left. \dot{v}\left(2x\Omega \frac{c_{d_0}}{a} + \theta v_i\right) + \dot{w}(\theta\Omega x - 2v_i) \right\} dx \quad (36)$$
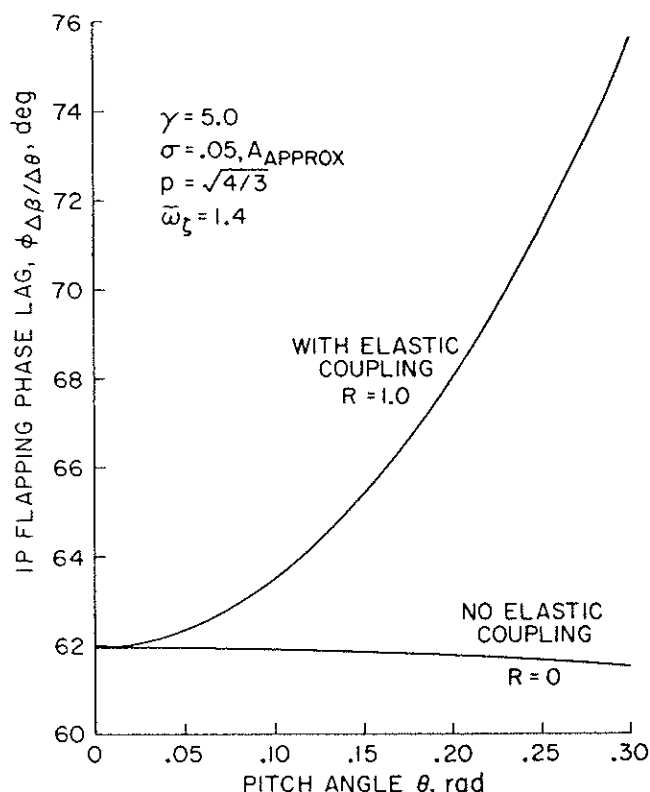
These are the general aerodynamic loading expressions including the effects of flap and lead velocities. The difference between the present results and those of Ref. 2 noted earlier lies in derivation of these equations. In Ref. 2, U_T in Eq. (31) was approximated by Ωx rather than the complete equation given by (34), $\Omega x + \dot{v}$. This results in an error in the coefficient of the first order $\dot{v}$ term in Eqs. (35) and (36).

For the elastic blades the aerodynamic loading can be applied directly to the relevant partial differential equations given below. For centrally hinged rigid blades, the aerodynamic moments about the hinges for the flap and lead-lag equations are easily developed. The kinematics of a rigid blade implies

$$\dot{v} = x\dot{\zeta} \qquad w = x\dot{\beta} \qquad (37)$$

The flap and lead aerodynamic moments are defined by

$$M_{\beta_{aero}} = \int_0^R x dF_z \qquad M_{\zeta_{aero}} = \int_0^R x dF_y \qquad (38)$$

The resulting moments become, for constant chord,

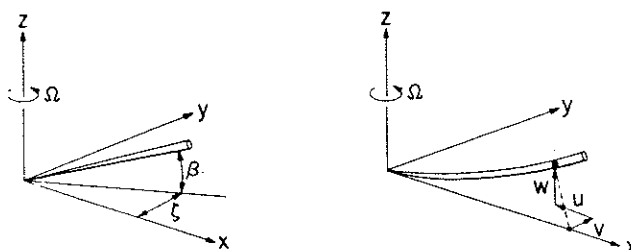FIGURE 12. Flap response phase lag variation with collective pitch, rigid blade.

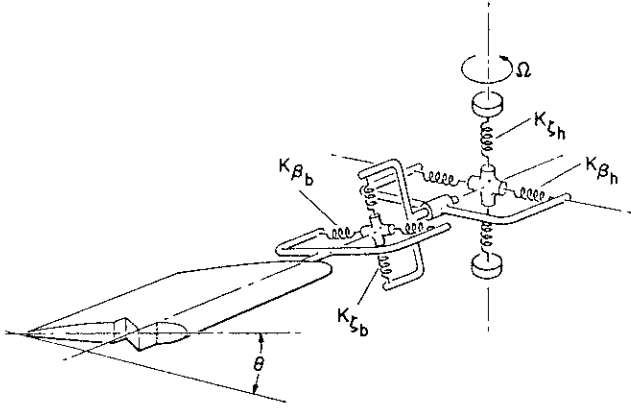FIGURE 13. Rotor blade angular and rectilinear displacements in roating coordinate system.

FIGURE 14. Arrangement of flap and lead-lag springs of rotor blade and hub for simulating variable elastic coupling. For clarity, rotor blade springs shown radially displaced from axis of rotation.

untwisted blades

$$M_{\beta_{aero}} = \frac{\gamma I \Omega^2}{8} \left\{ \theta - \left(1 + \frac{c_{d_0}}{a}\right) A + \right.$$

$$\left. \left[2\theta - \left(1 + \frac{c_{d_0}}{a}\right) A \right] \frac{\dot\zeta}{\Omega} - \left(1 + \frac{c_{d_0}}{a}\right) \frac{\dot\beta}{\Omega} \right\} \quad (39)$$

$$M_{\zeta_{aero}} = -\frac{\gamma I \Omega^2}{8} \left\{ \frac{c_{d_0}}{a} + A\theta - C + \right.$$

$$\left. \frac{\dot\zeta}{\Omega} \left(2 \frac{c_{d_0}}{a} + A\theta \right) + \frac{\dot\beta}{\Omega} (\theta - 2A) \right\} \quad (40)$$

The integrals A, C and Lock number γ are defined by

$$A \equiv 4 \int_0^1 \xi^2 \left(\frac{v_i}{R\Omega}\right) d\xi,$$

$$C \equiv 4 \int_0^1 \xi \left(\frac{v_i}{R\Omega}\right)^2 d\xi, \quad \gamma = \frac{\rho a c R^4}{I} \quad (41)$$

Rigid Blade Equations

The inertial and elastic restraint moments about the centrally located flap and lead-lag hinges are combined with the aerodynamic moments to yield the equations of motion for a rigid hinged rotor blade. The inertial terms, including centrifugal and Coriolis moments are

$$M_{\beta_i} = -I(\ddot\beta + \Omega^2 \beta + 2\Omega\beta\dot\zeta) \quad M_{\zeta_i} = -I(\ddot\zeta - 2\Omega\beta\dot\beta) \quad (42)$$

The elastic restraint hinge moment equations are developed for the spring configuration shown in Fig. 14. Two orthogonal spring systems are attached to the hub and blade inboard and outboard of the pitch axis respectively. The blade spring system, which rotates during collective pitch changes produces a significant cross coupling of flapping moments with lead-lag deflections and vice-versa. This effect, herein termed elastic coupling, is approximately proportional to the flexibility of the blade spring system relative to the total spring

flexibility. Previous studies have treated only the uncoupled configuration, where all flexibility is contained in the hub spring system.

The configuration of Fig. 14 reduces to a simple equivalent single spring system at zero pitch angle which defines the rotor blade nonrotating frequencies. The equivalent spring system is given by

$$K_\beta = \frac{K_{\beta_B} K_{\beta_H}}{K_{\beta_B} + K_{\beta_H}}, \quad K_\zeta = \frac{K_{\zeta_B} K_{\zeta_H}}{K_{\zeta_B} + K_{\zeta_H}} \quad (43)$$

The complete elastic moments can be written as

$$M_{\beta_{elastic}} = -\frac{\beta}{\Delta} [K_\beta + R(K_\zeta - K_\beta \sin^2\theta] -$$

$$\frac{\zeta R}{2\Delta} (K_\zeta - K_\beta) \sin 2\theta \quad (44)$$

$$M_{\zeta_{elastic}} = -\frac{\zeta}{\Delta} [K_\zeta - R(K_\zeta - K_\beta)\sin^2\theta] -$$

$$\frac{\beta R}{2\Delta} (K_\zeta - K_\beta) \sin 2\theta \quad (45)$$

where

$$\Delta = 1 + R(1 - R) \frac{(K_\zeta + K_\beta)}{K_\zeta K_\beta} \sin^2\theta \quad (46)$$

The degree of elastic coupling is governed by R which is defined as

$$R = K_\beta/K_{\beta_B} = K_\zeta/K_{\zeta_B}$$

$$(1 - R) = K_\beta/K_{\beta_H} = K_\zeta/K_{\zeta_H} \quad (47)$$

Where $R = 0.0$ no elastic coupling is present and the hinge spring system is entirely contained at the hub and does not rotate with pitch angle changes. The converse is true for full elastic coupling, $R = 1.0$. Variations in elastic coupling are accommodated by intermediate values of R.

The final flap-lag equations are obtained by combining the aerodynamic, inertial, and elastic contributions. The usual perturbation method of solution is desired wherein

$$\theta(t) = \theta_0 + \Delta\theta(t), \quad \beta(t) = \beta_0 + \Delta\beta(t),$$

$$\zeta(t) = \zeta_0 + \Delta\zeta(t) \quad (48)$$

The equilibrium equations become

$$\begin{bmatrix} p^2 & z^2 \\ z^2 & q^2 \end{bmatrix} \begin{Bmatrix} \beta_0 \\ \zeta_0 \end{Bmatrix} = \gamma/8 \begin{Bmatrix} \theta - A \\ -\left(\frac{c_{d_0}}{a} + A\theta - C\right) \end{Bmatrix} \quad (49)$$

The perturbation equations, which neglect second order nonlinear products such as $\Delta\dot\beta\Delta\beta$, $\Delta\beta\Delta\zeta$, $\Delta\theta\Delta\beta$, and

$\Delta\theta\Delta\zeta$ are Laplace transformed to yield

$$\begin{bmatrix} s^2 + \dfrac{\gamma}{8}s + p^2 & -s\left[\dfrac{\gamma}{8}(2\theta - A) - 2\beta_0\right] + z^2 \\ -s\left[2\beta_0 - \dfrac{\gamma}{8}(\theta - 2A)\right] + z^2 & s^2 + s\dfrac{\gamma}{8}\left(2\dfrac{c_{d_0}}{a} + A\theta\right) + q^2 \end{bmatrix}\begin{Bmatrix} \Delta\beta \\ \Delta\zeta \end{Bmatrix} = \Delta\theta$$

$$\left[\dfrac{\gamma}{8}\begin{Bmatrix}1 \\ -A\end{Bmatrix} - R\dfrac{(\bar\omega_\zeta^2 - \bar\omega_\beta^2)}{\Delta}\left\{R_w\left[\begin{bmatrix}\beta_0 - \dfrac{\gamma}{8}(\theta - A) \\ \dfrac{\gamma}{8}\left(\dfrac{c_{d_0}}{a} + A\theta - C\right)\end{bmatrix}\right] + \beta_0\begin{bmatrix}\sin 2\theta \\ \cos 2\theta\end{bmatrix} + \zeta_0\begin{bmatrix}\cos 2\theta \\ -\sin 2\theta\end{bmatrix}\right\}\right] \quad (50)$$

where

$$R_w = (1 - R)\frac{\bar\omega_\zeta^4 + \bar\omega_\beta^4}{\bar\omega_\zeta^2\bar\omega_\beta^2}\sin 2\theta$$

$$p^2 = 1 + \frac{1}{\Delta}[\bar\omega_\beta^2 + R(\bar\omega_\zeta^2 - \bar\omega_\beta^2\sin^2\theta)]$$

$$q^2 = \frac{1}{\Delta}[\bar\omega_\zeta^2 - R(\bar\omega_\zeta^2 - \bar\omega_\beta^2\sin\theta)] \quad (51)$$

$$z^2 = \frac{R}{2\Delta}(\bar\omega_\zeta^2 - \bar\omega_\beta^2)\sin 2\theta$$

$$\bar\omega_\beta^2 = K_\beta/I\Omega^2, \quad \bar\omega_\zeta^2 = K_\zeta/I\Omega^2$$

Note that for convenience θ_0 has been written as θ in the final equations.

Elastic Blade Equations

Only a brief outline of the equation derivation for an elastic rotor blade will be given. Although the effects of pre-cone for the elastic blade were not investigated, this parameter is included in the following equations for generality. The equations are restricted to untwisted blades with uniform mass and stiffness distributions. In the case of pre-cone, the X axis is rotated through the angle β_{pc} about the Y axis. The following equations are similar to those derived in Ref. 7 except that radial deflections and nonlinear strain have been retained. They are, in order, the radial, inplane, and flapping displacement equations together with the nonlinear strain relation.

$$-T' + m[\ddot u - 2\Omega\dot v - \Omega^2(x + u) + \Omega^2 w\beta_{pc}] = 0 \quad (52)$$

$$-(Tv')' + K_{vv}v'''' + K_{vw}w'''' + $$
$$m[\ddot v - \Omega^2 v + 2\Omega(\dot u - \beta_{pc}\dot w)] = \frac{dF_y}{dx} \quad (53)$$

$$-(Tw')' + K_{ww}w'''' + K_{wv}v'''' + $$
$$m[\ddot w - \Omega^2\beta_{pc}(w\beta_{pc} - (x + u)) + 2\Omega\beta_{pc}\dot v] = \frac{dF_z}{dx} \quad (54)$$

$$T = EA(u' + {}^1\!/_2 v'^2 + {}^1\!/_2 w'^2) \quad (55)$$

where

$$K_{vv} = E(I_2\cos^2\theta + I_1\sin^2\theta) \quad (56)$$

$$K_{ww} = E(I_1\cos^2\theta + I_2\sin^2\theta) \quad (57)$$

$$K_{wv} = K_{vw} = E(I_2 - I_1)\sin\theta\cos\theta \quad (58)$$

The solution proceeds in a manner similar to the rigid blade case, where the displacements are assumed to consist of steady state and perturbation components, $u(x,t) = u_0(x) + \Delta u(x,t)$, and similarly for v, w, and T. The steady state equations then become

$$-T_0' + m\Omega^2 w_0\beta_{pc} - m\Omega^2(x + u_0) = 0 \quad (59)$$

$$-(T_0 v_0')' + K_{vv}v_0'''' + K_{vw}w_0'''' - $$
$$m\Omega^2 v_0 = \frac{dF_{y_0}}{dx} \quad (60)$$

$$-(T_0 w_0')' + K_{ww}w_0'''' + K_{wv}v_0'''' - $$
$$m\Omega^2\beta_{pc}[w_0\beta_{pc} - (x + u_0)] = \frac{dF_{z_0}}{dx} \quad (61)$$

For $\beta_{pc} = 0$, a linear solution for v_0 and w_0 is easily obtained by Galerkin's method after discarding second order terms ($u_0 \ll x$) in Eqs. (59) and (61). For the perturbation equations we have

$$-\Delta T' - m(2\Omega\Delta\dot v - \Omega^2\Delta w\beta_{pc}) = 0 \quad (62)$$

$$-(T_0 v')' - (\Delta T v_0')' + K_{vv}\Delta v'''' + K_{vw}\Delta w'''' + $$
$$m[\Delta\ddot v - \Omega^2\Delta v + 2\Omega(\Delta\dot u - \beta_{pc}\Delta\dot w)] = \frac{d\Delta F_y}{dx} \quad (63)$$

$$-(T_0\Delta w')' - (\Delta T w_0')' + K_{ww}\Delta w'''' + K_{wv}\Delta v'''' + $$
$$m[\Delta\ddot w + 2\Omega\beta_{pc}\Delta\dot v] = \frac{d\Delta F_z}{dx} \quad (64)$$

$$\Delta T = EA[\Delta u' + v_0'\Delta v' + w_0'\Delta w'] \quad (65)$$

Equations (63) and (64) are the inplane and flapping perturbation equations for an elastic rotor blade. Without the perturbation tension, ΔT, and radial displace-

ment, Δu, terms these equations are conventional. However, the ΔT and Δu terms give rise to the de-stabilizing flap-lag effects and must be retained. The additional equations (62) and (65) can be substituted into Eqs. (63) and (64) to yield two equations in two unknowns Δv, Δw which are then solved by Galerkin's method. The flap and lead-lag displacements are ex-expressed in series form.

$$\Delta v(x,t) = \sum_{n=1}^{N} V_n(t)\phi_{v_n}(x) \qquad (66)$$

$$\Delta w(x,t) = \sum_{n=1}^{N} W_n(t)\phi_{w_n}(x) \qquad (67)$$

ACKNOWLEDGEMENT

REFERENCES

1. Young, M. I., "A Theory of Rotor Blade Motion Stability in Powered Flight", *J. American Helicopter Society*, Vol. 9, No. 3 July 1964.

2. Hohenemser, K. H. and Heaton, P. W. Jr., "Aeroelastic Instability of Torsionally Rigid Helicopter Blades," *J. American Helicopter Society*, 2 (12) April 1967.

3. Gaffey, T. M., *The Effect of Positive Pitch-Flap Coupling (Negative δ_3) on Rotor Blade Motion Stability and Flapping*, Proceedings, American Helicopter Society 24th Annual National Forum, Washington, D.C. May 1968.

4. Jenkins, J. L. Jr., *A Parametric Study of Blade Motion Stability Boundaries for an Articulated Rotor*, NASA TND-5032, February 1969.

5. Hall, W. E. Jr., *Application of Floquet Theory to the Analysis of Rotary-Wing VTOL Stability*, Stanford University, SUDAAR No. 400 February 1970.

6. Gessow, A. and Myers, G. D., Jr., *Aerodynamics of the Helicopter*, Frederick Ungar Publishing Company, New York, 1967.

7. Houbolt, J. C. and Brooks, G. W., *Differential Equations of Motion for Combined Flapwise Bending, Chordwise Bending, and Torsion of Twisted Nonuniform Rotor Blades*, NACA Report 1346, October 1956.

Flap-Lag Stability of Helicopter Rotor Blades in Forward Flight

David A. Peters

Flap-Lag Stability of Helicopter Rotor Blades in Forward Flight

David A. Peters
Assistant Professor of Mechanical Engineering
Washington University, St. Louis, Missouri

Peters

The linearized stability characteristics of rotor blades in forward flight are examined. Equations of motion are derived for the case of a centrally hinged spring restrained rigid blade. Various commonly used approximations for the equations of motion are examined in order to determine their effect on stability calculations. These comparisons show that periodic coefficients are important for flap-lag stability even at low advance ratios. The effect of rotor equilibrium on blade stability is studied. It is found that the variation in rotor trim and inflow with forward speed has a significant effect on blade stability. Finally, rotor stability boundaries are presented for a variety of rotor parameters showing that forward flight can often change the qualitative effects of certain parameters on blade stability.

NOTATION

a = slope of lift curve, rad^{-1}
b = number of blades
c = blade chord, m
c_{d_0} = blade profile drag coefficient
C_T = thrust coefficient, $T/\rho\pi R^2(\Omega R)^2$
$[C(\psi)]$ = damping matrix
d = local blade drag per unit length, N/m
D = helicopter parasite drag, $D = f\rho V_x^2/2$, N
f = helicopter flat plate drag area, m^2

$\bar{f}$ = nondimensional area, $f/\pi R^2$
F_β, F_ζ = force per unit length, perpendicular to blade and also perpendicular and parallel, respectively, to direction of rotation, N, $\bar{F}_\beta = R^2 F_\beta/\Omega^2 I$, $\bar{F}_\zeta = R^2 F_\zeta/\Omega^2 I$
I = blade inertia, kg-m^2
$[K(\psi)]$ = stiffness matrix
l = local blade lift per unit length, N/m
p = dimensionless rotating flapping frequency at $\theta = 0$, $p = \sqrt{P(\theta = 0)} = \sqrt{1 + \omega_\beta^2}$
P = stiffness parameter, Eq. 2
r = blade radial coordinate, m
$\bar{r}$ = nondimensional coordinate, r/R
R = blade radius, m, or elastic coupling parameter
t = time, sec
T = rotor thrust, N
U = total velocity of blade section relative to air
U_p, U_t = local velocity of blade relative to air in F_β and F_ζ directions, respectively, m/sec
$\bar{U}_p, \bar{U}_t$ = nondimensional velocities $U_p/\Omega R$, $U_t/\Omega R$
V_i = uniform induced velocity in negative z direction, m/sec
V_x, V_z = components of helicopter speed in negative X and positive Z directions, respectively, m/sec
W = stiffness parameter, Eq. 2

2

87

X, Y, Z, x, y, z = aircraft coordinates and rotating blade coordinates respectively

Z = stiffness parameter, Eq. 2

α = local blade angle of attack, rad

α_s = rotor shaft angle, positive nose down, rad

β = flapping angle, positive up, rad

$\bar{\beta}$ = equilibrium flapping angle, $\beta_0 + \beta_s s\psi + \beta_c c\psi$, rad

β_{pc} = precone angle, rad

γ = Lock number, $\rho a c R^4/I$

$\delta\beta, \delta\zeta$ = perturbation flapping and lead-lag angles, rad

Δ = coupling parameter, Eq. 2

ζ = lead-lag angle, positive forward, rad

$\bar{\zeta}$ = equilibrium lead-lag angle, rad

η = negative real portion of lead-lag eigenvalue, rad^{-1}

θ = pitch angle, $\bar{\theta} + \theta_\beta \delta\beta + \theta_\zeta \delta\zeta$

$\bar{\theta}$ = equilibrium pitch angle, $\theta_0 + \theta_s\psi + \theta_c c\psi + \theta_\beta(\bar{\beta} - \beta_{pc}) + \theta_\zeta\bar{\zeta}$, rad

$\theta_\beta, \theta_\zeta$ = pitch-flap and pitch-lag coupling ratios

λ = inflow ratio, $(V_i + V_z)/\Omega R$

μ = advance ratio, $V_x/\Omega R$

ν = induced flow ratio, $V_i/\Omega R$

ρ = density of air, kg/m^3

σ = rotor solidity, bc/πR

ϕ = local freestream angle, $\tan^{-1}(U_p/U_t)$, rad

$\bar{\phi}$ = inflow parameter, $\bar{\phi} \approx 4/3\lambda$

ψ = rotor azimuth angle, $\psi = 0$ aft, $\psi = \Omega t$, rad, dimensionless time

$\omega_\beta, \omega_\zeta$ = dimensionless nonrotating flap and lead-lag frequencies at $\theta = 0$

Ω = rotor angular velocity, rad/sec

$s\psi, c\psi$ = sine (ψ), cosine (ψ)

$(\cdot)$ = $\dfrac{d}{d\psi}(\ ) = \dfrac{1}{\Omega}\dfrac{d}{dt}(\ )$

The dynamics of hingeless or semi-hingeless rotorcraft involve the coupled aeroelastic motions of the rotor blades and of the fuselage in forward flight. Due to the complexity of the problem, however, much recent work has emphasized the analysis and understanding of small parts of the problem. For the rotor alone, efforts have mainly considered pitch-flap and pitch-flap-lag dynamics in hover or flap dynamics in forward flight. Flap-lag stability in hover is fairly well understood in terms of stabilizing or destabilizing flap-lag coupling, Refs. 1 and 2; and flapping

stability in forward flight is fairly well understood in terms of parametric or Hill type instabilities, Ref. 3. The next logical step is to study the coupled flap-lag dynamics of rotor blades in forward flight. This problem can be approached as an extension of the hover flap-lag analysis to forward flight or as the addition of the lead-lag degree of freedom to the analysis of flapping stability at high forward speed.

In principle, the analysis of flap-lag stability in forward flight could be performed by analyzing the time history traces from any of the so-called global rotor response programs. In practice, however, these programs are not satisfactory for obtaining blade damping characteristics over a wide range of configuration parameters. First, the computation time required for these programs is considerable and prohibits a detailed and systematic variation of all significant parameters. Second, the blade transient response is obscured by the blade forced response, which often drifts considerably during one or two rotor revolutions. Third, traditional log-decrement methods of damping determination are not applicable in forward flight because of the effect of the periodic coefficients. Thus, most investigations of blade stability in forward flight treat simplified sets of equations that can be systematically analyzed.

Several papers consider the problem of flap-lag stability in forward flight. Reference 4 analyzes the modal equations for a semi-articulated rotor; Refs. 5-8 treat a centrally hinged rigid blade model of a hingeless rotor; and Refs. 9-10 study the modal equations for an elastic blade. Most of these studies, however, concentrate on flap-lag dynamics at very high advance ratios, and only a few damping plots are provided for the moderate range of advance ratios. Furthermore, these investigations contain various theoretical deficiencies that limit the validity of their respective conclusions. For example, Refs. 4-6 and 8-10 fail to account for the decrease in induced flow that necessarily accompanies an increase in forward speed at constant thrust. References 4-10 do not include the proper variations of rotor equilibrium in forward flight. These variations include changes in coning angle and cyclic flapping angles for untrimmed rotors as well as changes in shaft angle, collective pitch, and cyclic pitch for trimmed rotors. Finally, Refs. 4-10 do not include all first order aerodynamic stiffness terms. The omitted effects of induced flow, rotor equilibrium, and aerodynamic stiffness significantly influence rotor blade lead-lag damping at low advance ratios.

The purpose of this paper is to extend the flap-lag analysis of Ref. 1 into the forward flight regime. A derivation of the nonlinear equations of motion for a centrally hinged rigid blade is outlined with special attention given to the aerodynamic terms that are influenced by forward flight. The effects of induced flow, blade equilibrium, and aerodynamic stiffness are retained; and the equations are solved using Floquet theory. Various commonly used approximations for the equations of motion are compared with the complete equations to determine the effect of mathematical modeling on lead-lag damping. The basic lead-lag damping trends at low advance ratios are studied for various trim and operating conditions. Finally, the effects of major rotor parameters on flap-lag stability boundaries are studied.

ANALYSIS

The equations of motion are derived for the idealized model of a hingeless rotor blade treated in Ref. 1. This model consists of a slender rigid blade, hinged at the center of rotation, with spring restraint at the hinge. Aerodynamic forces are based on linear, quasi-steady strip theory; and induced inflow is assumed to be uniform and is obtained from simple momentum theory. Approximate sets of equations are derived for special purposes. The four sets of equations used in this paper are: 1) nonlinear, periodic coefficient equations derived from first principles, 2) linearized perturbation equations derived from the nonlinear equations and used for most of the results of this paper, 3) a simplified version of the perturbation equations obtained by neglecting reversed flow and higher order terms, and 4) constant coefficient equations.

Nonlinear Equations

The coordinate systems used in deriving the flap-lag equations are shown in Fig. 1. The aircraft coordinates (X, Y, Z) are defined with Z along the rotor shaft and X opposite the direction of flight. The rotating coordinates (x, y, z) are obtained by rotating the aircraft coordinates about Z, through an angle $\psi = \Omega t$ where ψ is the rotor shaft angle. For no hinge offsets, the blade position with respect to the rotating coordinate system can be uniquely defined by the three Euler angles $\zeta, \beta,$ and θ. For the simple case of a single set of root hinges, Ref. 1, the Euler angles correspond directly to the hinge rotations in lead-lag, flapping, and pitch. However, for the more complicated double hinge arrangement, described in Ref. 1 in connection with elastic coupling, the
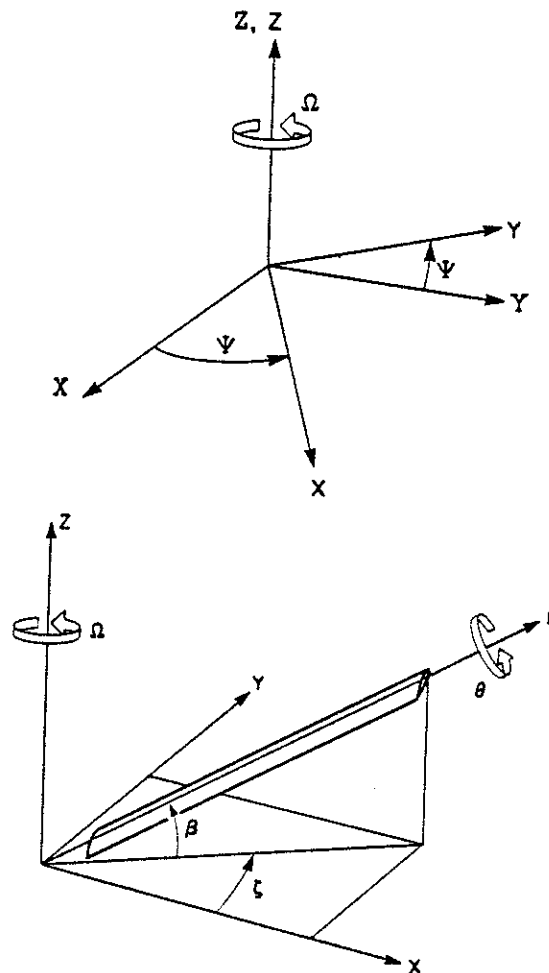

Figure 1. Rotor coordinate systems: aircraft system, rotating system, bladefixed system.

Euler angles do not directly correspond to hinge rotations.

The nonlinear equations of motion for the flap-lag dynamics of this rigid blade model are

$$\ddot{\beta} + \sin\beta\cos\beta\,(1 + \dot{\zeta})^2 + (P - 1)(\beta - \beta_{pc}) + Z\zeta$$

$$= \frac{1}{\Omega^2 I}\int_0^R F_\beta r\,dr = \int_0^1 \bar{F}_\beta \bar{r}\,d\bar{r} \quad (1)$$

$$\cos^2\beta\,\ddot{\zeta} - 2\sin\beta\cos\beta\,(1 + \dot{\zeta})\dot{\beta} + W\zeta + Z(\beta - \beta_{pc})$$

$$= \frac{\cos\beta}{\Omega^2 I}\int_0^R F_\zeta r\,dr = \cos\beta\int_0^1 \bar{F}_\zeta \bar{r}\,d\bar{r}$$

where F_β and F_ζ are the nondimensional airloads perpendicular to the blade and respectively perpendicular to the direction of rotation (flap direction) and parallel to the direction of rotation (lead direction), Fig 2. The elastic terms are approximated by the small β, ζ formulas of Ref. 1 for a double hinge arrangement.

$$P = 1 + \frac{1}{\Delta} \left[\omega_\beta{}^2 + R(\omega_\zeta{}^2 - \omega_\beta{}^2) \sin^2 \theta \right]$$

$$W = \frac{1}{\Delta}[\omega_\zeta{}^2 - R(\omega_\zeta{}^2 - \omega_\beta{}^2) \sin^2 \theta] \qquad (2)$$

$$Z = \frac{R}{2\Delta}(\omega_\zeta{}^2 - \omega_\beta{}^2) \sin 2\theta$$

$$\Delta = 1 + R(1 - R) \sin^2 \theta \, (\omega_\zeta{}^2 - \omega_\beta{}^2)^2/\omega_\zeta{}^2\omega_\beta{}^2$$

This hinge arrangement includes a hub flap and lag spring set that remains aligned with the rotor shaft ($K_{\beta H}$ and $K_{\zeta H}$) and a blade flap and lag spring set that remains aligned with the blade ($K_{\beta B}$ and $K_{\zeta B}$). The second set moves with the blade pitch θ. The parameter R is defined as

$$R \equiv \frac{1/K_{\beta B} - 1/K_{\zeta B}}{(1/K_{\beta B} + 1/K_{\beta H}) - (1/K_{\zeta B} + 1/K_{\zeta H})}$$

and reflects the amount of elastic coupling between flap and inplane. When $\theta = 0$ or $R = 0$, there is no elastic coupling and Eq. 2 reduces to

$$P = 1 + \omega_\beta{}^2 = p^2 \text{ (flap frequency squared)}$$
$$W = \omega_\zeta{}^2 \text{ (lead-lag frequency squared)}$$
$$Z = 0$$

The aerodynamic forces F_β and F_ζ are obtained from quasi-steady airfoil theory. As shown in Fig. 2, the air velocity U and direction ϕ relative to the blade are defined as

$$\phi \equiv \tan^{-1} (U_p/U_t)$$
$$U = \sqrt{U_p{}^2 + U_t{}^2} \qquad (3)$$

where U_p and U_t are the velocity components perpendicular to and parallel to the plane of rotation. The lift and drag per unit length are

$$l = \frac{\rho a c}{2} U^2 \sin \alpha$$
$$d = \frac{\rho a c}{2} U^2 \frac{c_{d_0}}{a} \qquad (4)$$

where ρ is air density, a is the local lift-curve slope, c is the blade chord, and c_{d_0} is the profile drag coefficient. Since $\alpha = \theta - \phi$, Eqs. 3 and 4 yield

$$l = \frac{\rho a c}{2}\sqrt{U_t{}^2 + U_p{}^2}(U_t \sin \theta - U_p \cos \theta)$$
$$d = \frac{\rho a c}{2}(U_t{}^2 + U_p{}^2) \frac{c_{d_0}}{a} \qquad (5)$$

The force components F_β and F_ζ are obtained from Eq. 5 under the assumptions

$$\frac{c_{d_0}}{a}\sqrt{1 + U_p{}^2/U_t{}^2} \approx \frac{c_{d_0}}{a}\left(1 + \frac{1}{2} U_p{}^2/U_t{}^2\right) \text{ and}$$

$$\frac{1}{2}\frac{c_{d_0}}{a}\frac{U_p{}^2}{U_t{}^2} \ll 1$$

nsionless form, they are

$$\bar{F}_\beta = \pm \frac{\gamma}{2}\left[\bar{U}_t{}^2 \sin \theta - \bar{U}_t \bar{U}_p\left(\cos \theta + \frac{c_{d_0}}{a}\right)\right]$$

$$\bar{F}_\zeta = \pm\frac{\gamma}{2}\left[\bar{U}_p{}^2\left(\cos \theta - \frac{1}{2}\frac{c_{d_0}}{a}\right) - \bar{U}_p\bar{U}_t \sin \theta - \bar{U}_t{}^2\frac{c_{d_0}}{a}\right]$$
$$(6)$$

The leading signs of $\bar{F}_\beta$ and $\bar{F}_\zeta$ are taken as positive for forward flow and negative for reversed flow ($U_t \cos\theta + U_p \sin \theta < 0$). The dimensionless velocities, $\bar{U}_t$ and $\bar{U}_p$ are

$$\bar{U}_t = (1 + \dot{\zeta})\bar{r} \cos \beta + \mu \sin (\psi + \zeta)$$

$$\bar{U}_p = \bar{r}\dot{\beta} + \lambda \cos \beta + \mu \sin \beta \cos (\psi + \zeta) \quad (7)$$

where μ is the advance and λ is the inflow including the induced flow ν. Assuming uniform inflow, an equation for ν can be obtained by equating the integrated thrust to the thrust from simple momentum theory.

$$2\nu\sqrt{\mu^2 + \lambda^2} = \frac{\sigma a}{2\pi\gamma}\cos \beta \int_0^{2\pi} \int_0^1 \bar{F}_\beta d\bar{r} d\psi \qquad (8)$$

The induced flow ν is assumed to have a slow reaction time in comparison to one rotor revolution so that only the equilibrium value of $\bar{F}_\beta$ is applied in Eq. 8. Equations 1–2 and 6–8 comprise the nonlinear flap-lag equations with periodic coefficients.

Linearized Equations

For stability analyses, it is convenient to write equations for small perturbation motions about a periodic equilibrium motion of the nonlinear system. The equilibrium values of θ, ζ, and β are designated $\bar{\theta}(\psi)$, $\bar{\zeta}(\psi)$, and $\bar{\beta}(\psi)$. These form the basis of the perturbation expansions.

$$\zeta = \bar{\zeta} + \delta\zeta, \quad \beta = \bar{\beta} + \delta\beta, \quad \theta = \bar{\theta} + \theta_\beta\delta\beta + \theta_\zeta\delta\zeta \quad (9)$$

where θ_β and θ_ζ are pitch-flap and pitch-lag coupling parameters. Positive θ_β or θ_ζ implies that the blade pitches up due to positive flapping or lead inplane motions. The perturbation equations are obtained by substituting Eq. 9 into the nonlinear equations, cancelling the appropriate equilibrium terms, collecting linear terms in $\delta\zeta$ and $\delta\beta$, and neglecting the higher order quantities $\bar{\zeta}, \dot{\bar{\zeta}}, \bar{\beta}^2, \bar{\beta}\dot{\bar{\beta}}$, and $\dot{\bar{\beta}}^2$ with respect to unity in the $\delta\zeta$ and $\delta\beta$ coefficients. As an additional assumption, the boundary of the reversed flow region is assumed to be the circle $\bar{r} + \mu \sin \psi = 0$. It follows that $\bar{\zeta}$ and $\dot{\bar{\zeta}}$ appear only in higher order terms and thus do not appear explicity in the perturbation equations. (Although $\bar{\zeta}$ can effect the couplings θ_β and θ_ζ, this is an implicit dependence

that is treated by appropriately choosing these coupling parameters.)

The perturbation equations described above are used for most of the damping calculations to follow. They are algebraically cumbersome, however, and are not explicitly presented here. Instead, a simplified version of these equations is given in order to obtain an understanding of the contributions of various terms. These simplified equations are obtained by neglecting reversed flow and by letting c_{d_0} and products of $\bar{\beta}$, $\bar{\theta}$, λ, and θ_ζ be neglected with respect to unity. These equations are

$$\begin{Bmatrix} \delta\ddot{\beta} \\ \delta\ddot{\zeta} \end{Bmatrix} + [C(\psi)]\begin{Bmatrix} \delta\dot{\beta} \\ \delta\dot{\zeta} \end{Bmatrix} + [K(\psi)]\begin{Bmatrix} \delta\beta \\ \delta\zeta \end{Bmatrix} = \begin{Bmatrix} 0 \\ 0 \end{Bmatrix} \quad (10a)$$

where

$$[C] = \left[\begin{array}{c|c}
\dfrac{\gamma}{8}\left(1 + \dfrac{4}{3}\mu s\psi\right) & \begin{array}{l} \dfrac{\gamma}{8}\left(\bar{\phi} + \dfrac{4}{3}\mu c\psi\bar{\beta} + \dot{\bar{\beta}}\right) \\[4pt] -2\dfrac{\gamma}{8}\bar{\theta}\left(1 + \dfrac{4}{3}\mu s\psi\right) + 2\bar{\beta} \end{array} \\[18pt]
\hline
\begin{array}{l} -2\dfrac{\gamma}{8}\left(\bar{\phi} + \dfrac{4}{3}\mu c\psi\bar{\beta} + \dot{\bar{\beta}}\right) \\[4pt] +\dfrac{\gamma}{8}\bar{\theta}\left(1 + \dfrac{4}{3}\mu s\psi\right) - 2\dot{\bar{\beta}} \end{array} & \begin{array}{l} \dfrac{\gamma}{8}\bar{\theta}\left(\bar{\phi} + \dfrac{4}{3}\mu c\psi\bar{\beta} + \dot{\bar{\beta}}\right) \\[4pt] +2\dfrac{c_{d_0}}{a}\dfrac{\gamma}{8}\left(1 + \dfrac{4}{3}\mu s\psi\right) - 2\bar{\beta}\dot{\bar{\beta}} \end{array}
\end{array}\right] \quad (10b)$$

$$[K] = \left[\begin{array}{c|c}
\begin{array}{l} P \\[4pt] +\dfrac{\gamma}{8}\left(\dfrac{4}{3}\mu c\psi + 2\mu^2 s\psi c\psi\right) \\[4pt] -\dfrac{\gamma}{8}\theta_\beta\left(1 + \dfrac{8}{3}\mu s\psi + 2\mu^2 s^2\psi\right) \end{array} & \begin{array}{l} Z + \dfrac{\gamma}{8}\mu c\psi\left(\dfrac{3}{2}\bar{\phi} + \dfrac{4}{3}\dot{\bar{\beta}}\right) \\[4pt] -2\dfrac{\gamma}{8}\bar{\theta}\left(\dfrac{4}{3}\mu c\psi + 2\mu^2 s\psi c\psi\right) \\[4pt] +2\dfrac{\gamma}{8}\bar{\beta}\left(\mu^2 c^2\psi - \mu^2 s^2\psi - \dfrac{2}{3}\mu s\psi\right) \\[4pt] -\dfrac{\gamma}{8}\theta_\zeta\left(1 + \dfrac{8}{3}\mu s\psi + 2\mu^2 s^2\psi\right) \end{array} \\[30pt]
\hline
\begin{array}{l} Z - 2\dot{\bar{\beta}} - 2\dfrac{\gamma}{8}\mu c\psi\left(\dfrac{3}{2}\bar{\phi} + \dfrac{4}{3}\dot{\bar{\beta}}\right) \\[4pt] +\dfrac{\gamma}{8}\bar{\theta}\left(\dfrac{4}{3}\mu c\psi + 2\mu^2 s\psi c\psi\right) \\[4pt] -4\dfrac{\gamma}{8}\bar{\beta}\mu^2 c^2\psi + R\theta_\beta(\bar{\beta} - \beta_{pc})(\omega_\zeta^2 - \omega_\beta^2) \\[4pt] +\dfrac{\gamma}{8}\theta_\beta\left[\bar{\phi}\left(1 + \dfrac{3}{2}\mu s\psi\right) + \dot{\bar{\beta}}\left(1 + \dfrac{4}{3}\mu s\psi\right)\right. \\[4pt] \left. +\bar{\beta}\left(\dfrac{4}{3}\mu c\psi + 2\mu^2 s\psi c\psi\right)\right] \end{array} & W
\end{array}\right] \quad (10c)$$

and for convenience of notation $\bar{\phi} \equiv 4/3\ \lambda$. The elastic terms ($P$, W, Z) are obtained from Eq. 2 with $\theta = \bar{\theta}$. If $W \ll 1$, some additional terms may be required in the K_{22} element of the stiffness matrix.

$$K_{22} = W + \dfrac{\gamma}{8}\left[2\dfrac{c_{d_0}}{a}\left(\dfrac{4}{3}\mu c\psi + 2\mu^2 s\psi c\psi\right) + \mu c\psi\bar{\theta}\right.$$
$$\times\left(\dfrac{3}{2}\bar{\phi} + \dfrac{4}{3}\dot{\bar{\beta}}\right) - \bar{\beta}\bar{\theta}\left(\dfrac{4}{3}\mu s\psi + 2\mu^2 s^2\psi - 2\mu^2 c^2\psi\right)$$
$$\left. + 2\mu s\psi\bar{\beta}\left(\bar{\phi}\dfrac{3}{2} + \dfrac{4}{3}\dot{\bar{\beta}} + 2\mu c\psi\bar{\beta}\right)\right] + \dfrac{\gamma}{8}\theta_\zeta\left[\bar{\phi}\left(1 + \dfrac{3}{2}\mu s\psi\right)\right.$$
$$\left. + \bar{\beta}\left(\dfrac{4}{3}\mu c\psi + 2\mu^2 s\psi c\psi\right) + \dot{\bar{\beta}}\left(1 + \dfrac{4}{3}\mu s\psi\right)\right] \quad (10d)$$

For physically reasonable values of W, however, $(.25 < W < 4.0)$ it has been found that these second order aerodynamic stiffness terms may be neglected.

The flap-lag equations are linear differential equations with periodic coefficients. The periodic coefficients can be classified into two groups.

First, there are the explicit periodic coefficients of the form $\mu \sin\psi$ or $\mu \cos\psi$. Second, there are implicit periodic coefficients that result from the fact that $\bar{\theta}$ and $\bar{\beta}$ may have cyclic components. Each type of coefficient appears in both the damp-

ing and stiffness matrices. The elements of the damping matrix that result from forward flight are simply periodic versions of their hover counterparts. The aerodynamic coupling in the stiffness matrix, however, is peculiar to forward flight. Calculations have shown that both the damping and the stiffness terms due to forward flight significantly affect blade damping.

The constant coefficient portion of Eq. 10 is obtained by substituting the Fourier components of $\bar{\theta}$ and $\bar{\beta}$

$$\bar{\theta} = \theta_0 + \theta_s \sin \psi + \theta_c \cos \psi$$
$$\bar{\beta} = \beta_0 + \beta_s \sin \psi + \beta_c \cos \psi$$
$$\dot{\bar{\beta}} = \beta_s \cos \psi - \beta_c \sin \psi$$

into Eq. 10. (Higher harmonics of β have been neglected.) This yields a constant coefficient approximation to the flap-lag equations.

$$[C] =$$

$$\begin{bmatrix} \gamma/8 & 2\beta_0 + \dfrac{\gamma}{8}\left(\bar{\phi} + \dfrac{2}{3}\mu\beta_c\right) \\ & -2\dfrac{\gamma}{8}\left(\theta_0 + \dfrac{2}{3}\mu\theta_s\right) \\ \hline -2\beta_0 - 2\dfrac{\gamma}{8}\left(\bar{\phi} + \dfrac{2}{3}\mu\beta_c\right) & \dfrac{\gamma}{8}\left[2\dfrac{c_{d_0}}{a} + \dfrac{1}{2}\theta_c\beta_s - \dfrac{1}{2}\theta_s\beta_c \right. \\ +\dfrac{\gamma}{8}\left(\theta_0 + \dfrac{2}{3}\mu\theta_s\right) & \left. +\dfrac{2}{3}\mu\theta_c\beta_0 + \theta_0\left(\phi + \dfrac{2}{3}\mu\beta_c\right)\right] \end{bmatrix}$$

(11a)

$$[K] =$$

$$\begin{bmatrix} P - \dfrac{\gamma}{8}\theta_\beta(1+\mu^2) & Z - \dfrac{\gamma}{8}\theta_c(1+\mu^2) \\ & -\dfrac{\gamma}{8}\mu\left(\dfrac{4}{3}\theta_c\right) \\ \hline Z + \dfrac{\gamma}{8}\bar{\phi}\theta_\beta & \\ + R\theta_\beta(\beta_0 - \beta_{pc})(\omega_\zeta^2 - \omega_\beta^2) & W \\ + \dfrac{\gamma}{8}\mu\left(\dfrac{2}{3}\theta_c - \dfrac{4}{3}\beta_s - 2\mu\beta_0\right) & \end{bmatrix}$$

(11b)

In hover, Eq. 11 reduces to the flap-lag coefficients of Reference 1 with two exceptions. First, in Ref. 1, the induced inflow parameter A, corresponding to the present $\bar{\phi}$, is obtained assuming nonuniform inflow. In this paper, $\bar{\phi}$ is obtained assuming uniform inflow, since this is easier to implement in forward flight. Second, Ref. 2 does not include θ_β.

Method of Solution

Blade stability can be calculated for three different equilibrium conditions: untrimmed, moment trim, and propulsive trim. In the untrimmed
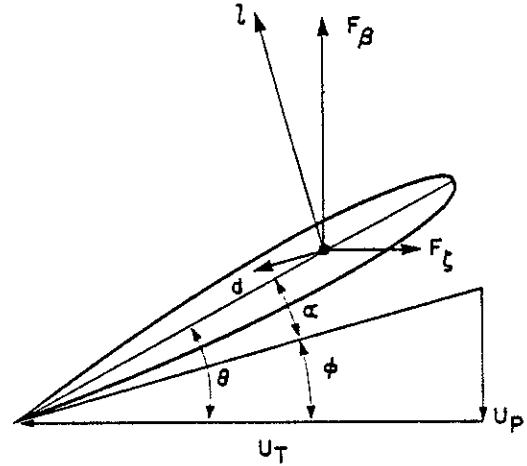

Figure 2. Blade element geometry.

condition, the rotor shaft angle of attack is zero and no cyclic pitch is applied, $\bar{\theta} = \theta_0$. The resulting cyclic flapping generates hub moments in roll and pitch as well as forces in the X and Y directions. The moment trim condition is achieved with cyclic pitch sufficient to suppress first harmonic cyclic flapping, $\bar{\beta} = \beta_0$, and thereby eliminate rotor hub moments. The shaft angle of attack is zero, and rotor forces are approximately vertical since the tip path plane is horizontal. The propulsive trim condition is achieved by balancing the rotorcraft parasite drag with a component of the rotor thrust. This is done by tilting the rotor shaft and also adjusting cyclic pitch to eliminate rotor hub moments. It is assumed that the rotor thrust is perpendicular to the tip path plane. Thus, the inplane component of thrust is neglected. Therefore, the required shaft angle of attack is determined by the following approximate conditions, valid for small angles.

$$T\alpha_s - D = 0 \qquad (12)$$

In terms of dimensionless parameters, the nose down shaft angle required for propulsive trim is, therefore

$$\alpha_s = \frac{\mu^2 \bar{f}}{2C_T} \qquad (13)$$

The corresponding inflow is $\lambda = \nu + \mu\alpha_s$. Most of the calculations in this paper are performed for either the untrimmed or the moment trimmed conditions, the latter being noted as trimmed with $\bar{f} = 0$.

The solution of flap-lag damping for these equilibrium conditions first requires determination of the blade equilibrium conditions $(\bar{\beta}, \bar{\theta}, \bar{o})$. For this paper, the necessary control inputs and the resultant equilibrium are calculated using a har-
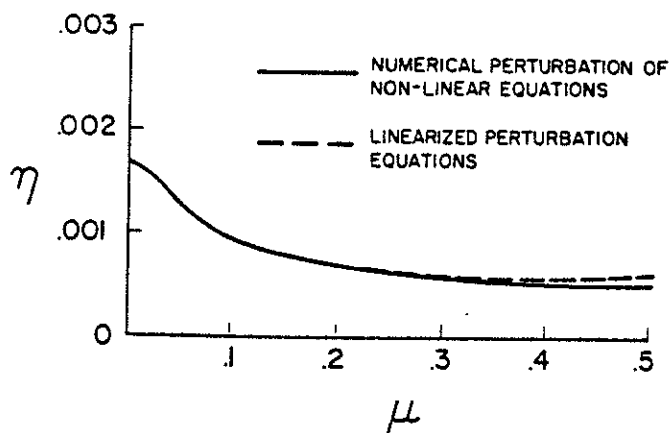
Figure 3. Effect of linearization assumptions on blade damping. $p = 1.15$, $\omega_\zeta = 1.4$, $R = 0$, $\gamma = 5$, $\sigma = 0.05$, $c_{d_0} = 0.01$, $C_T/\sigma = 0.1$, trimmed, $\bar{f} = 0$.

monic balance of the linear flapping equations. These values are checked by numerical integration of the nonlinear equations. Once the rotor equilibrium is established, the stability of the blade about that equilibrium must be determined. Most analytic methods of obraining this damping are based on Floquet theory, and Ref. 4 contains a list of some of these methods. The particular method used here is based on determining the Floquet transition matrix[3], and can be applied to an equilibrium point of nonlinear equations even when the linearized perturbation equations are not known. In such a case, the transition matrix is obtained by numerically perturbing the non-linear equations directly. In other words, the nonlinear equations are treated as an experimental rotor model; and each degree of freedom is perturbed by moving it away from equilibrium. The transient motion of the system as it returns to equilibrium is analyzed using Floquet theory to determine the frequency and damping.

RESULTS

The flap-lag equations discussed above will now be used to generate numerical results that illustrate flap-lag stability characteristics in forward flight. Results are presented in three categories. First, various approximations of the equations are compared with the more complete formulation to determine the effect of mathematical modeling on damping calculations. Second, the basic flap-lag damping trends in forward flight are studied for various trim conditions. This shows the major effects of forward flight on flap-lag stability. Third, damping curves and stability boundaries are presented for a variety of configuration parameters. The baseline calculations are for $p = 1.15$, $\omega_\zeta = 1.4$, $\gamma = 5$, $R = 0$,

$C_T/\sigma = 0.2$, $\beta_{pc} = 0$, $\theta_B = 0$, $\theta_\zeta = 0$, $c_{d_0} = 0.01$, and $\sigma = 0.05$; and variations are given for a range of μ, p, ω_ζ, R, β_{pc}, θ_ζ, and θ_B.

Sensitivity to Math Model

In this section, flap-lag damping calculated from the complete perturbation equations is compared with flap-lag damping calculated from other mathematical models. The damping parameter plotted is η, the negative real portion of the lead-lag eigenvalue; it is positive for stable systems. In Fig. 3, damping is plotted vs. advance ratio for $\omega_\zeta = 1.4$. Two damping curves are given. The first curve is the damping calculated from the linear perturbation equations and the second curve is the damping calculated by numerically perturbing the nonlinear equations as described earlier. The agreement between the two results gives an indication of the validity of the linearizing assumptions

$$\bar{\zeta}, \dot{\zeta}, \bar{\beta}^2, \bar{\beta}\dot{\beta}, \dot{\beta}^2 \ll 1$$

and of the validity of neglecting higher harmonics of $\bar{\beta}$.

$$\bar{\beta} = \beta_0 + \beta_s \sin\psi + \beta_c \cos\psi$$

The comparison indicates that the perturbation equations with truncated $\bar{\beta}$ are an adequate model of the nonlinear equations.

In Figure 4, results from the perturbation equations are compared with results from the simplified equations, Eq. 10, and with results from the constant coefficient equations, Eq. 11. In the simplified equations, reversed flow is neglected and products of θ, $\bar{\beta}$, and $\bar{\phi}$ are considered small with respect to unity. The curves indicate that
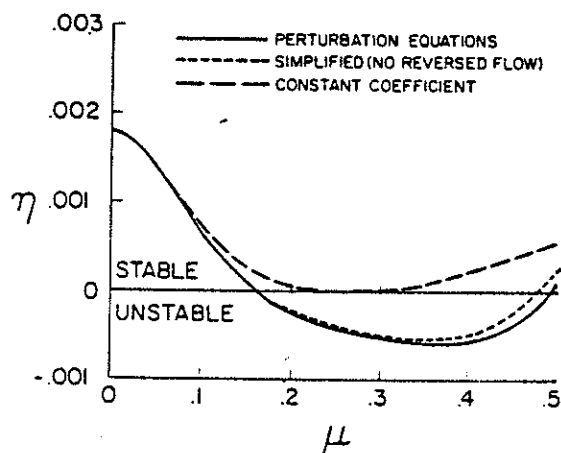

Figure 4. Effect of mathematical approximations on blade damping. $p = 1.15$, $\omega_\zeta = 1.4$, $R = 0$, $\gamma = 5$, $\sigma = 0.05$, $c_{d_0} = 0.01$, $C_T/\sigma = 0.2$, trimmed, $\bar{f} = 0$.
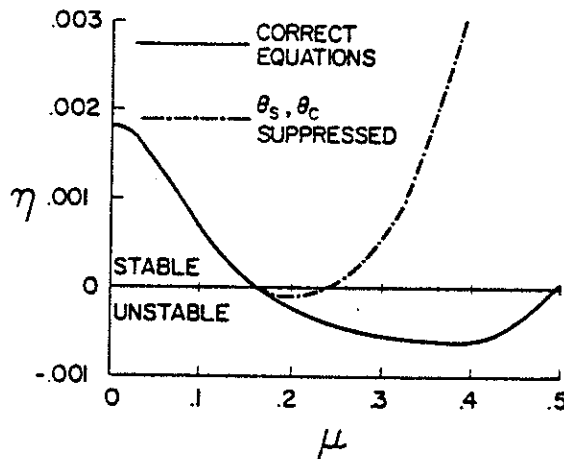
Figure 5. Effect of neglecting cyclic pitch in forward flight. $p = 1.15$, $\omega_\zeta = 1.4$, $R = 0$, $\gamma = 5$, $\sigma = 0.05$, $c_{d_0} = 0.01$, $C_T/\sigma = 0.2$, trimmed, $\bar{f} = 0$.

Figure 6. Effect of equilibrium condition on blade damping. $p = 1.15$, $\omega_\zeta = 1.4$, $R = 0$, $\gamma = 5$, $\sigma = 0.05$, $c_{d_0} = 0.01$, trimmed, $\bar{f} = 0$.

the simplified equations give satisfactory accuracy for $\mu < 0.5$, while the constant coefficient equations give satisfactory accuracy for $\mu < 0.1$. Other calculations, performed over a wide range of parameters confirm these conclusions for $C_T/\sigma < 0.2$. Although the simplified equations provide an adequate approximation, there is little computational penalty is using the complete perturbation equations; and this has been done for the following results.

As stated earlier, the equations of motion contain implicit periodic coefficients, but many investigators have not included the implicit coefficients from cyclic pitch or cyclic flapping. In Fig. 5, the effect of neglecting the cyclic variation in θ is examined. The figure shows that neglecting cyclic pitch for the moment trim condition gives erroneous damping predictions for $\mu > 0.2$. A detailed analysis of this result shows that θ_s and θ_c substantially influence the constant coefficient terms and the periodic terms in the equations. Similarly, it has been found that, for the untrimmed condition, β_s and β_c likewise produce large changes in blade damping. In summary, the effect of the implicit periodic coefficients (θ_s, θ_c, β_s, β_c) is as large as the effect of the explicit periodic coefficients ($\mu \sin\psi$, $\mu \cos\psi$); and both effects contribute substantially to blade stability. It should also be pointed out that periodic variations in $\bar{\phi}$ (e.g., a fore-to-aft inflow variation) were found not to have an important influence on stability.

Effect of Rotor Equilibrium

The differences between the three rotor trim conditions defined above can significantly influence the variation of lead-lag damping with ad-
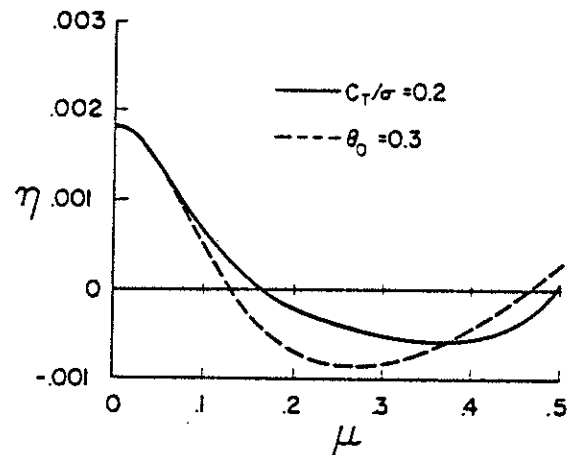
vance ratio. Before these differences are investigated, it is useful to note that constraints on collective pitch and thrust coefficient with advance ratio also influence lead-lag damping. For most of the present results, C_T/σ is held constant as μ varies, corresponding to the usual operating condition of a helicopter. The lead-lag damping for this condition is compared in Fig. 6 with a calculation where θ_0 is held constant with μ. These values of C_T/σ and θ_0 correspond to the same operating condition and the same lead-lag damping when $\mu = 0$; but the operating condition and damping differ considerably for the two cases when $\mu > 0$.

Figure 7 illustrates the effect of the rotor trim condition. Damping curves are presented for the untrimmed moment trim ($\bar{f} = 0$), and propulsive trim with $\bar{f} = 0.01$ conditions. All three condi-
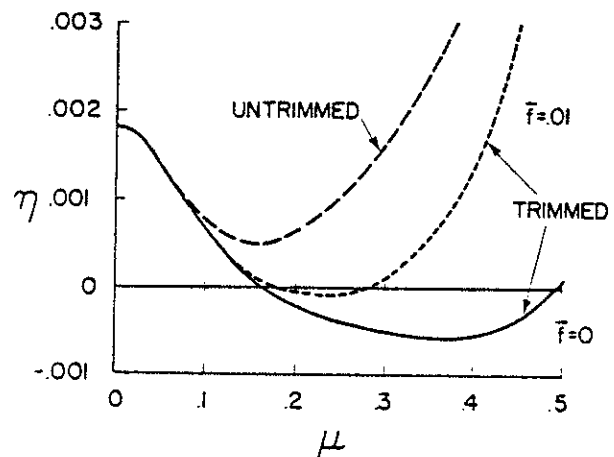

Figure 7. Effect of trim condition on blade damping. $p = 1.15$, $\omega_\zeta = 1.4$, $R = 0$, $\gamma = 5$, $\sigma = 0.05$, $c_{d_0} = 0.01$, $C_T/\sigma = 0.2$.
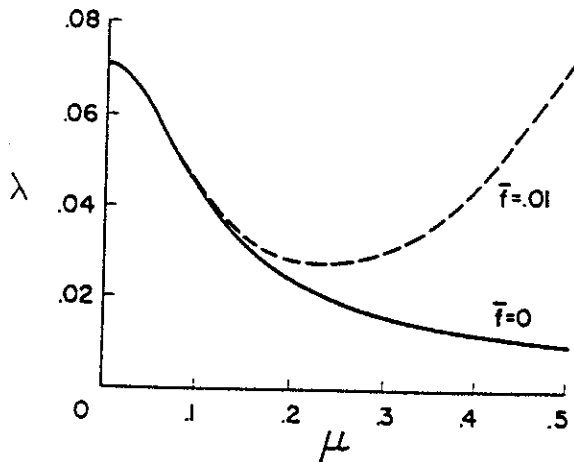
Figure 8. Inflow as a function of advance ratio. $C_T/\sigma = 0.2$, $\sigma = 0.05$, $a = 2\pi$, trimmed.

tions behave similarly at low μ, but significant differences exist at moderate and high μ. These results show that the rotor trim condition substantially influences the lead-lag damping. The variation of induced flow with advance ratio and with propulsive trim is the predominant factor influencing this variation in lead-lag damping at low advance ratios. This can be seen by comparing Figs. 8 and 9. Figure 8 shows the inflow variation with μ for $\bar{f} = 0$ and $\bar{f} = 0.01$. Figure 9 shows the corresponding lead-lag damping and compares it with an additional result in which the inflow is assumed to remain constant with μ. For $\mu < 0.2$, the large reduction in lead-lag damping closely corresponds to the reduction in inflow with μ. At higher μ, the propulsive trim requirement for $\bar{f} = 0.01$ increases the inflow and consequently increases the damping. When the variation in inflow with μ is not accounted

for, the predicted lead-lag damping is relatively constant for low μ. For advance ratios above 0.2, other factors also become important and control the variation of lead-lag damping. At low μ, however, the inflow variation is the predominant effect.

These and the previous results indicate that for $\mu < 0.2$ the effect of inflow is primarily a constant coefficient effect. Therefore, the results for hovering rotors in Refs. 1 and 2 can be used to help interpret the present results. Reference 1 indicates that inflow is stabilizing in the sense that increasing inflow increases θ^*, the pitch angle below which no instability is possible regardless of how p, γ, ω_ζ, and R are chosen (with $\theta_\zeta = \theta_\beta = 0$).

$$\theta^* = \bar{\phi} + 2\sqrt{\frac{2\bar{C}d_0}{a}}$$

For any particular configuration, however, inflow may be either stabilizing or destabilizing depending upon configuration parameters. Reference 2 shows that when C_T/σ (and consequently $\bar{\theta}-\bar{\phi}$ and β_0) is held approximately constant, the lead-lag damping varies quadratically with $\bar{\phi}$

$$\eta - \eta_{min} \sim \left[\frac{\bar{\theta} + \bar{\phi}}{2} - \frac{R(\omega_\zeta^2 - p^2 + 1)}{(\omega_\zeta^2 - p^2)}\right]^2 \quad (14)$$

The least stable condition is when the bracketed term vanishes. Equation 14 shows that for soft inplane rotors ($p^2 - 1 < \omega_\zeta^2 < p^2$) the decrease in $\bar{\phi}$ with μ decreases lead-lag damping. For stiff inplane configurations ($\omega_\zeta > p$) the decrease in $\bar{\phi}$ with μ reduces the lead-lag damping for low values of R but increases it for high values of R.

Effect of Configuration Parameters

The flap-lag stability characteristics of a hinge-less rotor are relatively sensitive to the configuration parameters of the rotor. The following results are intended to illustrate the general trends of these characteristics. In Fig. 10, damping trends are presented for several values of elastic coupling, R. The effect of decreased inflow with advance ratio discussed above is clearly seen for $\mu < 0.2$. The effect destabilizes soft inplane and low R, stiff inplane configurations; but it stabilizes high R, stiff inplane configurations. At higher advance ratios, other effects become important and all configurations are stabilized.

Stability boundaries as a function of p and ω_ζ are shown in Fig. 11 for $C_T/\sigma = 0.2$ and $R = 0$. In hover, the results agree with the conclusions of Ref. 1. For $R = 0$, instability is possible only when $1 < p < \sqrt{2}$ and ω_ζ is close to p. In forward flight, the unstable region is altered to include lead-lag frequencies significantly different from
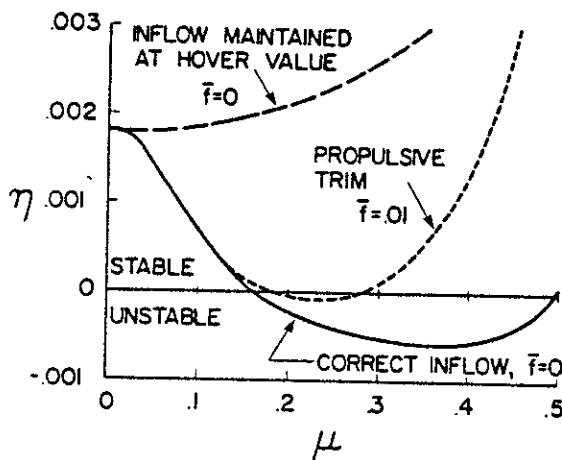

Figure 9. Effect of inflow on blade damping. $p = 1.15$, $\omega_\zeta = 1.4$, $R = 0$, $\gamma = 5$, $\sigma = 0.05$, $c_{d_0} = 0.01$, $C_T/\sigma = 0.2$, trimmed.
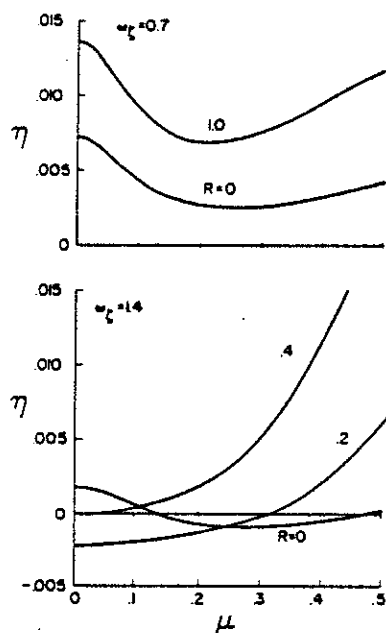
Figure 10. Effect of elastic coupling on blade damping. $p = 1.15$, $\gamma = 5$, $\sigma = 0.05$, $c_{d_0} = 0.01$, $C_T/\sigma = 0.2$, trimmed, $\bar{f} = 0$.

p; and, for sufficiently high μ, instability is also possible for stiff inplane, flap hinged rotors ($p = 1$), which cannot occur in hover.

The effect of elastic coupling on blade stability is given in Fig. 12 where stability boundaries at various advance ratios are plotted for $R = 0, 0.2,$ 0.4. The curves confirm the conclusion of Fig. 11 that forward flight shifts the region of instability to higher lead-lag frequencies. Figure 12 also shows, however, that advance ratio increases the minimum C_T/σ required for instabilities (i.e.,

Figure 12. Effect of lag frequency on stability boundaries. $p = 1.15$, $\gamma = 5$, $\sigma = 0.05$, $c_{d_0} = 0.01$, trimmed, $\bar{f} = 0$. Note: the curves for $R = 0$, 0.2 should be shifted to the left by $\omega_\zeta = 0.2$ units.

the minimum point on the stability boundary). This is especially pronounced for $R > 0$. Thus, no instabilities occur for $C_T/\sigma < 0.11$.

Another interesting aspect of Fig. 12 is the absence of parametric or Hill type instabilities. Theoretically, these instabilities are a potential
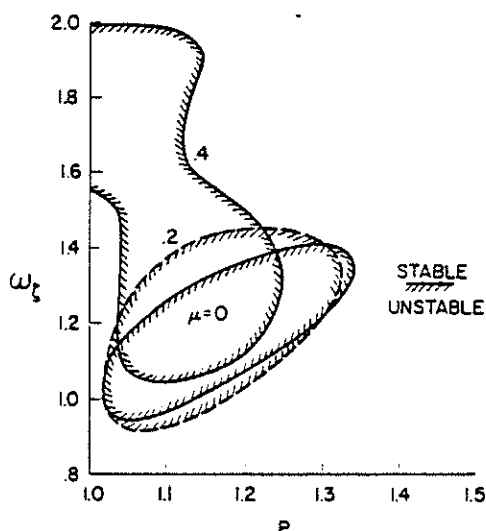
Figure 11. Stability boundaries as a function of flap and lead-lag frequency. $R = 0$, $\gamma = 5$, $\sigma = 0.05$, $c_{d_0} = 0.01$, $C_T/\sigma = 0.2$, trimmed, $\bar{f} = 0$.
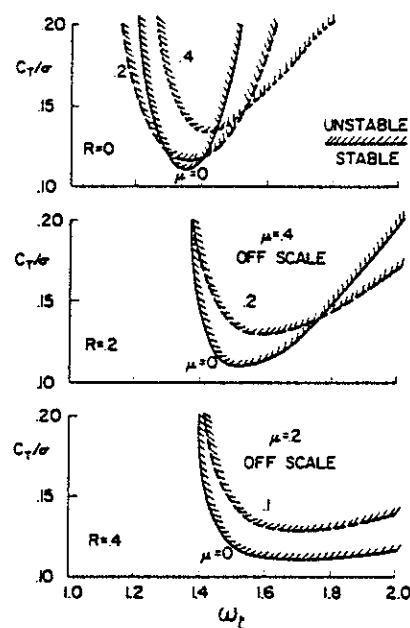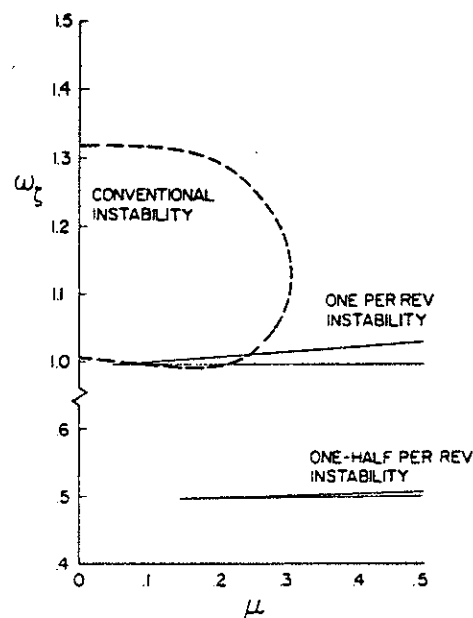
Figure 13. Regions of parametric instabilities. $p = 1.15$, $R = 0$, $\gamma = 5$, $\sigma = 0.05$, $c_{d_0} = 0.01$, $C_T/\sigma = 0.2$, untrimmed.
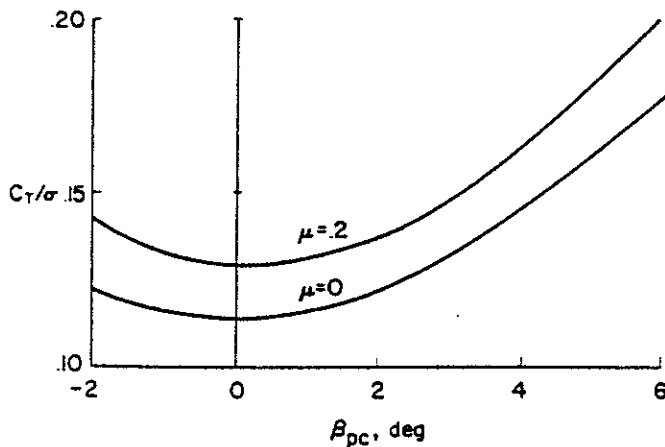
Figure 14. Effect of blade precone on stability boundaries. $p = 1.15$, $\omega_\zeta = 1.4$, $R = 0.2$, $\gamma = 5$, $\sigma = 0.05$, $c_{d_0} = 0.01$, trimmed, $\bar{f} = 0$.

problem whenever ω_ζ is very close to an integer multiple of 1/2 per rev. At low advance ratios, however, the destabilizing parametric terms are very small, and, in most cases, do not appreciably affect stability. The investigations of this study have found for $\mu < 0.5$ only two regions of parametric instability. They occur for the untrimmed rotor with $R = 0$ when ω_ζ is near 0.5 or 1.0, Fig. 13. None occurs for ω_ζ near 1.5. Rotor blades are not generally designed in these regions, however, and parametric instabilities are not a major consideration for $\mu < 0.5$. At higher advance ratios, however, the unstable parametric
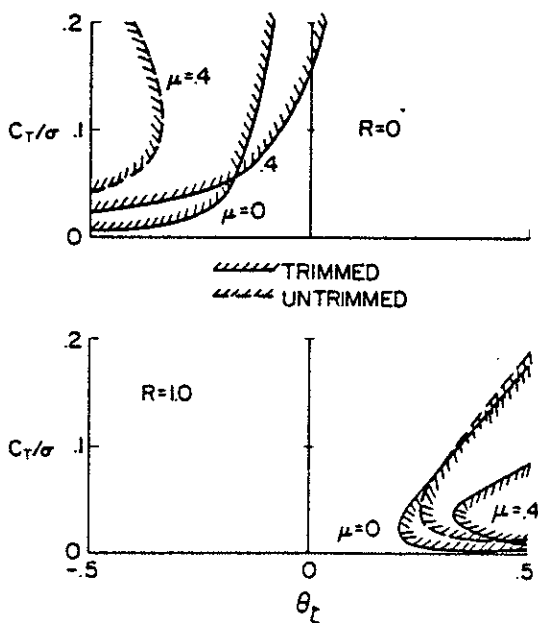

Figure 15. Effect of pitch-lag coupling for stiff inplane configuration. $p = 1.15$, $\omega_\zeta = 1.4$, $\gamma = 5$, $\sigma = 0.05$, $c_{d_0} = 0.01$, $\bar{f} = 0$.
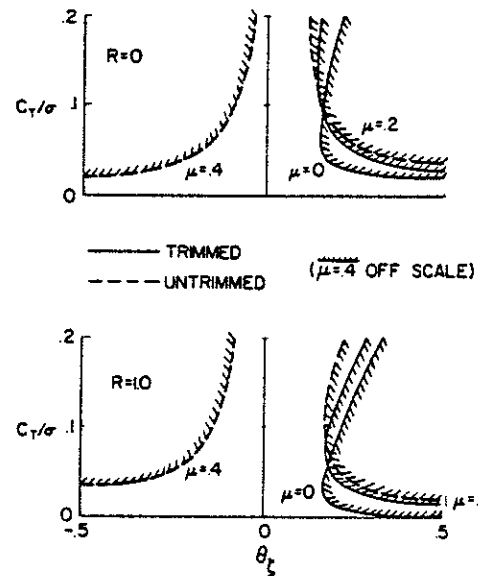

Figure 16. Effect of pitch-lag coupling for soft inplane configuration. $p = 1.15$, $\omega_\zeta = 0.7$, $\gamma = 5$, $\sigma = 0.05$, $c_{d_0} = 0.01$, $\bar{f} = 0$.

regions will expand to include a wider range of ω_ζ values. Thus, parametric flap-lag instabilities may be important at advance ratios much lower than that required for parametric instabilities in flap alone ($\mu \approx 2.25$).

Other configuration parameters that can affect blade stability are Lock number and blade precone. An increase in Lock number causes the aerodynamic terms to increase their relative importance, and it therefore accentuates the effects of forward flight. Blade precone affects the blade equilibrium coning angle and the Coriolis coupling. Figure 14 shows that the effect of β_{pc} in forward flight is qualitatively the same as the effect in hover.

Figures 15 and 16 show the effect of pitch-lag coupling on flap-lag stability boundaries. Figure 15 illustrates the effect for a stiff inplane rotor for the cases of no elastic coupling ($R = 0$) and full elastic coupling ($R = 1.0$). Stability boundaries are significantly different for hover and forward flight, and they are also significantly different for trimmed and untrimmed conditions. The qualitative stabilizing or destabilizing trends with θ_ζ, however, are not affected by advance ratio.

Figure 16 gives a similar comparison for a soft inplane rotor. In this case, however, advance ratio can reverse the stabilizing or destabilizing trend with θ_ζ. As μ is increased from 0 to 0.4, the stability boundaries move from the right half to the left of the θ_ζ plane. Thus, at low values of μ instabilities are encountered at low values of
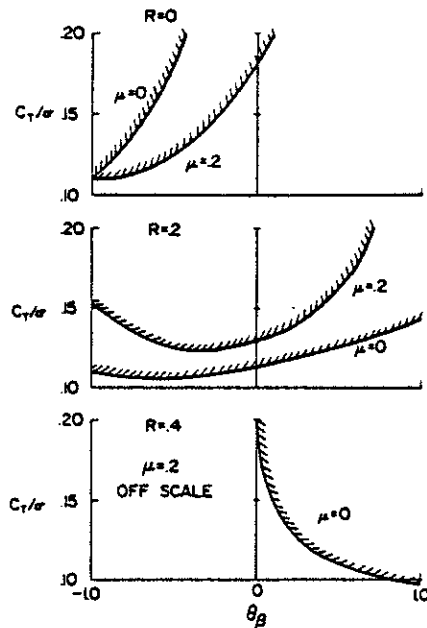
Figure 17. Effect of pitch-flap coupling. $p = 1.15$, $\omega_\zeta = 1.4$, $\gamma = 5$, $\sigma = 0.05$, $c_{d_0} = 0.01$, trimmed, $\bar{f} = 0$.

C_T/σ for positive θ_ζ; at intermediate values of μ instabilities are encountered at high C_T/σ (>0.2) for positive and negative values of θ_ζ; and at $\mu = 0.4$ instabilities are encountered for negative Θ_ζ. For the trimmed condition, the $\mu = 0.4$ stability boundary for negative θ_ζ occurs at values of C_T/σ and θ_ζ beyond the scale of the figure; but the un-trimmed condition exhibits instabilities for low values of C_T/σ and moderate θ_ζ. Thus, the effects of pitch-lag coupling can be reversed from hover to forward flight.

Figure 17 illustrates the effect of pitch-flap coupling on stability boundaries. In hover, the effect is very dependent upon elastic coupling; and either positive or negative θ_β can prove to be destabilizing. In forward flight, the boundaries are significantly changed and negative θ_β (positive δ_3) is generally destabilizing.

CONCLUSIONS

The following conclusions for a single rotor blade can be summarized from the results of this paper.

1. The simplified flap-lag equations without reversed flow, Eq. 10, are good for $\mu < 0.5$; and the constant coefficient equations, Eq. 11, are good for $\mu < 0.1$.

2. Both the implicit periodic coefficients (those due to θ_s, θ_c, β_s, β_c) and the explicit periodic coefficients (those of the form $\mu \sin \psi$, $\mu \cos \psi$) are important for flap-lag stability.

3. For $\mu < 0.2$, the largest effect of forward flight on flap-lag stability is the change in inflow

due to increasing advance ratio. This effect de-stabilizes both soft inplane rotors and those stiff inplane rotors having small elastic coupling.

4. For $0.1 < \mu < 0.5$, periodic coefficients are important for flap-lag stability, but the parametric or Hill type instability is not of practical significance.

5. Flap-lag stability is very sensitive to the moment trim and propulsive trim conditions placed on the rotor.

6. Forward flight tends to increase the least stable value of ω_ζ and decrease the least stable value of p, even to the point of allowing instabilities for $p = 1.0$, Fig. 11.

7. The basic effects of blade precone in forward flight are the same as in hover, Fig. 14.

8. For stiff inplane rotors, advance ratio does not change the qualitative effect of θ_ζ; but for soft inplane rotors, advance ratio can reverse the stabilizing or destabilizing effects of pitch-lag coupling.

REFERENCES

1. Ormiston, R. A. and Hodges, D. H., "Linear Flap-Lag Dynamics of Hingeless Helicopter Rotor Blades in Hover," Journal of the American Helicopter Society, 17, no. 2, Apr. 1972, pp. 2–14.

2. Peters, D., "An Approximate Closed Form Solution for Lead-Lag Damping of Rotor Blades in Hover," NASA TM X-62,425, Apr. 1975.

3. Peters, D. and Hohenemser, K., "Application of the Floquet Transition Matrix to Problems of Lifting Rotor Stability," Journal of the American Helicopter Society, 16, no. 2, Apr. 1971.

4. Bielewa, R., "A Second Order Non-Linear Theory of the Aeroelastic Properties of Helicopter Rotor Blades in Forward Flight," Ph.D. Thesis, Massachusettes Institute of Technology, 1965.

5. Young, M., "A Theory of Rotor Blade Motion Stability in Powered Flight," Journal of the American Helicopter Society, 9, no. 3, July 1964, pp. 12–25.

6. Hohenemser, K. and Heaton, P.W., Jr., "Aeroelastic Instability of Torsionally Rigid Helicopter Blades," Journal of the American Helicopter Society, 12, no. 2, Apr. 1967, pp. 1–13.

7. Hall, E., "Application of Floquet Theory to the Analysis of Rotary-Wing VTOL Stability," Stanford University SUDAAR No. 400, February 1970.

8. Tong, P., "The Nonlinear Instability in Flap-Lag of Rotor Blades in Forward Flight," NASA CR-114524, ASRL TR 166-2, October 1971.

9. Friedmann, P. and Tong, P., "Dynamic Nonlinear Elastic Stability of Helicopter Rotor Blades in Hover and in Forward Flight," NASA CR-114485, ASRL TR 166-3, May 1972.

10. Friedmann, P. and Silverthorn, L., "Aeroelastic Stability of Periodic Systems with Application to Rotor Blade Flutter," AIAA Journal, 12, no. 11, Nov. 1974, pp. 1559–1565.

THE IMPORTANCE OF STEADY AND DYNAMIC INFLOW ON THE

STABILITY OF ROTOR-BODY SYSTEMS

by

David A. Peters
Professor and Chairman
Department of Mechanical Engineering
Washington University
St. Louis, Missouri 63130

THE IMPORTANCE OF STEADY AND DYNAMIC INFLOW
ON THE STABILITY OF ROTOR-BODY SYSTEMS

David A. Peters
Professor and Chairman
Department of Mechanical Engineering
Washington University
St. Louis, Missouri 63130

Abstract

The induced flow field of a rotor responds in a dynamic fashion to oscillations in rotor lift. This has long been known to affect the stability and control derivatives of the rotor. More recently, however, it has also been shown that this dynamic inflow also affects rotor and rotor-body aeroelastic stability. Thus, both the steady and unsteady inflow have pronounced effects on air resonance. Recent theoretical developments have been made in the modeling of dynamic inflow, and these have been verified experimentally. Thus, there is now a simple, verified dynamic inflow model for use in dynamic analyses.

Notation

a = slope of lift curve, per radian

B = tip loss factor

C_{do} = drag coefficient

C_{do}^* = equivalent drag coefficient

C_L = roll moment coefficient

C_M = pitch moment coefficient

C_Q = torque (or power) coefficient

C_T = thrust coefficient

e_{pc} = pocket cut-out divided by radius

$\{F\}$ = vector of loadings

$\bar{f}$ = flat plate drag area over rotor area

k = reduced frequency based on free stream, $= \omega/v$

K_I = apparent inertia coefficient

K_M = apparent mass coefficient

$[L]$ = matrix of inflow gains

$[\mathcal{L}]$ = normalized L matrix

$[M]$ = inflow apparent mass matrix

p = nondimensional flapping frequency

r = nondimensional distance from rotor center, $0 < r < 1$

R_e = elastic coupling parameter

v = mass flow parameter

$\bar{v}$ = nondimensional free stream

V_T = total nondimensional flow at rotor, Table 3

α = pitch angle, angle of incidence, positive nose down

α^* = pitch angle at rotor, $\alpha^* = \sin^{-1}[(\lambda + v)/\mu]$

γ = Lock number

γ^* = equivalent Lock number

υ = nondimensional free-stream velocity

υ^* = free-stream velocity at rotor, $\upsilon^* = \sqrt{\mu^2 + (\lambda + v)^2}$

δ = axis of minimum damping

η = inplane damping

θ = total pitch angle

θ_o = collective pitch

θ_s, θ_c = cyclic pitch

λ = normal freestream component, $\lambda = \upsilon\sin\alpha$

λ_o = total uniform inflow, $\lambda_o = \lambda + \bar{v}$

λ_c = fore-to-aft steady gradient

μ = advance ratio, $\mu = \upsilon\cos\alpha$

v = total induced flow

v_o = uniform induced flow

v_s = side-to-side induced flow gradient

v_c = fore-to-aft induced flow gradient

ξ = axis along free stream

σ = rotor solidity, real part of eigenvalue

[τ] = matrix of inflow time constants

ϕ = inflow angle

ϕ_s = side-to-side gradient in inflow angle

ω = excitation frequency, imaginary part of eigenvalue, per rev

ω_ζ = inplane frequency, per rev

Ω = rotor speed, rpm

$(\bar{})$ = average value

$(\tilde{})$ = perturbation value

Introduction

Almost everyone would agree that the induced flow field of a rotor is an important contributor to the performance and vibrational characteristics of that rotor. What is less well known, however, is that the induced flow field of a rotor is also an important contributor to the aeromechanical stability of that rotor. The contribution of induced flow to stability is manifested in two ways. First, the steady induced-flow field affects the equilibrium flapping angles, the cyclic pitch, and the inflow angles of the rotor. These, in turn, impact directly upon aeromechanical stability. Second, the induced flow field responds (in a dynamic fashion) to oscillations of the rotor; and this inflow response can fundamentally change the damping of the rotor oscillation. Because of the important influence of unsteady induced flow, a good deal of effort has gone into the modeling of dynamic inflow for helicopter applications. This paper examines the history of this modeling effort including the latest developments and experimental verification.

Steady Inflow

The major contribution of steady inflow to rotor damping can be understood in terms of the axis of minimum damping, as shown in Figure 1. In the top figure, we see an airfoil pitched at an angle θ with the relative air flow impinging at an angle ϕ. The vertical direction is flap and the inplane direction is lead-lag. It turns out that the least stable direction of motion is at $(\theta + \phi)/2$, Reference 1. In other words, a coupled flap-lag mode with a principle direction of motion at $(\theta + \phi)/2$ will have the least damping of all modes. The physical basis for this "minimum damping" is illustrated in the lower part of the figure. The blade lift is always perpendicular to the direction of air flow. Thus, a blade motion directed along an axis δ creates an increased lift which is opposite to the direction of motion-damping. However, if δ is larger than ϕ, then lift is in the _same_ direction as the

motion and can create negative damping. The maximum negative contribution occurs at $\delta = (\theta + \phi)/2$.

Now, it is clear that the induced flow directly affects the angle ϕ. Thus, induced flow can either move the axis of minimum damping closer to the modal axis (which is destabilizing) or further from the modal axis (which is stabilizing).

The mathematical description of this phenomenon is given by

$$\eta = \eta_0 + \left[\frac{\theta + \phi}{2} - \frac{R_e(\omega_\zeta^2 - p^2 + 1)}{(\omega_\zeta^2 - p^2)} \right]^2 \quad (1)$$

The negative real portion of the inplane eigenvalue is η and is a measure of inplane damping. Here, we see that there is a contribution to this damping that is minimum when $(\theta + \phi)/2$ is equal to the direction of blade motion. The modal direction depends upon the elastic coupling (R_e) and upon the difference between the inplane and flapping stiffnesses $(\omega_\zeta^2 - p^2)$. For a stiff inplane rotor, $\omega_\zeta^2 > p^2$, the worst case is at a positive $\theta + \phi$. For soft inplane rotors, $p^2 - 1 < \omega_\zeta^2 < p^2$ (including those with matched-stiffness $\omega_\zeta^2 = p^2 - 1$), the worst case is for $\theta + \phi$ negative. This occurs during autorotational descent and partially accounts for the fact that autorotation is often the most critical air-resonance condition.

The effect of induced flow on inplane damping turns out to be the most powerful effect that forward flight exerts on inplane damping. To be more specific, the decrease in induced flow (that accompanies forward speed) and the tip-path tilt (that is used for propulsive force) both combine to significantly change the inflow as a function of μ. Figure 2, taken from Reference 2, depicts inplane damping as a function of advance ratio. The figure shows a sharp drop in damping with μ. When the μ-related changes in induced flow are ignored, however, as shown in the top curve, this loss of damping is not predicted. Therefore, we conclude that the major effect of advance ratio is the drop in ϕ (and hence the movement of the axis of minimum damping). In fact, up to $\mu = .25$, most of the effect of forward flight can be included by a hover analysis with inflow appropriately changed to account for forward flight. When propulsive trim is included (the short-dashed curve), the rotor shaft tilts forward with advance ratio to overcome fuselage drag. This tends to increase inflow and, therefore, to cancel the lower induced flow. Thus, for $\mu > .25$ the damping again increases.

102

A similar phenomenon is manifested in wind turbine (or autorotatinal) damping, as shown in Figure 3, taken from Reference 3. Here, the wind-speed ratio directly affects φ, which results in minimum damping at a particular velocity. The same can be said of wind-turbine damping versus power coefficient, as seen in Figure 4. At a particular value of C_Q, the induced flow is such as to make the damping a minimum.

Thus far, we have considered only the uniform (or average) value of induced flow. It is also interesting to investigate the effect of gradients in the induced flow field. The Figure 5 compares inplane damping for the case of no gradients ($\lambda_c = 0$) with that for the case of a full gradient ($\lambda_c = \lambda_0$), which implies zero induced flow at the leading edge of the rotor disc and maximum induced flow at the trailing edge. One can see that there is only a minor variation in damping between the two cases. Even in hover (for which no gradient physically exists), the effect is small. Thus, fore-to-aft gradients are not important in the context of the effect of steady induced flow on inplane damping.

In Figure 6, we see the effect of a side-to-side gradient on inplane damping. A wind turbine is chosen, for which such gradients occur due to the earth's boundary layer. Here, there is some effect on stability at moderate μ. The reason for this is straight-forward. Changes in φ from fore-to-aft generally cancel in terms of damping. Side-to-side gradients, on the other hand, tend not to cancel due to the large changes in relative free-stream velocity in forward flight. Thus, induced flow gradients are more important in the lateral direction than in the longitudinal; but neither effect is very large.

Early Work In Dynamic Inflow

In the preceding development, we have seen that the steady induced-flow field has a significant effect on blade damping. We now turn our attention to the effect of unsteady fluctuations in the flow field (dynamic inflow). To begin, it might be good to review the past developments in this area. In 1950, Ken Amer noted that the pitch-rate damping of a helicopter depends upon the thrust coefficient in a repeatable, quantitative fashion, Reference 4. In 1952, G. J. Sissingh successfully showed that this measured effect is due to a transient behavior of the induced flow, Reference 5. That is, a roll-rate of a helicopter causes a side-to-side gradient in lift which creates roll damping. However, the formation of this lift gradient also creates an induced-flow gradient that partially negates the lift gradient that finally develops. (This is the effect of dynamic inflow.) Since the induced flow depends greatly upon the mass flow through the rotor, there is a strong C_T dependence,

as measured by Amer. In related work, Reference 6, Carpenter and Fridovitch developed experimental and theoretical results that related to how quickly induced flow follows a change in lift (i.e., a time constant). They found that the time delay could be modeled satisfactorily by the apparent mass of an impermeable disk, as developed in Reference 7. Therefore, by 1953, researchers had identified both the effect of transient inflow and the effect of apparent mass. These two pieces (the induced flow due to lift perturbations and the related time constants) form the kernel of all subsequent work in dynamic inflow.

The early work of these researchers was picked up by several investigators in the early 1970's. This later work concentrates on stability and control derivatives as well as forced response (both of which are dramatically affected by the dynamic inflow phenomenon identified by Sissingh). In 1970, Pat Curtiss and Norm Shupe included the Sissingh model in their helicopter flight equations, References 8-9. (This was a quasi-steady model, and no time constants were used.) The work of Curtiss and Shupe points out that the quasi-steady effect of induced flow in pitch and roll can be accounted for by a simple reduction in the lift coefficient (i.e., by an equivalent Lock number). In other words, changes in lift produce changes in inflow which _lower_ the expected change in lift. Thus, we have an equivalently lower lift-curve slope and lower gamma.

In 1972, Ormiston and Peters took the Sissingh-Shupe model and extended it to include plunge, pitch, and roll for combinations of lift, climb, and forward flight, Reference 10. Calculations of control derivatives with this model were then compared with experimental data taken by Dave Sharpe and Bill Kusczynski with a 7-1/2 ft diameter model rotor. The results show that the Sissingh-Shupe dynamic inflow model (based on momentum theory) gives excellent correlation in hover but not in forward flight. Alternative models for forward flight were then suggested, including an empirical model based on curve fitting the measured data.

By 1974, Peters and Ormiston had extended the dynamic inflow models to the unsteady condition (time constants, etc), Reference 11. Sharpe and Kuczynski had obtained experimental frequency-response data both in hover and forward flight, Reference 12; and this data was compared to the theory in Reference 11. At the same time, Hohenemser and Crews were obtaining similar frequency-response data for a very small-scale rotor, Reference 13; and they also compared with theory. Both studies showed a dramatic effect of dynamic inflow. Furthermore, these two independent studies revealed a completely consistent picture of the gains and time constants of dynamic inflow. In hover, they found that momentum theory (combined with the apparent mass of an impermeable disc) captured all of the experimental features. Thus, when these theoretical gains and time constants were combined with the theory, amazing correlation was obtained.

Figure 7 shows an example of this correlation. Here we have the roll moment (on the left) and the pitch moment (on the right) due to an oscillation in θ_s (longitudinal cyclic). Both the amplitude and the phase of the response are given. The circles are experimental data from the 7-1/2 ft rotor. The solid line is the normal theory in which only steady induced flow is taken (no dynamic inflow). The results are presented for frequencies of swashplate oscillation from 0 to 1.2 per revolution and for 4° of steady collective pitch. One notices large, qualitative deviations between the solid, theoretical curve and the experiment, especially in the phase of C_L and in the amplitude of C_M. The discrepancies are largest at small values of ω and decrease for larger values of ω. Perhaps the most significant aspect of the comparison (between the solid line and the data) is the fact that none of our standard analytic excuses could explain the difference. Collective pitch is only 4°, so there is no stall; and the analysis includes several elastic modes in flapping, so that the dynamics are well represented. Thus, the only candidate to improve correlation is dynamic inflow.

The short-dashed curve gives results for a simple, quasi-steady momentum-theory model of dynamic inflow. That is, the dynamic inflow is assumed to follow changes in lift immediately according to simple momentum theory. The result is dramatic. Every single detail of the data is matched for $\omega < .4$ per rev. At larger ω, however, the theory with quasi-steady theory begins to deviate from the experimental result. The reason for this is that inflow actually responds with a time delay. When this unsteady effect is added, however, (the long dashed curve) the new analysis agress at both low and high ω. The time constants used in this amazing correlation are the apparent mass and inertia of an impermeable disc. This yields the nondimensional inertia and mass terms (K_I = .1132, K_m = .8488). This simple theory leads to the correlation shown in both magnitude and phase.

It seems impossible that anyone could study these results and not be convinced that: a) dynamic inflow is an important, physically-based effect, and b) it can be modeled in hover by simple momentum theory with simple apparent mass terms. In general, one would not always admit that a theory is good simply because in improves correlation. In many cases, improvement might simply be luck; because there can be so many unknown effects that one error might coincidentally cancel another. In this case, however, all reasonable errors have been accounted for. Furthermore, the details of the response are so well simulated that coincidence is out of the question. These results establish dynamic inflow as a fundamental cornerstone of rotor analysis.

We now turn from the response of cyclic pitch oscillations and study the response due to shaft oscillations, as shown in Figure 8. Here, we look at the amplitude and phase of roll moment and pitch moment as a result of pitch oscillations. Because of the symmetry in hover, roll oscillations should create responses identical to those due to pitch (except for a 90° phase shift). Thus, both pitch and roll data are plotted together on this figure (circles and dots). Where the two sets of data begin to deviate (ω = .25), a stand resonance is contaminating the results. Below ω = .25, however, the pitch and roll data are consistent. The solid curve represents conventional theory with no dynamic inflow. One is impressed with how poorly it models the response. (C_L with α is in error by several hundred percent.) When either quasi-steady or unsteady dynamic inflow is included, however, the amplitude and the phase are completely captured. This data correlation leads one to believe that an air resonance mode could be very sensitive to dynamic inflow, since such modes occur from 0.2 to 0.5 per rev.

In forward flight, there is also a large effect of dynamic inflow; but it is not well modeled by simple momentum theory. Figure 9 shows response of the same rotor as that of the previous figures, but with μ = .51. C_L due to all three controls is given. Momentum theory (shown by the dashed line) does not at all correlate with the data. The long dashed curve in the figure is a calculation based on an empirically identified model. This model is identified at ω = 0 only. The effect of ω is included by the same apparent mass terms used in hover. Thus, we see an excellent correlation which includes the presence of an anti-resonance (zero amplitude and phase discontinuity) predicted and measured for the θ_s derivative at ω = .4. Thus, dynamic inflow is important even at high advance ratios.

The effect of dynamic inflow and the satisfying correlation shown above are not flukes of one rotor in one wind tunnel. Figure 10 shows data taken by Kurt Hohenemser and Sam Crews with a 20-inch diameter rotor at Washington University, Reference 13. Here, harmonic excitation is applied in the rotating system by a rotating eccentric. The magnitude of flapping angle due to θ is plotted versus the excitation frequency in the rotating system, ω. The squares are the test data, the solid curve is the analysis with no dynamic inflow, and the dashed curve is the analysis including dynamic inflow. The parameters L and τ are chosen to give the best fit of the data, and yet they agree with the values from momentum theory within a few percent. For example, K_I = .113 (momentum), K_I = .112 (Reference 13). Therefore, dynamic inflow is established as an effect independent of rotor site or wind-tunnel characteristics.

In summary, the early work in dynamic inflow concentrates on forced response of rotors. It shows beyond reasonable doubt that dynamic inflow is an important effect. In hover, the quasi-steady inflow is well modeled by momentum theory; but, in forward flight, momentum theory is completely inadequate. In both hover and forward flight, however, the apparent mass of an impermeable disc provides the correct time constants.

Effect On Stability

The superb data correlations given thus far were developed for the forced response of rotors. It was not long, however, before researchers began studying the effect that dynamic inflow might have on the stability and damping of rotor systems. We now mention a few of the developments in this area. In 1976, Bob Ormiston studied the effect on flapping eigenvalues, Reference 14. He discovered the importance of mode type (collective, progressing, regressing) on the effect of dynamic inflow. In 1979, Peters and Gaonkar studied the effect on lead-lag eigenvalues, Reference 15. One of the more interesting aspects of that paper was the introduction of an equivalent drag coefficient. In other words, just as the lowered lift (due to dynamic inflow) can be modeled by a loss in lift-curve slope, even so, the corresponding increase in induced drag (also caused by dynamic inflow) can be modeled by an equivalent increase in C_{d_o}.

In 1982, Gaonkar and several co-authors extended this work to include aeromechanical stability, Reference 16. That same year, Wayne Johnson also used dynamic inflow theory to correlate Bill Bousman's test data, Reference 17. At this point, it might be good to briefly review the findings of each of these papers with respect to the stability and damping of rotors.

First we look, in Figure 11, at the calculation from Reference 14 of the negative real part of the flapping eigenvalue as a function of collective pitch for p = 1.02 and 1.15. With no dynamic inflow, there is a constant value of damping equal to $\gamma/16$, independent of θ_o. When dynamic inflow is included in the analysis, however, one finds two distinct damping values depending upon the mode, progressing or regressing (collective is not included). The difference in damping of the two modes is attributed to the fact that each mode has a different frequency and therefore affects the inflow in a different way. The quasi-steady approximation (shown by the dashed curve) is closer to the regressing mode because that mode is of lower frequency. The results show clearly the large effect of dynamic inflow. The effect is most pronounced for the regressing mode at low collective pitch. Such a plot indicates that one cannot count on flap damping to stabilize ground resonance at low θ_o.

Another interesting aspect is that even the progressing mode, with a relatively high frequency, is affected by dynamic inflow.

Figure 12 shows the real part of the _inplane_ eigenvalue as a function of advance ratio, Reference 15. The solid curve is the theory without dynamic inflow, and the broken curves are the modes with dynamic inflow. We notice that the higher-frequency progressing and collective modes are only moderately affected. The lower-frequency, regressing mode, however, shows a substantial alteration due to dynamic inflow. Thus, we conclude that dynamic inflow has a potentially large effect on inplane damping, and thus on rotor-body damping.

Next we look at calculations of coupled rotor-body modes from Reference 16, as shown in Figure 13. Here we have body roll-mode damping both for an RPM sweep and for a collective-pitch sweep. The dashed-dot curves are quasi-steady theory; and the dashed-only curves are conventional, unsteady theory. The rotor is matched stiffness. The figure on the left shows a fairly uniform effect of dynamic inflow within the RPM range of interest. This effect is about 30%. The right-hand figure gives a collective sweep. As might be expected, the effect of dynamic inflow increases with decreased lift. Again, the theoretical predictions are that dynamic inflow should play a major role in rotor-body damping; and this effect comes from equivalent changes in both flap damping and inplane damping, as we understand from Reference 16.

It fell to Wayne Johnson to finally compare these predictions with experimental data, as shown in Figure 14. This figure presents the real part of the eigenvalue for the pitch-mode damping. The dashed curve is the theory without inflow dynamics, and the solid curve is the theory with inflow dynamics. Dynamic inflow successfully predicts the peak in damping at low Ω and the 25-30% loss of damping at higher values of Ω. Figure 15 shows a similar comparison for roll. Again, the dynamic inflow provides a substantial improvement in correlation.

The previous two figures show that the NASA analytic model does reasonably well in correlation and that dynamic inflow is an important part of that correlation. Therefore, an analysis without dynamic inflow, but that correlated with experimental data, would be suspect, since dynamic inflow is well-documented and damping analyses are not, and since we know that dynamic inflow has an important effect.

For those who might still be skeptical, we present Figure 16, also from Reference 17. This figure compares measured and calculated frequencies as a function of RPM. The astounding part of the comparison is that one of the branches, labeled λ, is the frequency of a mode that is predominantly dynamic inflow. This branch does not even exist when dynamic inflow is not included. With dynamic inflow, however, the branch appears and matches the experimental data nearly perfectly. Thus, we are looking not just at the effect of dynamic inflow _on_ some mode; we are looking at

the measured dynamic-inflow mode, itself, as seen for the first time.

A final comparison with data is given in Figure 17, which represents two of the correlation studies presented at this workshop. One is Wayne Johnson's correlation with the NASA program, and the other is Sheng Yin's correlation with the Bell Helicopter program. In either case, dynamic inflow represents a significant contribution and improves the correlation of the analysis.

Before leaving the stability correlation, we need to make an important point about the role of these correlations in verifying dynamic inflow theories. The point is this. The validity of a particular dynamic inflow theory (or of dynamic inflow as a phenomenon) cannot presently be made on the basis of comparisons with inplane damping or rotor-body stability data. The reason for this is clear. Stability calculations are not yet accurate enough to uniquely distinguish dynamic inflow from other effects. The role of dynamic inflow in such calculations is, however, important. The reason for this is straightforward. First, we know from flapping response that dynamic inflow exists as a phenomenon and that it is important. The accuracy of any dynamic inflow theory can be determined by comparisons with low-lift flapping response data, which is accurate and relatively unhindered by unknown structural or aerodynamic effects. It is this exact same theory that is applied to inplane stability analyses. (There is not one "flapping" dynamic inflow and one "inplane" dynamic inflow.) Therefore, the comparison with stability data does not test the inflow theory. Instead, the dynamic inflow theory is included in the analysis in order to see the effect of dynamic inflow and to verify the analysis package. This is why we said earlier that a theory that correlates without dynamic inflow would be suspect. Such a theory must have two errors that are cancelling. One error is the omission of dynamic inflow, and the other error is the unknown omission that is somehow cancelling the inflow effect.

Momentum-Theory Formulation

In the early portions of this paper, we briefly reviewed the early work in dynamic inflow; but we did not go into detail as to the exact mathematical formulations used. In this section, we consider these formulations in more detail. The vast majority of the work in this area has been based on simple momentum theory. In hover, this implies that each elemental section of rotor area is treated independently. Then, for each section, the thrust is set equal to the product of the mass flow through the element and the total change in velocity in the associated stream tube. The next step in the analysis (and this is crucial to the theory) is to average the loads and induced flow over the rotor disc. In other words, the theory of dynamic inflow does not concern itself with

details of either load distribution or induced flow distribution. It concerns itself, rather, with global averages. This further implies that the induced flow is treated more as a large mass of air rather than as individual vortices.

As a simple example, we consider the average induced flow ν due to the total thrust coefficient, C_T

$$C_T = 2\nu^2 \qquad (2)$$

Equation (2) is nonlinear in ν. Usually, however, we consider perturbations about a steady condition $(\bar{C}_T, \bar{\nu})$. Thus, we have for the quasi-steady case

$$C_T = \bar{C}_T + \tilde{C}_T \qquad (3a)$$

$$\nu = \bar{\nu} + \nu_o \qquad (3b)$$

$$\bar{C}_T = 2\bar{\nu}^2 \qquad (4a)$$

$$\tilde{C}_T = 4\bar{\nu}\nu_o \qquad (4b)$$

Equation (4b) is the typical perturbation relation between charges in thrust, C_T, and charges in uniform inflow, ν_o. In a more general formulation, we may add cyclic variations in lift (i.e. roll and pitch moments) and cyclic variations in induced flow

$$\nu = \bar{\nu} + \tilde{\nu} \qquad (5a)$$

$$\tilde{\nu} = \nu_o + \nu_s r\sin\psi + \nu_c r\cos\psi \qquad (5b)$$

where ν_s and ν_c are induced flow gradients. Simple momentum theory gives

$$\tilde{C}_T = 4\bar{\nu}\nu_o \qquad (6a)$$

$$\tilde{C}_L = -\bar{\nu}\nu_s \qquad (6b)$$

$$\tilde{C}_M = -\bar{\nu}\nu_c \qquad (6c)$$

Equations (6a-c) represent the momentum theory model in hover used in References 5, 8, 9, 10, 11, 14, 15, and 16.

Although equation (6) works well for hover, it is natural to try to extend the formulation to combinations of thrust, climb, and forward flight. To do this, $\bar{\nu}$ in equations (6a-c) is replaced by $v/2$ where v is a mass-flow parameter. In climb,

v is given by

$$v = \lambda + 2\bar{\nu} = \lambda_o + \bar{\nu} \tag{7}$$

where λ is the inflow due to climb, and λ_o is the total inflow, Reference 8. In forward flight with perfectly edgewise flow and no lift, we have

$$v = \mu \tag{8}$$

as given in Reference 9 and 10, (although forward flight certainly stretches the assumptions of momentum theory to the extreme).

Most investigators agree on the formulations of equations (7) and (8), but a more difficult problem is the transition from hover to edgewise flow. If we consider a freestream velocity υ and a rotor incidence α, then the relative flow is given by

$$\mu = \upsilon \cos \alpha \tag{9a}$$

$$\lambda = \upsilon \sin \alpha \tag{9b}$$

$$\upsilon = \sqrt{\mu^2 + \lambda^2} \tag{9c}$$

If we then add the induced flow, we obtain for the flow at the rotor disc

$$\lambda_o = \upsilon \sin\alpha + \bar{\nu} = \lambda + \bar{\nu} \tag{10a}$$

$$\upsilon^* = \sqrt{\mu^2 + (\lambda + \bar{\nu})^2} = \sqrt{\mu^2 + \lambda_o^2} \tag{10b}$$

$$\alpha^* = \tan^{-1}\left(\frac{\lambda + \bar{\nu}}{\mu}\right) = \tan^{-1}\left(\frac{\lambda_o}{\mu}\right) \tag{10c}$$

The real problem is to relate v to μ, λ, and $\bar{\nu}$.

In References 9 and 18, this is accomplished by the following ad hoc formula

$$v = \upsilon + 2\bar{\nu} \sin \alpha = \frac{\mu^2 + \lambda^2 + 2\bar{\nu}}{\sqrt{\mu^2 + \lambda^2}} \tag{11}$$

Equation (11) gives the correct value of v in hover ($\mu = 0$, $v = \lambda + 2\bar{\nu}$); but for edgewise flow, equation (11) gives an inconsistent result ($\lambda = 0$, $v = \mu$). Now, $v = \mu$ <u>is</u> correct for edgewise flow with <u>no lift</u>; but the inconsistency is that, for $\lambda = 0$, equation (11) gives no effect of thrust (i.e. of $\bar{\nu}$) in the formula. Thus, in the limit as ($\lambda = 0, \mu \to 0$) we obtain a different value of v than we do for ($\mu = 0$, $\lambda \to 0$). There is a discontinuity in the function at ($\mu = 0$, $\lambda = 0$), and this is unacceptable.

A more reasonable formulation of v is given in Reference 11 from basic principles

$$v = \upsilon^* + \bar{\nu} \sin \alpha^* = \frac{\mu^2 + (\lambda + \bar{\nu})(\lambda + 2\bar{\nu})}{\sqrt{\mu^2 + (\lambda + \bar{\nu})^2}} \tag{12}$$

where υ^* and α^* are the total flow and angle at the rotor including induced flow. Equation (12) is derived from momentum principles (not on an ad hoc basis) and provides a much more reasonable formulation of the transition between hover and forward flight. When v is represented by equation (12), it is always positive (with no singularities) except at the vortex-ring boundary, where $v = 0$, Reference 19.

In more recent work by Johnson, Reference 20, equation (12) is obtained for the C_T relation, equation (6a); but a different formulation is derived for the C_L and C_M relations, equations (6b) and (6c). In particular, Reference 20 uses for C_L and C_M

$$v = \upsilon^* = \sqrt{\mu^2 + (\lambda + \bar{\nu})^2} \tag{13}$$

This is in direct contrast to equation (12). Furthermore, in Reference (20), the v for the C_T relation is altered by use of an "approximation" of equation (12)

$$v = \upsilon^* + \nu\sin\alpha^* \approx \upsilon^* + \lambda + \bar{\nu} = \sqrt{\mu^2 + (\lambda + \bar{\nu})^2} + (\lambda + \bar{\nu}) \tag{14}$$

It is not at all clear why the approximation in equation (14) should be valid. Although Reference (20) states that it is valid "for low inflow ratio," this claim is actually not correct.

Table 1 provides a comparison of equations (11)-(14) at critical flight conditions. There are several interesting comparisons in the table. First, in the hover results, we note the Johnson model for roll and pitch differs by a factor of 2 from all previous work (including Sissingh, Curtiss, Shupe, Ormiston, Peters, and Azuma), even in hover. Since these previous results show such an excellent correlation with flapping data, there can be little doubt that Reference 20 is in error. The source of the error can be quickly traced to a failure to include ν_s and ν_c in the mass flow term of each generic element. Along this same line, Reference 20 mentions agreement with the results of Loewy, Reference 21, as confirmation of the accuracy of the formulation. Reference 21, however, is for a zero-lift climb (no wake contraction). The second row of Table 1 shows that for a climb, equation (13) is acceptable for roll and pitch, giving the correct answer $v = \lambda$. With lift, however, the formulation is incorrect.

The second row of Table 1 also reveals an error in the C_T formulation of Reference 20. Whereas all other formulations (including Reference 21) result in $v = \lambda$, the approximation of equation (14) (from Reference 20) gives $v = 2\lambda$. Here, the error lies in the approximation and not in the original formulation. When the conditions of climb and lift are combined, the third row of Table 1, the error in the formulation of Reference 20 is more clear. The correct value, $\lambda + 2\bar{\nu}$, is the flow speed downstream from the rotor. The two incorrect formulas $(\lambda + \bar{\nu})$ and $2(\lambda + \bar{\nu})$ do not provide any effect of wake contraction, for they treat thrust and climb equally.

Going on with Table 1, we see that all formulations give the same value, $v = \mu$, for zero lift edgewise flow; but when lift is added, row 5, there is a wide range of answers. Only the results of Reference 11 and Reference 20 (C_T) are consistent in the sense that they reduce both to μ as $\bar{\nu} \to 0$ and to $2\bar{\nu}$ as $\mu \to 0$. When we further consider the case of zero lift but with incidence, row 6, the results of Reference 20 (C_T) also fail, which leaves the result of Reference 11 as the only viable choice. (For no lift, only $\sqrt{\mu^2 + \lambda^2}$ makes physical sense.) Finally, the last row of Table 1 gives results for zero normal flow, which can occur in a descent. Here, another failure of Reference 8 is noticed. Thus, the v parameter from Reference 11 is the most logical choice of transition between hover and forward flight in momentum theory. To summarize, its attributes are:

1) Correct limiting behavior in climb, hover, and edgewise flow

2) No singularities

3) Foundation in momentum theory

4) Prediction of vortex-ring boundary

The above discussion has considered only the quasi-steady effect of inflow. (Induced flow is assumed to follow immediately any change in loads.) The concept of momentum theory can also be extended, however, to include the time lag between lift and induced flow. In general, equations (6a-c) can be extended as follows.

$$K_M \, \dot{\nu}_o \;+\; 2v\nu_o \;=\; \widetilde{C}_T \tag{15a}$$

$$K_I \, \dot{\nu}_s \;+\; v/2 \, \nu_s \;=\; -\widetilde{C}_L \tag{15b}$$

$$K_I \, \dot{\nu}_c \;+\; v/2 \, \nu_c \;=\; -\widetilde{C}_M \tag{15c}$$

Here K_M and K_I are time constants associated with the rotor air mass. These can be taken as completely general and identified experimentally, as in References 6 and 13. On the other hand, they can be obtained from first principles by potential flow theory. K_M is developed (in Reference 7) and K_I is found (in Reference 11) in this way.

$$K_M \;=\; \frac{8}{3\pi} \;=\; .8488 \tag{16a}$$

$$K_I \;=\; \frac{16}{45\pi} \;=\; .1132 \tag{16b}$$

In each case, the parameters are based on the apparent mass (or inertia) of an impermeable disc. Equations (15) and (16) form a complete unsteady dynamic inflow theory. With $K_M = K_I = 0$, we recover quasi-steady theory.

One of the most valuable results of momentum-theory inflow dynamics has been the discovery that the quasi-steady theory is tantamount to the use of an equivalent Lock number and drag coefficient, References 9 and 15. The formulation is as follows

$$\gamma^* \;=\; \frac{\gamma}{1 + \dfrac{\sigma a}{8v}} \tag{17a}$$

$$\left(\gamma \, \frac{C_{do}}{a}\right)^* \;=\; \gamma\left[\frac{C_{do}}{a} \;+\; \frac{(\theta - \phi)^2}{1 + 8v/\sigma a}\right] \tag{17b}$$

$$\left(\frac{C_{do}}{a}\right)^* = \frac{C_{do}}{a}\left(1 + \frac{\sigma a}{8v}\right)$$
$$+ \frac{\sigma a}{8v}(\theta - \phi)^2 \qquad (17c)$$

Although equation (17a) was originally derived for rigid flapping only, Reference 22 shows that the formulation is quite general. Therefore, a simplified estimate of the effect of dynamic inflow can be obtained from a simple change of γ and C_{do} in any analysis package.

Another interesting aspect of the γ^* approximation is that it can also be used in unsteady, harmonic response analyses, Reference 11 and 13. In particular,

$$\frac{\gamma^*}{\gamma} = 1 - \frac{1}{1 + \frac{8v}{\sigma a} + \frac{16K_I i\omega}{\sigma a}} \qquad (18a)$$

The crucial parameter may be rewritten as

$$\frac{8v}{\sigma a} + \frac{16K_I i\omega}{\sigma a} = \frac{8v}{\sigma a}\left(1 + \frac{2i\omega K_I}{v}\right) \qquad (18b)$$

Equation (18b) shows that there is a reduced frequency, $k = \omega/v$, associated with dynamic inflow. Therefore, the effect of mass flow, v, can be very complicated since it changes both gain and reduced frequency.

.

More Advanced Formulations

The formulation of equations (15a-c), while being excellent in hover, has proven very poor in forward flight. (For example, it does not allow for a fore-to-aft gradient due to C_T.) For this reason, several attempts have been made to extend the theory. Up to now, all such attempts have been based on a matrix formulation of equation (15).

$$[\tau]\begin{Bmatrix}\dot{v}_o\\\dot{v}_s\\\dot{v}_c\end{Bmatrix} + \begin{Bmatrix}v_o\\v_s\\v_c\end{Bmatrix} = [L]\begin{Bmatrix}\tilde{C}_T\\\tilde{C}_L\\\tilde{C}_M\end{Bmatrix} \qquad (19a)$$

$$[M]\begin{Bmatrix}\dot{v}_o\\\dot{v}_s\\\dot{v}_c\end{Bmatrix} + [L]^{-1}\begin{Bmatrix}v_o\\v_s\\v_c\end{Bmatrix} = \begin{Bmatrix}\tilde{C}_T\\\tilde{C}_L\\\tilde{C}_M\end{Bmatrix}$$

$$(19b)$$

$$[M]\{\dot{v}\} + [L]^{-1}\{v\} = \{F\} \qquad (19c)$$

If we look at equation (19a) and temporarily ignore the "dot" term, we see a quasi-steady inflow law. The various harmonics of inflow (described by a vector, $\{v\}$) are assumed to be linearly proportional to the aerodynamic loads on the blade (such as thrust, roll moment, and pitch moment). These loads are represented by the vector, F. The matrix L is the dynamic inflow matrix and expresses the coupling relationships between inflow and loads. Generally, we consider $\{v\}$ and $\{F\}$ in this equation to be perturbation quantities about some steady inflow and loading distributions.

The term, $[\tau]\{\dot{v}\}$, then represents time constants of the system. These imply that the induced flow does not instantaneously follow perturbations to the loads. The τ-terms imply "unsteady" as opposed to "quasi-steady" inflow theory. In an equivalent form of the general theory, given by the second matrix equation, the system is premultiplied by L-inverse. In this alternative version, the $L^{-1}\tau$ matrix takes on the roll of apparent mass terms, [M]. The crux of all dynamic inflow theories is to find the elements of L and [M]. In the early momentum theory (Sissingh, Curtis, Shupe, and Peters), the M-matrix and the L-matrix were diagonal, 3 x 3 matrices, as given by equation (15). In later work, Reference 10, other [L] matrices were considered based on empirical considerations. These were very successful, but lacked physical foundation. Thus, a need was recognized to find [L] and [M] from more basic theories.

In principle, any induced flow theory that keeps track of the three-dimensional, unsteady vorticity automatically includes dynamic inflow, eg., Reference 21. In practice, however, few present-day programs provide a transient rotor wake analysis. Furthermore, even the steady wake programs are much too cumbersome for use in a dynamics analysis, Reference 23. What is needed, therefore, is some analysis that can be used to obtain [M] and [L] in a simple, usable form. The prime candidate for this analysis is actuator-disc theory. In Reference 24, the first attempt was made to extract dynamic inflow data from an actuator-disc theory. It should be pointed out that many people had used actuator-disc theories to obtain induced flow, but no one had exercised them in the context of obtaining dynamic-inflow derivatives.

Although Reference 23 came a long way toward the desired answer, the analysis became so involved that no definitive results could be obtained. The problem is illustrated by Figure 18. The dynamic inflow theory is just one part of an overall rotor analysis. However, if one tries to identify the inflow law in the presence of blade dynamics and airfoil theories, the problem becomes too complicated for a fundamental solution. What is needed is a look at the open-loop transfer function of dynamic inflow without the complications of blade theory.

The ideal theory for attempting such a derivation is the actuator-disc theory of Mangler and Squire, as applied by Joglekar and Loewy in Reference 25. This theory is based on the Kinner closed-form pressure potentials for an actuator disc. Figure 19 gives a schematic of such a disc in an ellipsoidal coordinate system (ν, η, ψ). The free-stream enters at an angle α, and positive lift is taken in the negative Z direction. Kinner was able to obtain a closed-form potential function to describe an arbitrary pressure discontinuity across the disc. This function is expressed in terms of Legendre functions and can be used to find the induced-flow field for any given loading. Although the theory is successfully applied (in Reference 25) to give a specific inflow distribution, it is not used to find the dynamic inflow matrices.

In Reference 27, Dale Pitt extends the Kinner theory to include unsteady effects and uses it to find the elements of [L] and [M]. Two different radial lift distributions are used to verify that the matrices are not sensitive to the details of blade loading. Table 2 provides the final forms of the matrices as suggested in Reference 26, where [L] takes the form .

$$[L] = \frac{1}{\nu} [L] \qquad (20)$$

The $[L]$ matrix is symmetric with elements that depend only upon the angle of incidence, α. The entire matrix is divided by the free-stream velocity, ν. For forward flight with lift, ν becomes the mass flow parameter of equation (12) and α becomes the local angle, α^*, equation (10c). In axial flow ($\alpha = \alpha^* = 90°$), the $[L]$ matrix reduces to that of momentum theory, a very satisfying result of the theory. Similarly, the M-matrix also agrees with momentum theory for the roll and pitch inertias, although the apparent mass for thrust is different than that of momentum theory when the loading is zero at the rotor center.

In Reference 27, the formulation of Table 2 has been verified by two independent means. First, for the quasi-steady terms, the $[L]$ matrix has been checked against a free-vortex wake analysis written by Landgrebe. The prescribed wake model of Landgrebe is exercised in numerical experiments in which changes in cyclic and collective pitch create changes in induced flow patterns, and these are interpreted in terms of the wake coupling matrix, L. Figure 20 presents the first column of L, inflow due to thrust. The horizontal line is the theoretical value of $L_{11} = 1/2$ that relates thrust to uniform inflow; it is completely independent of lift distribution. The open triangles are results from the wake program and agree within 10%. The long-dashed and dash-dot lines provide the L_{31} term, which is zero in hover ($\alpha = 90°$) and maximum at $\alpha = 0°$. Two different loading distributions are used, labelled "corrected" and "uncorrected." The results from Landgrebe's program are given by squares. (Solid squares indicate convergence problems.) The corrected curve, which enforces zero lift at the center, is very close to the Landgrebe results, and is the formulation used in Table 2. The two solid squares are suspect because no data has ever shown the fore-to-aft gradient decreasing as incidence goes to zero. The L_{21} term is zero for both the theory and the Landgrebe model.

Figure 21 provides a comparison of the second column of L, induced flow due to roll moment. In theory, the only term should be L_{22}, given by the two curves and the triangles. One can see that there is little difference in L_{22} for the two possible lift distributions. Furthermore, the prescribed-wake results agree to within a few percent for $\alpha > 30°$. Therefore, the simpler uncorrected curve is used in Table 2. L_{32} on the other hand (fore-to-aft inflow due to roll moment, shown by squares) is theoretically zero but exhibits a non-zero value from the prescribed wake. The explanation of this is the wake rotation (which is not included in the actuator-disc theory). Fortunately, the effect is not large. L_{12} is zero for both theory and numerical experiment.

When we look at the third column of L, Figure 22, we again see the wake rotation effect $L_{23} = -L_{32} = .2$, ideally zero from actuator-disc theory. The L_{33} term, shown as diamonds, displays an excellent correlation between actuator-disc and vortex models, as does the L_{13} term, shown in triangles. Again, the corrected versus uncorrected pressure distributions do not show an appreciable effect on L, and uncorrected is used in Table 2.

Reference 27 also provides a verification of the unsteady part of dynamic inflow, the M-matrix. In particular, an exact solution of the unsteady, potential flow equations is compared to the simpler approach of a direct superposition of $[L]^{-1}\{\nu\}$ and $[M]\{\dot{\nu}\}$ terms. The result is given in Figure 23 for $L_{22} = L_{33}$ ($\alpha = 90°$) as a function of reduced frequency, $k = \omega/\nu$. For both magnitude and phase, the simple model of equation (19) gives excellent agreement with a more rigorous, Theodersen-type, unsteady theory.

It should also be mentioned here that References 26 and 27 discuss the possibility of using additional radial and azimuthal degrees of freedom in the inflow model, and an expanded 5 x 5 model is explicitly given. In Reference 28, this 5 x 5 model is compared to the 3 x 3 model with respect to its effect on inplane damping. The results show two

things. First of all, the 5 x 5 model gives extraneous answers for rotors with less than 5 blades (as a result of a mathematical indeterminancy). Second, for rotors with 5 or more blades (or for constant-coefficient analyses), the 5 x 5 results are essentially the same as the 3 x 3 results. Therefore, Reference 28 concludes that the 3 x 3 model is adequate and is probably the most sophisticated model that is possible for dynamic inflow in matrix formulation.

With dynamic inflow verified by both experimental and computational data, it is presently ready to be used in dynamics analyses. The theory as it now stands is a perturbation theory and thus applicable to linearized analysis packages. It is easily extended, however, to a nonlinear version for use in time history solutions. Table 3 shows the nonlinear version of L. Here, v_0 represents the total uniform induced flow (steady plus perturbation). You may recall that the linear version of L is divided by v, the mass-flow parameter, equation (20). In the nonlinear version, the first column of L is divided instead by the total mass flow V_T. The mass flow parameter v is simply related to V_T through a derivative as shown. Consequently, the nonlinear L-matrix has perturbation equations identical to those of the linearized dynamic-inflow theory.

Summary

The following statements summarize our present understanding of the importance of inflow to rotor and rotor-body damping.

1. Steady inflow (mostly uniform) is important for inplane damping in that it changes the axis of minimum damping.

2. The largest effect of advance ratio on inplane damping is the associate change in inflow.

3. Dynamic inflow is an important effect on rotor damping, and its importance has been physically verified many times.

4. The effect of dynamic inflow is largest for the low-frequency, regressing rotor-body modes.

5. Presently, the best dynamic-inflow theory is a 3 x 3 closed-form model based on actuator-disc theory. It's accuracy has been verified by comparisons with more sophisticated models.

References

1. Peters, David A., "An Approximate Closed-Form Solution for Lead-Lag Damping of Rotor Blades in Hover," NASA TM X-62,425, April 1975.

2. Peters, David A., "Flap-Lag Stability of Helicopter Rotor Blades in Forward Flight, "Journal of the American Helicopter Society, Vol. 20, No. 4, October 1975, pp. 2-13.

3. Wei, F-S and Peters, D. A., "Lag Damping in Autorotation by a Perturbation Method," Proceedings of the 34th Annual National Forum of the American Helicopter Society, Washington, D.C., May 1978, Paper 78-25.

4. Amer, K. B., "Theory of Helicopter Damping in Pitch or Roll and a Comparison with Flight Measurements," NACA TN-2136, October 1950.

5. Sissingh, G. J., "The Effect of Induced Velocity Variation on Helicopter Rotor Damping in Pitch or Roll," Aeronautical Research Council Paper No. 101, Technical Note No. Aero 2132, November 1952.

6. Carpenter, P. J. and Fridovitch, B., "Effect of Rapid Blade Pitch Increase on the Thrust and Induced Velocity Response of a Full Scale Helicopter Rotor," NACA TN-3044, November 1953.

7. Tuckerman, L. B., "Inertia Factors of Ellipsoids for Use in Airship Design," NACA Report No. 210, 1925.

8. Shupe, N. K., A Study of the Dynamic Motions of Hingeless Rotored Helicopters, Ph.D. Thesis, Princeton, September 1970.

9. Curtiss, H. C., Jr. and Shupe, N. K., "A Stability and Control Theory for Hingeless Rotors," Proceedings of the 27th Annual National Forum of the American Helicopter Society, May 1971, Paper No. 541.

10. Ormiston, Robert A. and Peters, David A., "Hingeless Rotor Response with Nonuniform Inflow and Elastic Blade Bending," Journal of Aircraft, Vol. 9, No. 10, October 1972, pp 730-736.

11. Peters, David A., "Hingeless Rotor Frequency Response with Unsteady Inflow," Rotorcraft Dynamics, NASA SP-352, February 1974, pp 1-13.

12. Kuczynski, W. A. and Sissingh, G. J., "Characteristics of Hingeless Rotors with Hub Moment Feedback Controls Including Experimental Rotor Frequency Response," NASA CR 114427, January 1972.

13. Crews, S. T., Hohenemser, K. H., and Ormiston, R. A., "An Unsteady Wake Model for a Hingeless Rotor," Journal of Aircraft, Vol. 10, No. 12, December 1973, pp 758-760.

14. Ormiston, Robert A., "Application of Simplified Inflow Models to Rotorcraft Dynamic Analysis," Journal of the American Helicopter Society, Vol. 21, No. 3, July 1976, pp 34-39.

15. Peters, David A. and Gaonkar, Gopal H., "Theoretical Flap-Lag Damping with Various Dynamic Inflow Models," Journal of the American Helicopter Society, Vol. 25, No. 3, July 1980, pp 29-36.

16. Gaonkar, G. H., Mitra, A. K., Reddy, T.S.R., and Peters, D. A., "Sensitivity of Helicopter Aeromechanical Stability to Dynamic Inflow," Vertica, Vol. 6, No. 1, January 1982, pp 59-75.

17. Johnson, Wayne, "Influence of Unsteady Aero-
    dynamics on Hingeless Rotor Ground Resonance,"
    Journal of Aircraft, Vol. 19, No. 8, August
    1982, pp 668-673.

18. Azuma, Akira and Nakamura, Yoshiya, "Pitch
    Damping of Helicopter Rotor with Nonuniform
    Inflow," Journal of Aircraft, Vol. 11,
    No. 10, October 1974, pp 639-646.

19. Peters, D. A. and Chen, S. K., "Momentum
    Theory, Dynamic Inflow, and the Vortex Ring
    State," Journal of the American Helicopter
    Society, Vol. 27, No. 3, July 1982, pp 18-24.

20. Johnson, Wayne, Helicopter Theory, Princeton
    University Press, 1980, pp 520-526.

21. Loewy, R. G., "A Two-Dimensional Approxima-
    tion to the Unsteady Aerodynamics of Rotary
    Wings," Journal of Aeronautical Sciences,
    Vol. 24, 1957.

22. Gaonkar, Mitra, and Reddy, "Feasibility of a
    Rotor Flight Dynamics Model with First-Order
    Cyclic Inflow and Multi-Blade Modes,"
    proceedings of the AIAA Dynamics Specialists'
    Meeting, Atlanta, Georgia, April 9-10, 1981,
    p 15.

23. Landgrebe, A. J., "An Analytical Method for
    Predicting Rotor Wake Geometry," Journal of
    the American Helicopter Society, Vol. 14,
    No. 4, October 1969.

24. Ormiston, Robert A., "An Actuator Disc Theory
    for Rotor Wake Induced Velocities," AGARD
    Specialists Meeting on the Aerodynamics of
    Rotary Wings, Marseille, France, September
    13-15, 1972.

25. Joglekar, M. and Loewy, R., "An Actuator-Disc
    Analysis of Helicopter Wake Geometry and the
    Corresponding Blade Response," USAAVLABLS
    Technical Report 09-66, 1970.

26. Pitt, Dale M. and Peters, David A.,
    "Theoretical Predictions of Dynamic Inflow
    Derivatives," Vertica, Vol 5, No. 1, March
    1981.

27. Pitt, Dale M. and Peters, David A., "Rotor
    Dynamic-Inflow Derivatives and Time Con-
    stants from Various Inflow Models, "9th
    European Rotorcraft Conference, Stresa,
    Italy, September 13-15, 1983, Paper No. 55.

28. Gaonkar, et. al., "The Use of Actuator-
    Disc Dynamic Inflow for Helicopter Flap-Lag
    Stability," Journal of the American Helicop-
    ter Society, Vol. 28, No. 3, July 1983,
    PP 79-88.
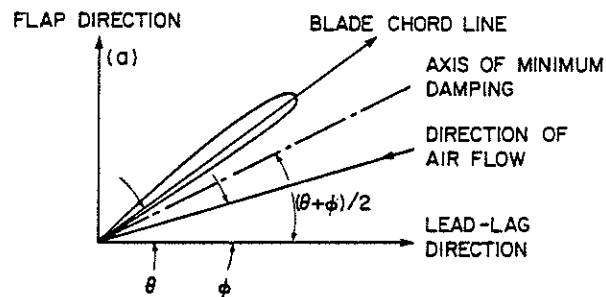
(a) Motion geometry.
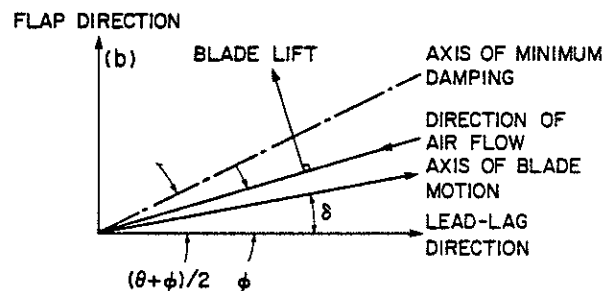
(b) Force geometry.
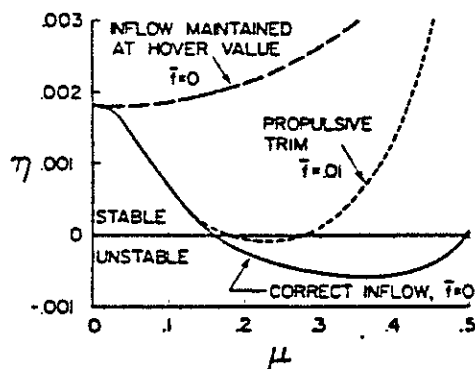
Figure 1. The Axis of Minimum Damping.

Figure 2. Effect of Inflow on Inplane Damping, $p=1.15$, $\omega_\zeta=1.4$, $R_e=0$, $\gamma=5$,
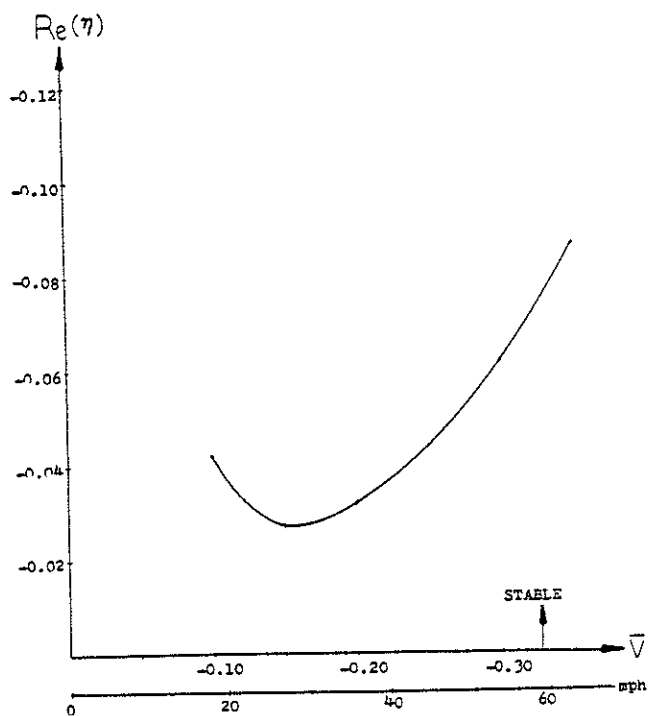$\sigma=.05$, $C_{d_o}=0.1$, $C_T/\sigma=0.2$, trimmed.

Figure 3. Wind Turbine Inplane Damping Versus Wind Speed, $\gamma'=12.3$, $p=2.76$, $\omega_\eta=3.62$, $C_{d_o}=.01$, $C_Q/\sigma=.007$, $\sigma=.0255$, $R_e=1.0$, $\mu=0.0$.

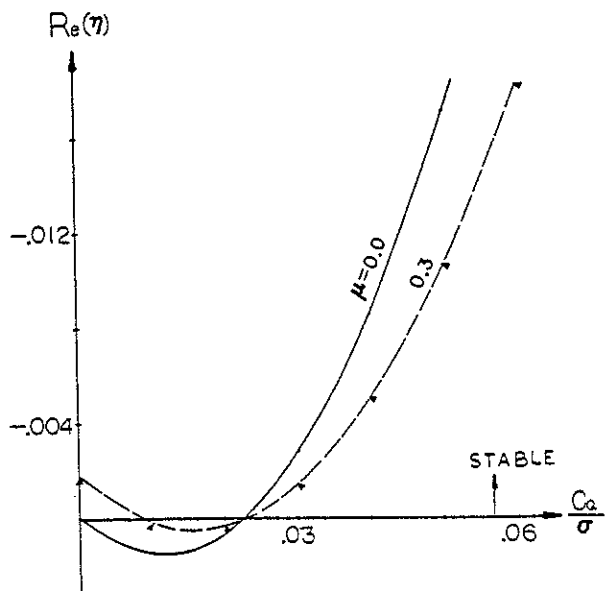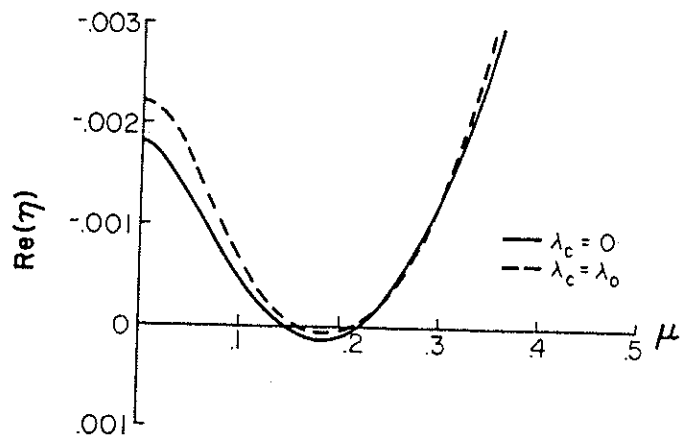Figure 5. Effect of Fore-to-Aft Inflow Gradients on Inplane Damping, $p=1.15$, $\omega_\eta=1.4$, $R_e=0$, $\gamma'=5$, $\sigma=.05$, $C_{d_o}=.01$, $\epsilon_o=0.3$, $\epsilon_s=\epsilon_c=0$.
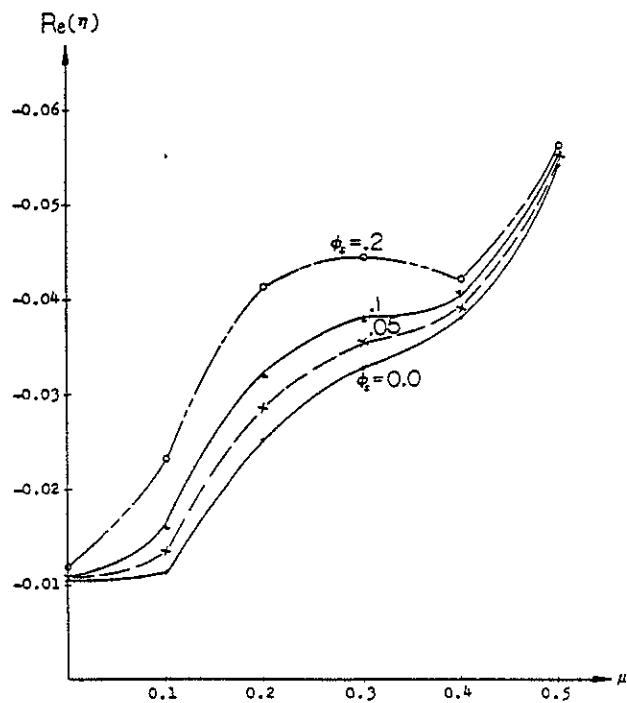

Figure 4. Wind Turbine Inplane Damping Versus Power Coefficients, $C_T=.01$, $\omega_\eta=0.7$, $R_e=0.0$, $\sigma=.05$, $p=1.15$, $\gamma'=5.0$, $C_{do}=.01$.

Figure 6. Effect of Lateral Gradients on Inplane Damping of Wind Turbine, $C_T=.01$, $C_Q/\sigma=.06$, $\sigma=.05$, $p=1.15$, $\omega_\eta=1.4$, $C_{do}=.01$, $\gamma'=5.0$.

113

-13-
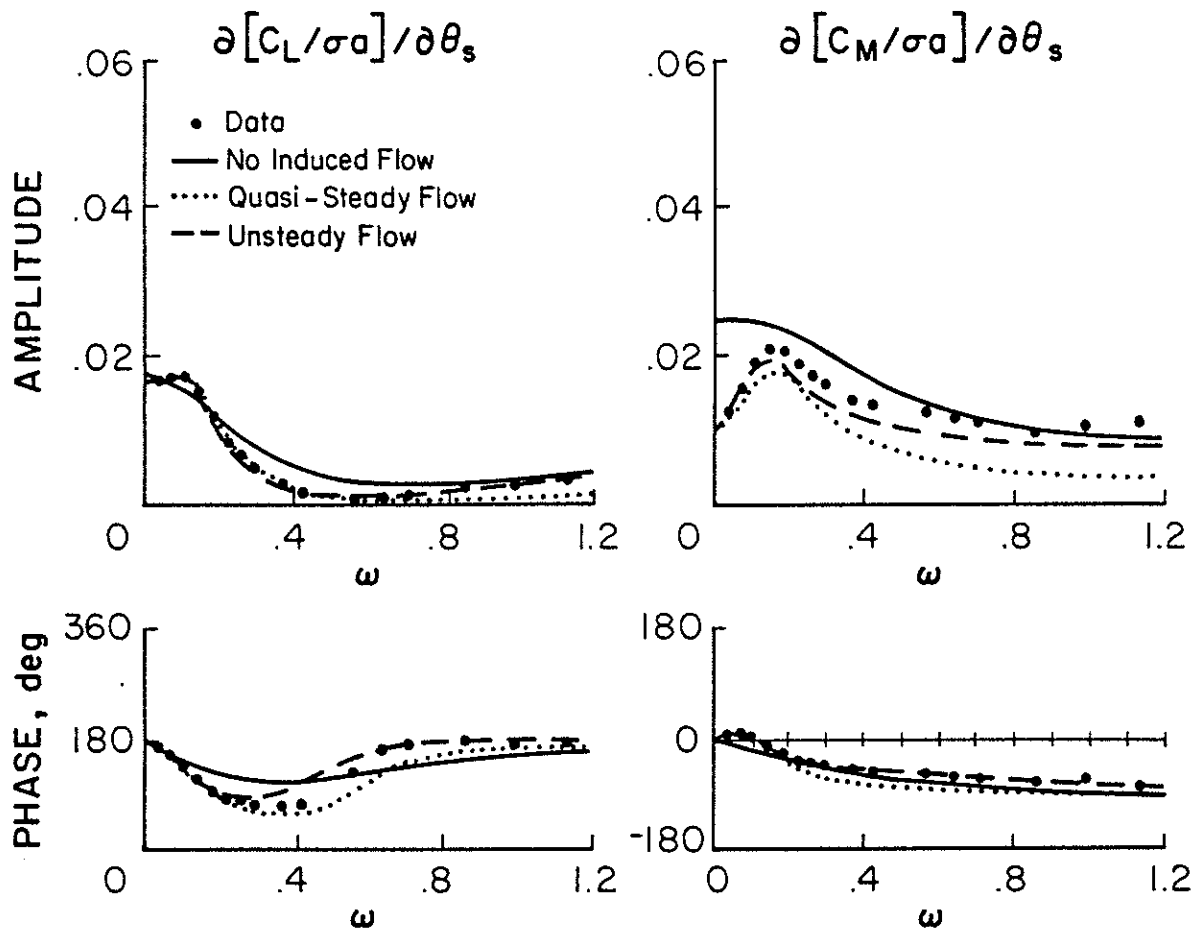
Figure 7. Rotor Response to Cyclic Pitch in Hover, p=1.15, γ =4.25, B=.97, e_{pc} =.25, μ =0, σ a=.7294, $\bar{\nu}$ = $\bar{\lambda}$ =.03, Θ_o =4°, momentum theory, single rotating mode.
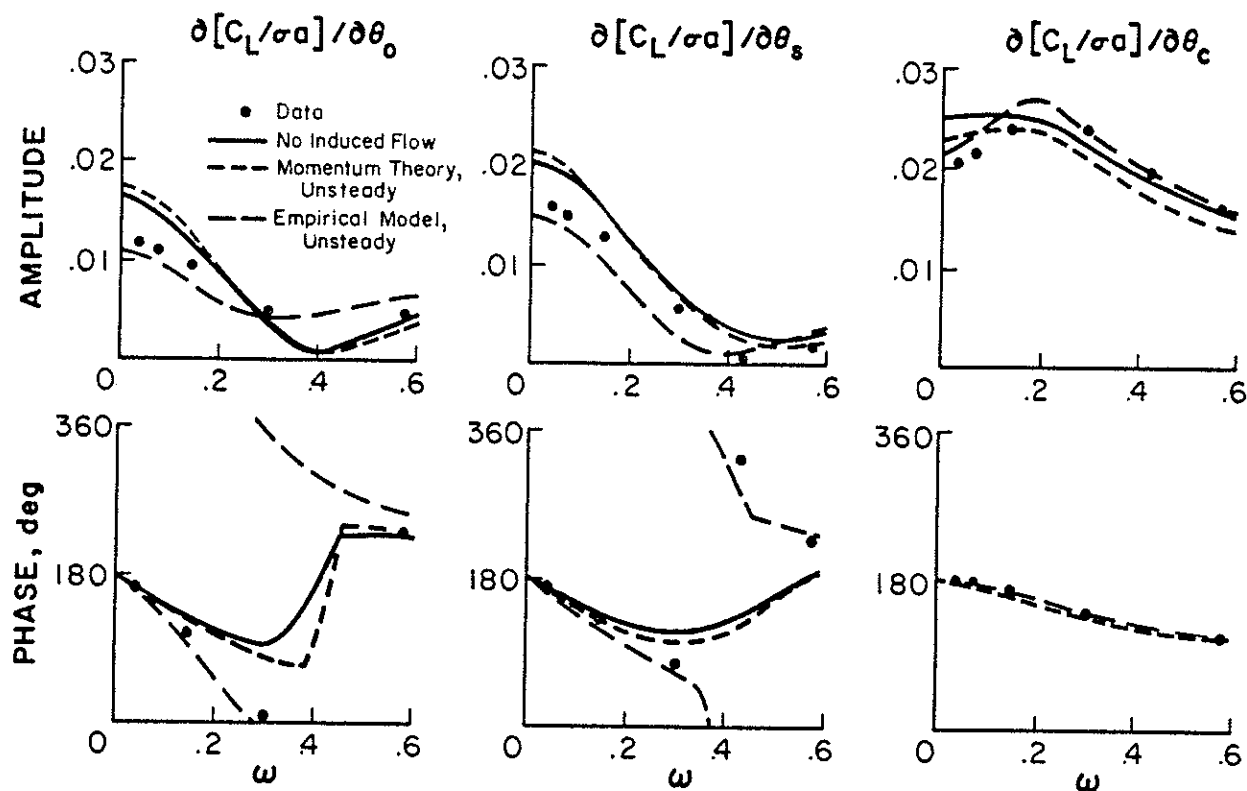
114
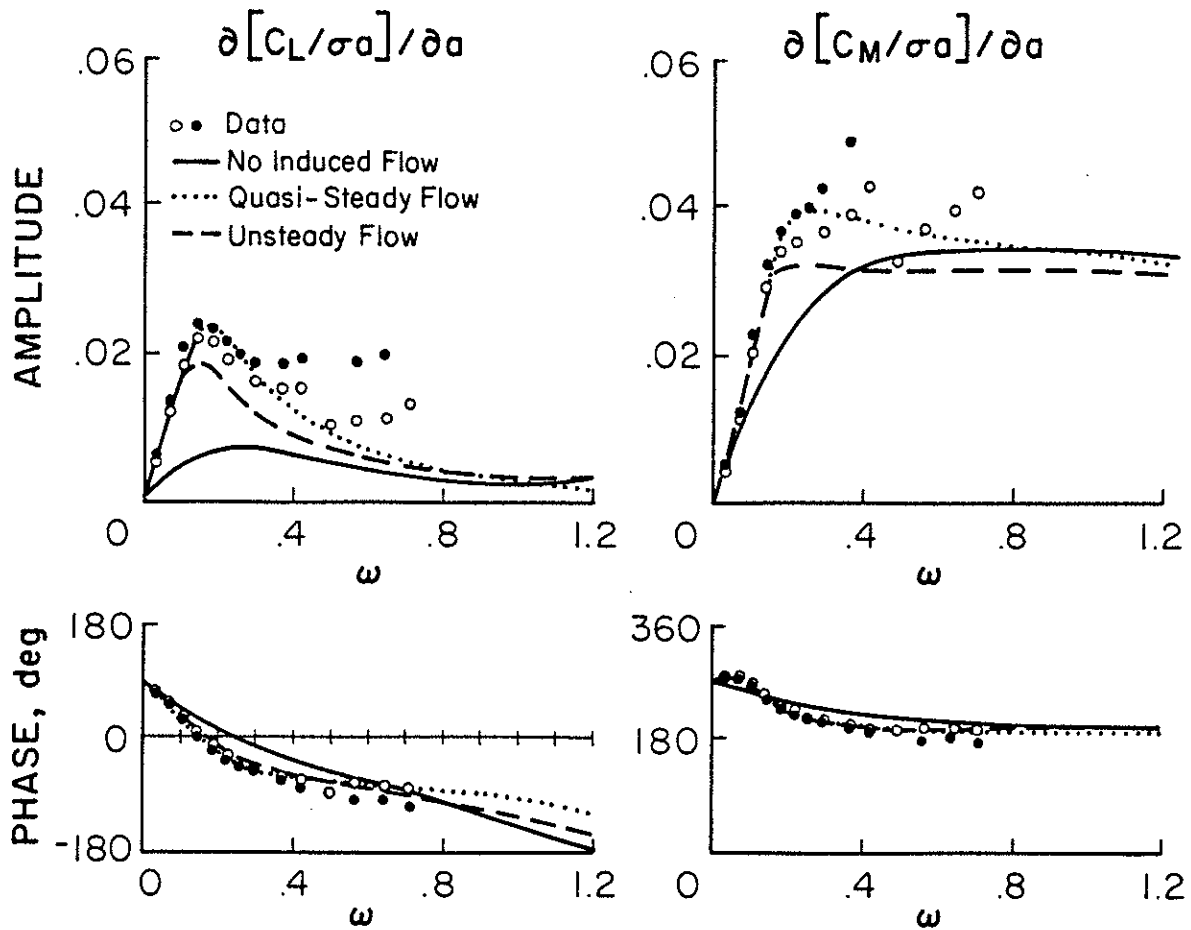
Figure 8. Rotor Response to Hub Motions in Hover, p=1.15, Y' =4.25, B=.97,
e_{pc} =.25, μ =0, σa=.7294, $\bar{\nu}$ =$\bar{\lambda}$ =.03, Θ_o =4°, momentum theory,
single rotating mode.

Figure 9. Rotor Response to Cyclic Pitch in Forward Flight, p=1.15, V=4.25, B=.97, e_{pc}=.25, μ=.51, σa=.7294, $\bar{\nu}=\bar{\lambda}=0$, Θ_o=1/2", single rotating mode.
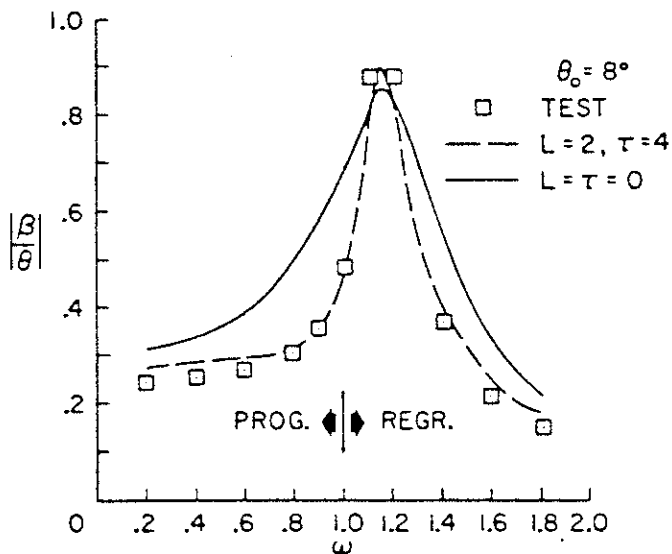
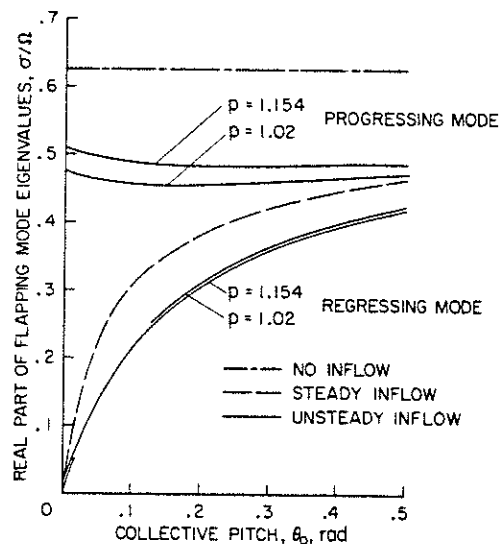Figure 10. Rotor Response to Pitch Stirring, p=1.21, V=4.0, μ=0, B=.97.

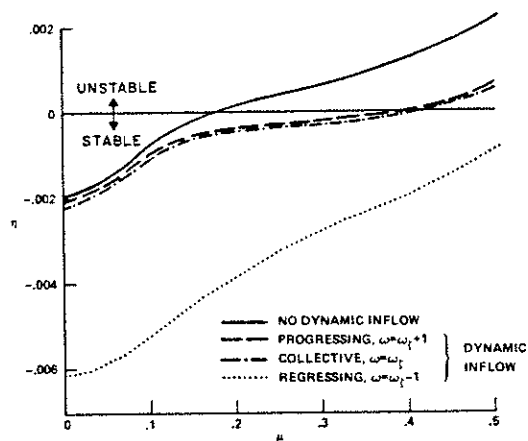Figure 11. The Effect of Different Induced Flow Models on Flap Mode Damping, V=10, σ=.15.

Figure 12. Effect of Dynamic Inflow on Lead-
Lag Mode, $\tilde{\omega}_\zeta = 1.4$, p=1.15, γ =5,
C_T=0.1, σ =.05, C_{d_o}=.01.

Figure 15.

Body Roll Mode Damping as a Function of Rotor Speed,
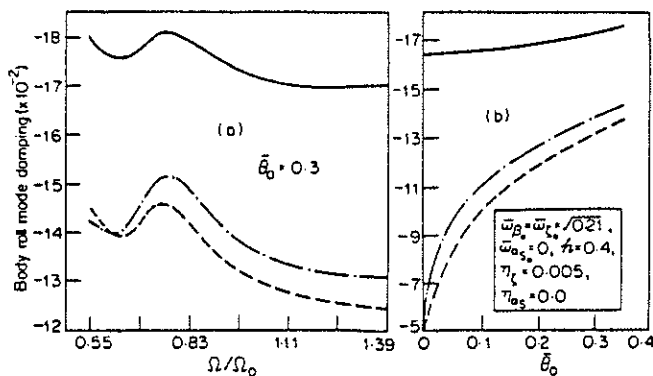σ =.05, γ =8.4, Hover.

Figure 13.

Body Role Mode Damping of a Matched-Stiffness Rotor with:
No Dynamic Inflow (—), Quasi-steady Inflow (—·—), and
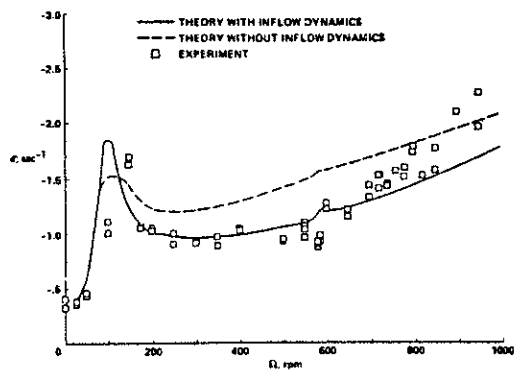Unsteady Inflow (---); μ =.1, γ =5, σ =.05, p=1.1.

Figure 16.

Modal Frequencies as a Function of Rotor Speed: Comparison,
Theory (—) and Data (o , ◊ , □), σ =.05, γ = 8.4, Hover.

Figure 14.

Body Pitch Mode Damping as a Function of Rotor Speed,
σ =.05, γ =8.4, Hover.

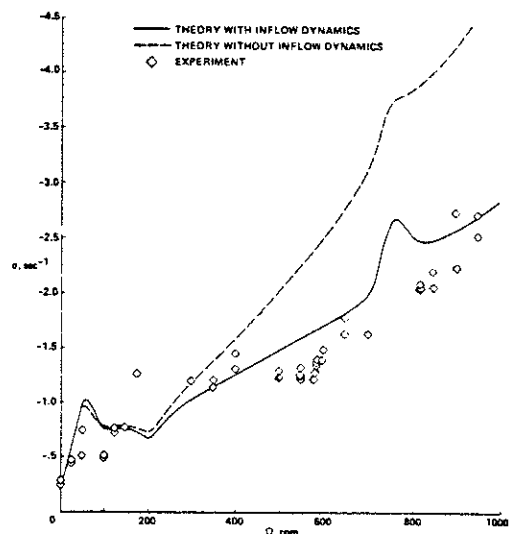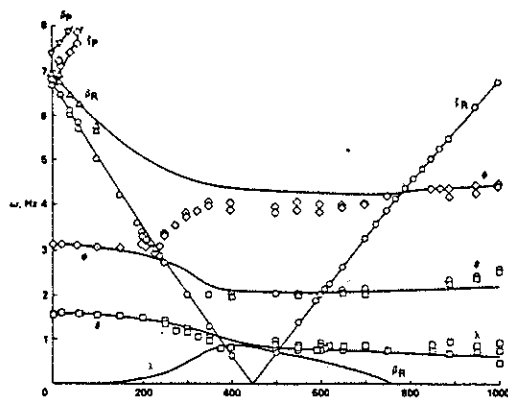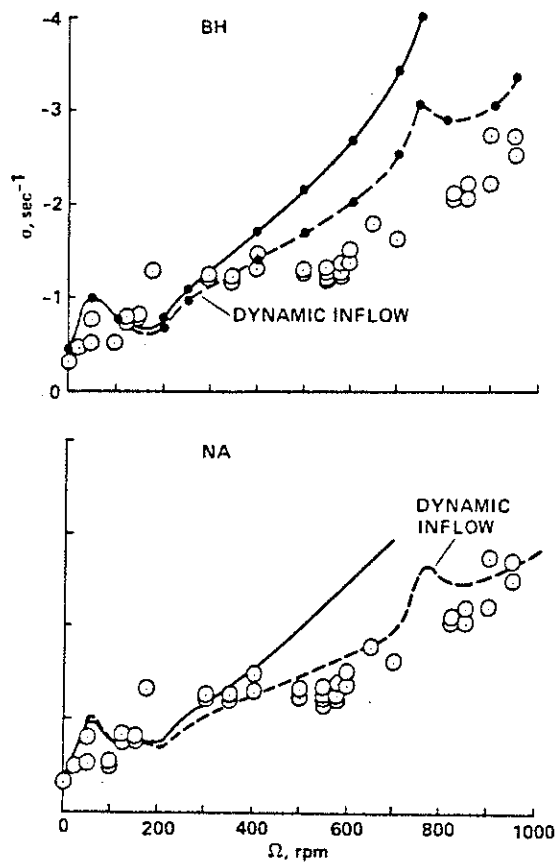Figure 17. Comparison of Roll Mode Damping, Bell and NASA Ames Models.
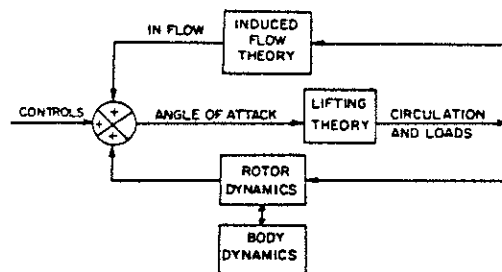

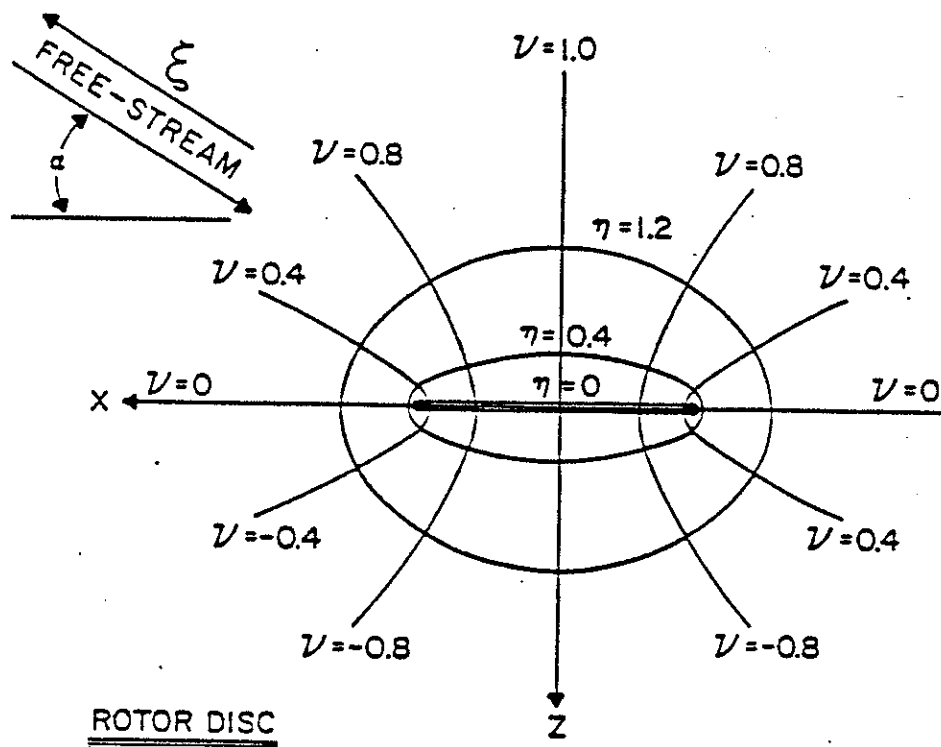Figure 18. Block Diagram of Inflow Dynamics.
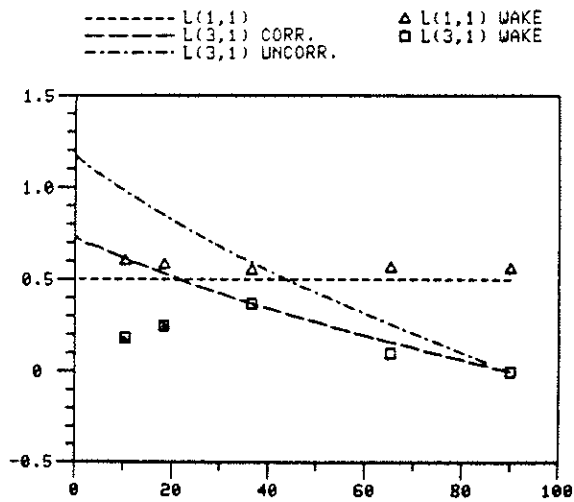
Figure 19.

Ellipsoidal Coordinates.

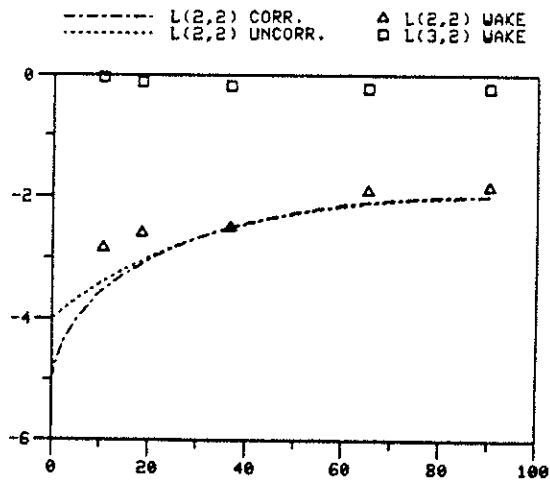Figure 20. Verification of First Column of L.

Figure 21. Verification of Second Column of L.
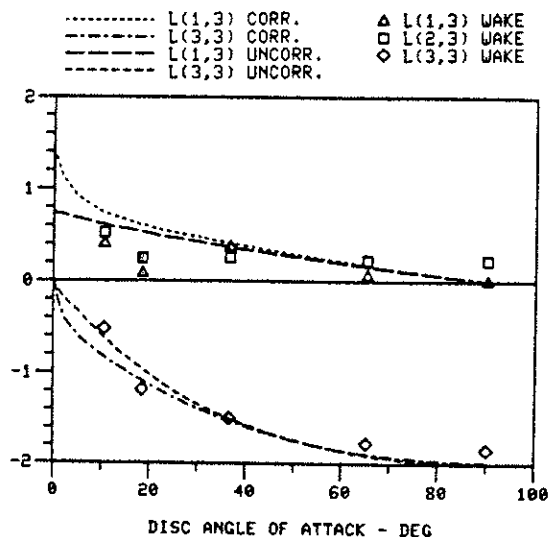
Figure 22. Verification of Third Column of L.
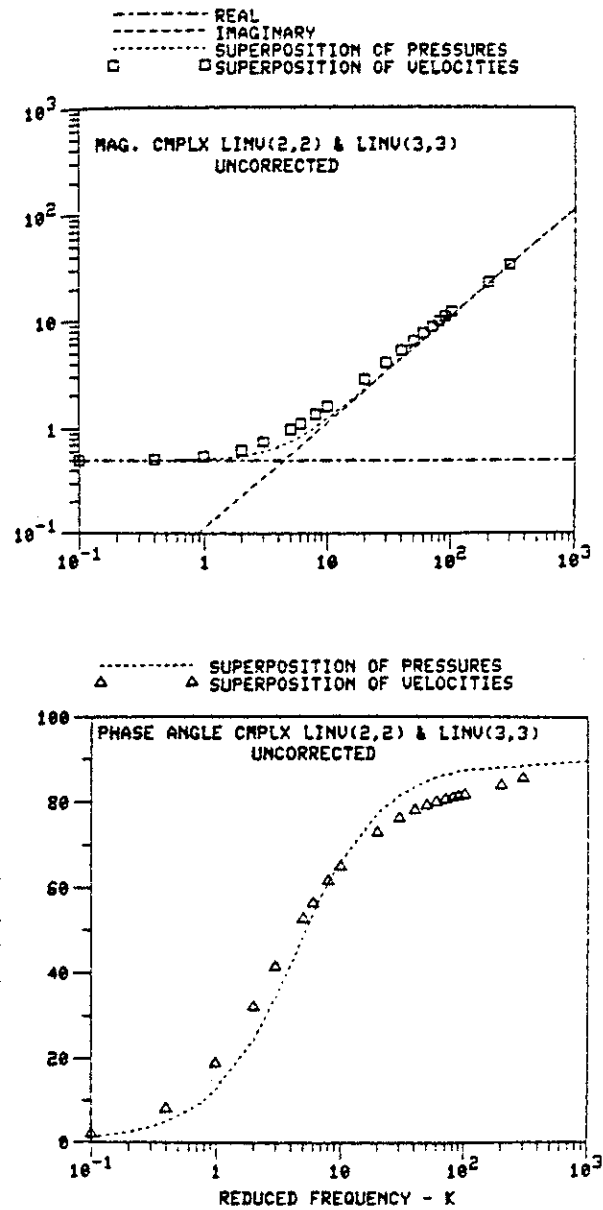
Figure 23.

Comparison of Unsteady Pressure Distribution with
Superposition of Apparent Mass Terms.

119

Table 1. Comparison of Mass Flow Parameters

Condition	$\upsilon^* + \bar\nu \sin\alpha^*$ Ref. 11	$\upsilon + \bar\nu \sin\alpha$ Ref. 8	$\upsilon^* + \lambda + \bar\nu$ Ref. 20, C_T	υ^* Ref. 20, C_L and C_M
Hover, $\mu = \lambda = 0$	$2\bar\nu$	$2\bar\nu$	$2\bar\nu$	$\bar\nu$
Zero lift, climb $\bar\nu = 0,\ \mu = 0$	λ	λ	2λ	λ
Climb, $\mu = 0$	$\lambda + 2\bar\nu$	$\lambda + 2\bar\nu$	$2\lambda + 2\bar\nu$	$\lambda + \bar\nu$
Zero lift, edgewise $\bar\nu = 0,\ \lambda = 0$	μ	μ	μ	μ
Lifting, edgewise $\lambda = 0$	$\dfrac{\mu^2 + 2\bar\nu^2}{\sqrt{\mu^2 + \bar\nu^2}}$	μ	$\sqrt{\mu^2 + \bar\nu^2} + \bar\nu$	$\sqrt{\mu^2 + \bar\nu^2}$
Zero lift $\bar\nu = 0$	$\sqrt{\mu^2 + \lambda^2}$	$\sqrt{\mu^2 + \lambda^2}$	$\sqrt{\mu^2 + \lambda^2} + \lambda$	$\sqrt{\mu^2 + \lambda^2}$
No normal flow, $\lambda = -\bar\nu$ (descent)	μ	$\dfrac{\mu^2 - \lambda^2}{\sqrt{\mu^2 + \lambda^2}}$	μ	μ

120

$$[L] = \frac{1}{v}\begin{bmatrix} \dfrac{1}{2} & 0 & \dfrac{15\pi}{64}\sqrt{\dfrac{1-\sin\alpha}{1+\sin\alpha}} \\[2ex] 0 & \dfrac{-4}{1+\sin\alpha} & 0 \\[2ex] \dfrac{15\pi}{64}\sqrt{\dfrac{1-\sin\alpha}{1+\sin\alpha}} & 0 & \dfrac{-4\sin\alpha}{1+\sin\alpha} \end{bmatrix}$$

$$[M] = \begin{bmatrix} \dfrac{128}{75\pi} & 0 & 0 \\[2ex] 0 & \dfrac{-16}{45\pi} & 0 \\[2ex] 0 & 0 & \dfrac{-16}{45\pi} \end{bmatrix}$$

Table 2.   Analytic Forms of L-matrix and M-matrix

$$[L] = [\alpha]\begin{bmatrix} 1/V_T & 0 & 0 \\ 0 & 1/V & 0 \\ 0 & 0 & 1/V \end{bmatrix}$$

$$V_T = \sqrt{(\lambda+\upsilon_0)^2+\mu^2} \qquad V = \frac{d}{d\upsilon_0}(\upsilon_0 V_T)$$

$$V = \left[(\lambda+\upsilon_0)(\lambda+2\upsilon_0)+\mu^2\right]/V_T$$

Table 3.   Nonlinear Version of Dynamic Inflow Theory

TECHNICAL NOTES

Technical Notes is intended to provide a forum for prompt disclosure of new developments or important results of a preliminary nature. Short manuscripts not exceeding one-quarter the length of a full paper may qualify for publication in this category. Submissions will be informally reviewed by the Editor and published within a few months of receipt.

The Effects of Second Order Blade Bending on the Angle of Attack of Hingeless Rotor Blades

David A. Peters and Robert A. Ormiston

Ames Directorate, U.S. Army Air Mobility R&D Laboratory, Moffett Field, California

The aeroelastic stability of hingeless rotor blades is known to be highly sensitive to small variations in many configuration parameters.[1-3] In particular, pitch-lag and pitch-flap coupling, whether induced by control system geometry or by elastic coupling between blade torsion and blade bending, greatly influence the stability of rotor blade motion. In this note, an expression for the angle of attack of an elastic rotor blade is derived which includes important second order terms due to blade bending. These terms are interpreted as a dihedral effect and a kinematic pitch rotation which is independent of torsional deformations. The kinematic rotation has not heretofore been included in stability analyses of elastic hingeless rotor blades. These angle of attack terms can be expressed as effective pitch-lag and pitch-flap coupling and are shown to be significant for rotor blade stability calculations.

NOTATION

$C, \tilde{C}$ = pitch coupling parameters
$[T]$ = tensor transformation
$\mathbf{i, j, k}$ = unit vectors of blade-fixed coordinate system
$\mathbf{I, J, K}$ = unit vectors of rotating coordinate system
α = angle-of-attack
ϕ = elastic torsional deformations
ζ, β, θ = Euler angles of blade-fixed coordinate system
ϕ_i, ψ_i = mode shapes
ω = radial rate of rotation of blade-fixed coordinate system
$\omega_i, \omega_j, \omega_k$ = curvatures, components of ω
$(\ )'$ = d/dr
$(\dot{\ })$ = $d/d\psi = d/d(\Omega t)$
u, v, w = axial, lead-lag, and flapping displacements of rotor blade
μ, λ = advance and inflow ratios
s, c = sine, cosine
R = blade radius

TENSOR FORMULATION

To formulate the blade angle of attack relations, it is convenient to use the displacement and coordinate system definitions shown in Fig. 1. The displacements of a point on the blade are defined as u, v, w which are written as functions of the running length along the blade, r. Two separate coordinate systems are defined, the I, J, K system which is fixed to the rotating reference frame and the i, j, k system which is fixed to the blade. The tensor transformation between the two systems is given by

$$\begin{Bmatrix} \mathbf{i} \\ \mathbf{j} \\ \mathbf{k} \end{Bmatrix} = [T] \begin{Bmatrix} \mathbf{I} \\ \mathbf{J} \\ \mathbf{K} \end{Bmatrix}, \quad \begin{Bmatrix} \mathbf{I} \\ \mathbf{J} \\ \mathbf{K} \end{Bmatrix} = [T]^T \begin{Bmatrix} \mathbf{i} \\ \mathbf{j} \\ \mathbf{k} \end{Bmatrix} \quad (\ )$$
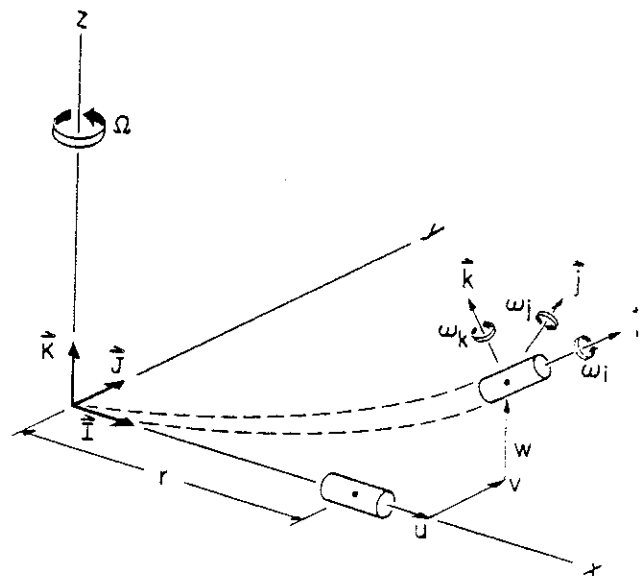
Figure 1. Blade coordinate systems.

Figure 2. Euler angles.

components of the rate of rotation ω can be identified as the torsional rotation rate ($\omega_i = \phi'$) and the bending curvature (ω_j and ω_k) as shown in Fig. 1. This infinitesimal rotation can be written in terms of the rotation tensor giving a differential equation for $[T]$.

$$[T]' = \begin{bmatrix} 0 & \omega_k & -\omega_j \\ -\omega_k & 0 & \omega_i \\ \omega_j & -\omega_i & 0 \end{bmatrix} [T], \begin{bmatrix} 0 & \omega_k & -\omega_j \\ -\omega_k & 0 & \omega_i \\ \omega_j & -\omega_i & 0 \end{bmatrix} = [T]'[T]^T \quad (4)$$

Substitution of Eq. (3) into Eq. (4) (and eliminating $\omega_i, \omega_j,$ and ω_k yields the following exact expression for θ (the Euler pitch angle) completing the solution for $[T]$.

$$\theta = \theta_0 + \phi - \int_0^r \frac{v''w'}{\sqrt{1 - v'^2 - w'^2}} dr - \int_0^r \frac{w'^2 w'' v'}{(1 - w'^2)\sqrt{1 - v'^2 - w'^2}} dr \quad (5)$$

Note that $\theta \equiv \theta_0$ at the blade root. This equation is significant because it shows that the blade pitch angle is due to neither elastic torsional deformations ϕ nor root pitch angle alone. Second order contributors to the pitch angle also occur from purely bending deformations. The elastic torsional deformations ϕ resulting from combined flap and lead-lag bending of hingeless rotor blades are dependent on the difference between the flap and lead-lag bending stiffness of the blade. For "matched stiffness" configurations, these elastic torsional deformations will vanish, but the present results show that a kinematic pitching of the blade will still result from the bending deformations.
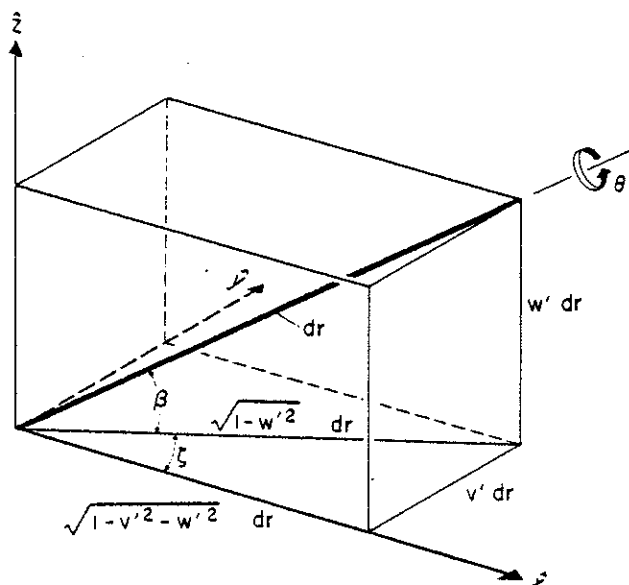
where $[T]$ can be expressed in terms of Euler angles as

$$[T] = \begin{bmatrix} c\beta c\zeta & c\beta s\zeta & s\beta \\ -s\theta s\beta c\zeta & c\theta c\zeta & \\ -c\theta s\zeta & -s\zeta s\beta s\theta & c\beta s\theta \\ -c\theta s\beta c\zeta & -s\theta c\zeta & \\ +s\theta s\zeta & -s\zeta s\beta c\theta & c\beta c\theta \end{bmatrix} \quad (2)$$

The Euler angles are defined in Fig. 2 and are taken in the order ζ, β, θ. They uniquely define the orientation of the blade principle axes with respect to the undeformed coordinate system.

Because rotor blade equations are written in terms of the blade displacements and the blade torsional deformation (v, w, ϕ), it is necessary to express $[T]$ in terms of v, w, ϕ rather than ζ, β, θ. The Euler angles ζ and β can be easily expressed in terms of v and w (Fig. 2) yielding

BLADE ANGLE OF ATTACK

The lift generated by a blade (and consequently the effective angle of attack) is readily expressed

$$[T] = \begin{bmatrix} \sqrt{1 - v'^2 - w'^2} & v' & w' \\ [-s\theta w'\sqrt{1 - v'^2 - w'^2} & [c\theta\sqrt{1 - v'^2 - w'^2} & \\ - c\theta v']/\sqrt{1 - w'^2} & - s\theta v'w']\sqrt{1 - w'^2} & s\theta\sqrt{1 - w'^2} \\ [-c\theta w'\sqrt{1 - v'^2 - w'^2} & [-s\theta\sqrt{1 - v'^2 - w'^2} & \\ + s\theta v']/\sqrt{1 - w'^2} & - c\theta v'w']/\sqrt{1 - w'^2} & c\theta\sqrt{1 - w'^2} \end{bmatrix} \quad (3)$$

The determination of the third Euler angle θ, however, requires the solution of a differential equation for $[T]$. Consider the small rotation, $\omega\, dr$, of the blade-fixed coordinate system which occurs as r goes through the increment dr. The vector

in terms of the air velocity components in the blade-fixed coordinate system as shown in Fig. 3. These components are directly related to the
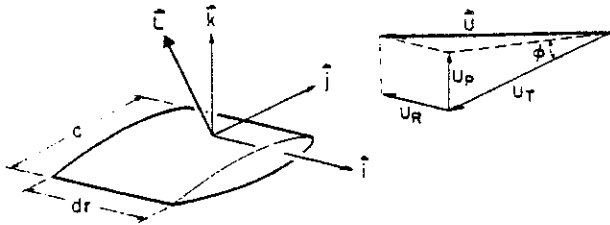
$$|\hat{L}| = \frac{\rho a c}{2}\, dr\, (U_P{}^2 + U_T{}^2)\,(\sin\phi)$$

$$L_i = 0, \quad L_j = |\hat{L}|\sin\phi, \quad L_k = |\hat{L}|\cos\phi$$

$$L_k = \frac{\rho a c}{2}\, dr\, (U_P\, U_T), \quad L_j = \frac{\rho a c}{2}\, dr\, U_P{}^2$$

Figure 3. Blade element aerodynamics.

tensor transform $[T]$ by

$$
\begin{Bmatrix} U_R \\ U_T \\ -U_P \end{Bmatrix}
= [T]
\begin{Bmatrix} -\mu R c\psi - v + \dot{u} \\ \mu R s\psi + r + u + \dot{v} \\ \lambda R + \dot{w} \end{Bmatrix}
\Omega
\tag{6}
$$

The major effect of $[T]$ on the angle of attack can be found by working out L_k (as defined in Fig. 3) for the hover condition, keeping only terms of second order or less in v, w, and ϕ. Using Eq. (6), the resultant lift and angle of attack expressions are

$$L_k = \frac{\rho a c}{2} dr (U_P U_T) = \frac{\rho a c}{2} dr (\Omega^2 r^2)\alpha \tag{7}$$

where

$$\alpha \equiv \theta_0 + \phi - \left(\frac{\lambda R}{r} + \frac{\dot{w}}{r} + \frac{\dot{v}\lambda R}{r^2}\right) - \frac{v}{r}w'$$
$$- 2\,\frac{v\dot{v}}{r^2} + v'w' - \int_0^r v''w'\,dr \tag{8}$$

The first term in the angle of attack expression is the Euler angle at the blade root. The second term is the elastic blade rotation due to torsional moments about i (including those due to "bending" moments about J and K). The next three terms express the angle of attack due to inflow and blade motions. The next two terms are analogous to the dihedral effect of a fixed wing, and are caused by the blade unit vector i not being in line with the center of rotation. They are affected by blade precone, torque offset, and the blade elastic displacements. The last term is the second order kinematic pitch rotation of the blade from Eq. (5), and also affected by blade precone.

These terms are usually treated properly for rotor blade analyses which use a hinged blade approximation because the angular rotations are uniquely defined by the blade hinge geometry.

However, equations for the elastic rotor blade are not as easily derived; and the above terms are usually not properly accounted for. For instance, the dihedral terms are not completely included in Refs. 2–4 and none of these references includes the kinematic pitch term, although it is of comparable magnitude to the dihedral terms.

EFFECTIVE PITCH COUPLING

For a linearized perturbation analysis the second order angle of attack terms assume the character of pitch-lag and pitch-flap coupling coefficients. Using a modal representation of the blade

$$v = \sum_{i=0}^{n} \psi_i(r)\zeta_i, \qquad w = \sum_{j=0}^{n} \phi_j(r)\beta_j \tag{9}$$

where $\psi_0\zeta_0$ and $\phi_0\beta_0$ represent the equilibrium position of the blade, the blade angle of attack of Eq. (8) becomes (for $\lambda = 0$, steady-state)

$$\alpha = \theta_0 + \phi + C_{00}(r)\beta_0\zeta_0 + \sum_{i=1}^{n} C_{i0}(r)\beta_0\zeta_i$$
$$+ \sum_{j=1}^{n} C_{0j}(r)\zeta_0\beta_j \tag{10}$$

where

$$C_{ij}(r) \equiv \frac{-\psi_i}{r}\phi_j' + \psi_i'\phi_j' - \int_0^r \psi_i''\phi_j'\,dr \tag{11}$$

In modal representations it is often useful to also define an average angle of attack

$$\bar{\alpha} \equiv \theta_0 + \bar{\phi} + \bar{C}_{00}\beta_0\zeta_0 + \sum_{i=1}^{n}\bar{C}_{i0}\beta_0\zeta_i + \sum_{j=1}^{n}\bar{C}_{0j}\zeta_0\beta_j \tag{12}$$

where

$$\langle \bar{\alpha}, \bar{\phi}, \bar{C}_{ij}\rangle = \frac{\int_0^R r^2\phi_1(r)\langle\alpha(r),\phi(r),C_{ij}(r)\rangle\,dr}{\int_0^R r^2\phi_1(r)\,dr} \tag{13}$$

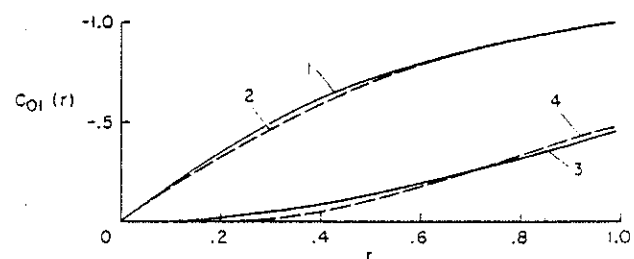|	1	2	3	4
EQUILIBRIUM FLAP MODE, ϕ_0	$\phi_0 = r$ (PRE-CONE)	$\phi_0 = r$ (PRE-CONE)	NONROTATING	ROTATING
PERTURBATION LEAD-LAG MODE, ψ_1	NONROTATING	ROTATING	NONROTATING	ROTATING

Figure 4. Pitch coupling parameters.

12Aa

Thus an equilibrium value of lead-lag displacement gives pitch flap coupling coefficients $\bar{C}_0, \zeta_0$, and an equilibrium value of flap displacement gives pitch-lag coupling coefficients $\bar{C}_{i0}\beta_0$.

Some examples of the magnitude of C_{ij} are given in Fig. 4. The coupling due to blade pre-cone and the coupling due to equilibrium elastic blade deflection are calculated using two different mode shapes: a) a rotating mode, and b) a nonrotating mode. (Both modes are normalized to unit tip deflection). A comparison of the curves shows that the amount of coupling is not strongly dependent upon the details of the mode shape. The average value of the coupling parameter $(\bar{C}_{01})$ is 0.92 for precone and 0.36 for static deflections when either mode shape is used.

The significance of coupling of this magnitude can be partially inferred from Fig. 5 where the effect of the second order coupling is presented for a hinged blade with hinge sequence flap-lag, $\bar{C} = -1$. For a lag-flap sequence, $\bar{C} = 0$. For this matched stiffness configuration, the coupling term reduces the stability boundary by more than one-half. Although $\bar{C}$ may not be this powerful for all rotor configurations, $\bar{C}$ values of 40% to 90% of the flap-lag value cannot reasonably be neglected.

CONCLUSIONS

A rigorous formulation of rotor blade deformations yields the higher order terms in the blade angle of attack relations. A careful examination of these terms indicates that there are significant amounts of pitch-lag and pitch-flap coupling which can be introduced by pre-cone or blade deforma-
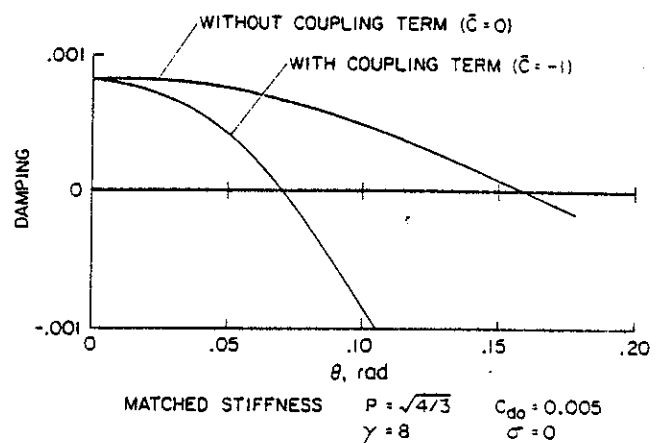
Figure 5. Effect of second order terms.

tions. Because of the delicate stability balance present in the flap-lag dynamics, this second order coupling is not negligible and can cause significant changes in stability.

REFERENCES

1. Hohenemser, K. H. and Heaton, P. W. Jr., "Aero-elastic Instability of Torsionally Rigid Helicopter Blades." J. American Helicopter Society, 12(2), April 1967.
2. Ormiston, R. A. and Hodges, D. H., "Linear Flap-Lag Dynamics of Hingeless Rotor Blades in Hover," J. American Helicopter Society 17(2), April 1972.
3. Friedmann, P. and Tong, P., "Dynamic Nonlinear Elastic Stability of Helicopter Rotor Blades in Forward Flight," NASA CR-114485, 1972.
4. Hodges, D. H. and Ormiston, R. A., "Nonlinear Equations for Bending of Rotating Beams with Application to Linear Flap-Lag Stability of Hingeless Rotors," NASA TMX-2770 Nov 1972.

NASA TECHNICAL MEMORANDUM

AN APPROXIMATE CLOSED-FORM SOLUTION FOR LEAD-LAG DAMPING OF ROTOR BLADES IN HOVER

David A. Peters

Ames Research Center

and

U. S. Army Air Mobility R&D Laboratory
Moffett Field, Calif. 94035

April 1975

1. Report No.	2. Government Accession No.	3. Recipient's Catalog No.
TM X-62,425		
4. Title and Subtitle		5. Report Date
AN APPROXIMATE CLOSED-FORM SOLUTION FOR LEAD-LAG DAMPING OF ROTOR BLADES IN HOVER		
		6. Performing Organization Code
7. Author(s)		8. Performing Organization Report No.
David A. Peters		A-6025
		10. Work Unit No.
9. Performing Organization Name and Address		
Ames Research Center and U.S. Army Air Mobility R&D Laboratory Moffett Field, Calif., 94035		11. Contract or Grant No.
		13. Type of Report and Period Covered
		Technical Memorandum
12. Sponsoring Agency Name and Address		
National Aeronautics and Space Administration Washington, D. C. 20546		14. Sponsoring Agency Code

15. Supplementary Notes

16. Abstract

Simple stability methods are used to derive an approximate, closed-form expression for the lead-lag damping of rotor blades in hover. Destabilizing terms are shown to be a result of two dynamic mechanisms. First, the destabilizing aerodynamic forces that can occur when blade lift is higher than a critical value are maximized when the blade motion is in a straight line equidistant from the blade chord and the average direction of the air flow velocity. This condition occurs when the Coriolis terms vanish and when the elastic coupling terms align the blade motion with this least stable direction. Second, the nonconservative stiffness terms that result from pitch-flap or pitch-lag coupling can add or subtract energy from the system depending upon whether the motion of the blade tip is clockwise or counterclockwise.

17. Key Words (Suggested by Author(s))		18. Distribution Statement	
Helicopter Rotor blade		Unclassified - Unlimited STAR Category 02	
19. Security Classif. (of this report)	20. Security Classif. (of this page)	21. No. of Pages	22. Price*
Unclassified	Unclassified	27	$3.75

AN APPROXIMATE CLOSED-FORM SOLUTION FOR LEAD-LAG

DAMPING OF ROTOR BLADES IN HOVER

David A. Peters

U. S. Army Air Mobility R&D Laboratory
and
Ames Research Center

SUMMARY

Simple stability methods are used to derive an approximate, closed-form expression for the lead-lag damping of rotor blades in hover. Destabilizing terms are shown to be a result of two dynamic mechanisms. First, the destabilizing aerodynamic forces that can occur when blade lift is higher than a critical value are maximized when the blade motion is in a straight line equidistant from the blade chord and the average direction of the air flow velocity. This condition occurs when the Coriolis terms vanish and when the elastic coupling terms align the blade motion with this least stable direction. Second, the nonconservative stiffness terms that result from pitch-flap or pitch-lag coupling can add or subtract energy from the system depending upon whether the motion of the blade tip is clockwise or counterclockwise.

INTRODUCTION

Flap-lag stability is an important fundamental basis for the study of hingeless rotorcraft dynamics. Although a simple flap-lag analysis is not adequate for the absolute determination of blade stability, it is invaluable for giving insight into the basic physical mechanisms that underly the more complex dynamic phenomena. Reference 1 described the flap-lag dynamics of a hingeless rotor in hover by using the simplified model of a rigid blade with root spring restraint. Numerical results provided a systematic study of the effect of blade parameters on rotor stability, and applications of Routh's criteria identified stability boundaries for some specialized conditions. The present paper studies this same problem using different methods that provide additional explanations of the system behavior. These methods permit the development of an approximate, closed-form expression for the lead-lag damping. In addition, the methods illustrate the specific contributions of various dynamic mechanisms to the blade damping.

A-6025

a   lift curve slope per radian

C_{d_o} profile drag coefficient

$[C]$ matrix coefficients of $\dot{\beta}, \dot{\zeta}$ terms

$[D]$ damping matrix, $\frac{1}{2} [C + C^T]$

F_1, F_2 dimensionless elastic forces

$[G]$ Coriolis matrix, $\frac{1}{2} [C - C^T]$

i $\sqrt{-1}$

$[K]$ stiffness matrix

p   rotating flapping frequency divided by Ω

$\bar{p}$ equivalent flapping frequency, $\sqrt{p^2 - \frac{\gamma}{8} \theta_\beta}$

R   elastic coupling parameter

s   Laplace transform variable, rad^{-1}

x_1, x_2 flap and lead-lag directions

β perturbation flapping angle, positive up, rad

β_o equilibrium flapping angle, rad

β_{pc} precone angle, rad

γ Lock number

δ angle between lead-lag direction and the principal axis of blade motion, rad

δ_m angle between lead-lag direction and the direction of the natural vibrations of the rotating blade in a vacuum, $\dfrac{\Delta}{\omega_\zeta^2 - p^2}$, rad

$\bar{\delta}_m$ modified δ_m including pitch-flap and pitch-lag coupling, $\dfrac{\Delta - \frac{\gamma}{8} \theta_\zeta}{\omega_\zeta^2 - \bar{p}^2}$

$\delta\theta$ perturbation pitch angle, $\theta_\beta \beta + \theta_\zeta \zeta$, rad

Δ elastic coupling term

A-6025

2

128

Δ_θ partial derivative of Δ, $\frac{\partial\Delta}{\partial\theta}$

ϵ perturbation of lead-lag eigenvalue, rad^{-1}

ζ perturbation lead-lag angle, positive forward, rad

ζ_0 equilibrium lead-lag angle, rad

η real portion of ϵ, rad^{-1}

θ equilibrium pitch angle, $\theta_0 + \theta_\beta(\beta_0 - \beta_{pc})$, rad

θ_0 collective pitch, rad

$\theta_\beta, \theta_\zeta$ pitch-flap and pitch-lag coupling

$\bar{\theta}_\beta$ coupling due to θ_β, $\left[\phi + \frac{8}{\gamma}(\beta_0 - \beta_{pc})\Delta_\theta\right]\theta_\beta$

λ eigenvalue of $[D]$

$\begin{Bmatrix}\lambda_\beta \\ \lambda_\zeta\end{Bmatrix}$ eigenvector of $[D]$

ρ thickness ratio of ellipse of motion (positve for clockwise motion)

ϕ average inflow angle (A of ref. 1), rad

ϕ_β flapping component of lead-lag mode shape when lead-lag component = 1, $\phi_\beta = \delta + i\rho$

ω_ζ lead-lag frequency divided by Ω

Ω rotor rotational speed, rad^{-1}

$(\dot{\ })$ $\frac{d}{d(\Omega t)}$

$(\ )^*$ complex conjugate

3

The linearized flap-lag equations of motion, as derived in reference 1, may be written in the form

$$\left\{ \begin{array}{c} \ddot{\beta} \\ \ddot{\zeta} \end{array} \right\} + \begin{bmatrix} C_{11} & C_{12} \\ C_{21} & C_{22} \end{bmatrix} \left\{ \begin{array}{c} \dot{\beta} \\ \dot{\zeta} \end{array} \right\} + \begin{bmatrix} K_{11} & K_{12} \\ K_{21} & K_{22} \end{bmatrix} \left\{ \begin{array}{c} \beta \\ \zeta \end{array} \right\} = \left\{ \begin{array}{c} 0 \\ 0 \end{array} \right\} \tag{1}$$

where

$$C_{11} = \frac{\gamma}{8}$$

$$C_{12} = 2\beta_o - \frac{\gamma}{8}(2\theta - \phi)$$

$$C_{21} = -2\beta_o + \frac{\gamma}{8}(\theta - 2\phi)$$

$$C_{22} = \frac{\gamma}{8}\left(2\frac{C_{d_o}}{a} + \theta\phi\right)$$

$$K_{11} = p^2 - \frac{\gamma}{8}\theta_\beta \equiv \bar{p}^2$$

$$K_{12} = \Delta - \frac{\gamma}{8}\theta_\zeta$$

$$K_{21} = \Delta + \left[\frac{\gamma}{8}\phi + (\beta_o - \beta_{pc})\Delta_\theta\right]\theta_\beta \equiv \Delta + \frac{\gamma}{8}\bar{\theta}_\beta$$

$$K_{22} = \omega_\zeta^2$$

and β_o, $\sqrt{\bar{\zeta}_o}$, θ, ϕ, θ_ζ, $\bar{\theta}_\beta$, $\sqrt{C_{d_o}/a}$ are considered small quantities whose products may be neglected with respect to unity. Equation (1) also contains a contribution from the homogeneous terms of reference 1, $(\beta_o - \beta_{pc})\Delta_\theta\theta_\beta$ in K_{21}, that results from the effect of pitch-flap coupling on the steady elastic pitch angle.

From reference 1, it is known that the least stable mode of motion is predominantly lead-lag. It is also known that the frequency of the motion is near ω_ζ and that the damping is very small. This allows a perturbation solution for equation (1) to be derived. The perturbation solution is obtained by applying the following perturbation expressions to the Laplace transformed equation (1).

4

130

$$s = i\sqrt{K_{22}} + \epsilon$$

$$\begin{Bmatrix} \beta \\ \zeta \end{Bmatrix} = \begin{Bmatrix} \phi_\beta \\ 1 \end{Bmatrix} e^{st} \qquad (2)$$

where ϵ and ϕ_β are considered small quantities.

$$\begin{bmatrix} K_{11} - K_{22} & K_{12} \\ +iC_{11}\sqrt{K_{22}} & +iC_{12}\sqrt{K_{22}} \\ \hline K_{21} & iC_{22}\sqrt{K_{22}} \\ +iC_{21}\sqrt{K_{22}} & +2i\epsilon\sqrt{K_{22}} \end{bmatrix} \begin{Bmatrix} \phi_\beta \\ 1 \end{Bmatrix} = \begin{Bmatrix} 0 \\ 0 \end{Bmatrix} \qquad (3)$$

The solution of equation (3) is simply

$$\epsilon = -\frac{C_{22}}{2} + \frac{[K_{12} + iC_{12}\sqrt{K_{22}}][K_{21}i - C_{21}\sqrt{K_{22}}]}{2\sqrt{K_{22}}(K_{22} - K_{11} - iC_{11}\sqrt{K_{22}})} \qquad (4a)$$

$$\phi_\beta = \frac{K_{12} + iC_{12}\sqrt{K_{22}}}{(K_{22} - K_{11}) - iC_{11}\sqrt{K_{22}}} \qquad (4b)$$

Equations (4a) and (4b) give the change in frequency $Im(\epsilon)$, damping $Re(\epsilon)$, and mode shape θ_β due to the presence of flap-lag coupling. They imply that transient motion of the blade tip is a slowly decaying or growing ellipse. Although equation (4a) can be directly applied to obtain an approximate expression for lead-lag damping, the identical result can be obtained by applying simple stability methods to equation (1). This latter method has the advantage of describing the specific contributions of various dynamic mechanisms to the blade damping and will be used in this paper.

NEGATIVE AERODYNAMIC DAMPING

The first stability method to be considered is based on the Kelvin-Tait-Chetaev theorem, reference 2. This theorem applies to equation (1) when no pitch-flap or pitch-lag coupling is present ($\theta_\beta = \theta_\zeta = 0$) and when the matrix [C] is decomposed into symmetric and antisymmetric parts.

$$[D] \equiv \frac{1}{2}[C + C^T] \quad \text{damping matrix}$$

5

131

$$[G] \equiv \frac{1}{2} [C - C^T] \quad \text{Coriolis matrix}$$

The theorem states that if [D] has all positive eigenvalues, then the system is stable if, and only if, [K] has all positive eigenvalues. Stated another way, the theorem implies that if [K] has all positive eigenvalues, then a necessary, but not sufficient, condition for instability is that [D] have a negative eigenvalue. Thus, for a hingeless rotor without pitch coupling, for which [K] is always positive definite, an instability can occur only if [D] has a negative eigenvalue. The Coriolis and stiffness terms are conservative and can provide no positive or negative damping of their own.

Therefore, the stability of equation (1) is determined by the eigenvalues of the damping matrix

$$[D] = \frac{\gamma}{8} \begin{bmatrix} 1 & -\dfrac{\theta + \phi}{2} \\ -\dfrac{\theta + \phi}{2} & \theta\phi + 2\dfrac{C_{d_o}}{a} \end{bmatrix} \tag{5}$$

One can obtain approximate values for the eigenvalues of [D] by utilizing the fact that ϕ, θ, C_{d_o}/a are small quantities. The eigenvalue λ and eigenvector $\langle \lambda_\beta, \lambda_\zeta \rangle$ are given from

$$\begin{bmatrix} \dfrac{\gamma}{8} - \lambda & -\dfrac{\gamma}{16}(\theta + \phi) \\ -\dfrac{\gamma}{16}(\theta + \phi) & \dfrac{\gamma}{8}\left(\theta\phi + 2\dfrac{C_{d_o}}{a}\right) - \lambda \end{bmatrix} \begin{Bmatrix} \lambda_\beta \\ \lambda_\zeta \end{Bmatrix} = \begin{Bmatrix} 0 \\ 0 \end{Bmatrix}$$

and are

$$\lambda = \frac{\gamma}{8}, \quad \frac{\gamma}{8}\left[2\frac{C_{d_o}}{a} - \frac{(\theta - \phi)^2}{4}\right] \tag{6a}$$

$$\begin{Bmatrix} \lambda_\beta \\ \lambda_\zeta \end{Bmatrix} = \begin{Bmatrix} 1 \\ -\dfrac{\theta + \phi}{2} \end{Bmatrix}, \quad \begin{Bmatrix} \dfrac{\theta + \phi}{2} \\ 1 \end{Bmatrix} \tag{6b}$$

The term $\theta - \phi$ in the smaller lead-lag mode eigenvalue is the average blade angle of attack. Thus, the lead-lag damping decreases quadratically with the blade lift. Blade instabilities are only possible when the eigenvalue becomes negative and creates a source of negative damping. This can occur when the blade lift exceeds the critical value.

6

$$(\theta - \phi) > 2\sqrt{2\,\frac{C_{d_o}}{a}} \tag{7}$$

This relation was also derived in reference (1) by application of Routh's criteria.

The corresponding eigenvector of [D], equation (6b), shows that this minimum value of damping occurs along an axis which is equidistant from the blade chord line and the direction of the mean air flow velocity relative to the blade. Thus, there exists an axis of minimum damping that makes an angle $(\theta + \phi)/2$ with the lead-lag direction, as shown in figure 1. Blade motions nearly aligned with this axis will be unstable when equation (7) is fulfilled, but motions deviating from this axis will be stabilized by the large flap damping that exists in the direction perpendicular to the $(\theta + \phi)/2$ axis.

Another way of looking at this phenomenon is to consider the aerodynamic forces when blade motions make an angle δ with the lead-lag direction, figure 1. Blade motion in the positive lead-lag direction with $\delta = 0$ increases the blade lift, but the lift has a component in the negative lead-lag direction. Therefore, the increased lift opposes the motion and provides damping. For blade motions with $\phi < \delta < \theta$, the lift is similarly increased by positive velocities. In this case, however, the lift has a component in the positive direction of motion and therefore adds energy to the motion providing negative damping. When $\delta > \theta$, the lift is decreased by positive lead-lag velocity and the motion is stabilized. The aerodynamic energy added to the blade is maximum when $\delta = (\theta + \phi)/2$. The fact that the minimum damping occurs along the $(\theta + \phi)/2$ axis can also be derived by calculating the work done on the blade by the aerodynamic forces and showing that this energy is maximized when $\delta = (\theta + \phi)/2$. The relation between the direction of motion and the damping (or energy dissipation) is illustrated in figure 2 where the damping coefficient in the direction of blade motion is plotted versus δ. The minimum damping (i.e., the eigenvalue) occurs at the midpoint of the destabilizing region. Flap-lag instabilities in hover are a result of this negative aerodynamic damping.

In the previous discussion, the blade was assumed to move in a straight line. The blade may actually move, however, around an elliptical path as shown in figure 3. Thus, even when the principal axis of motion is along the $(\theta + \phi)/2$ axis, blade motions can be in the flap direction near the tips of the ellipse. This flap motion will stabilize the blade by introducing flap damping into the system. Since the uncoupled flap damping $\gamma/8$ is nearly an order of magnitude larger than the uncoupled lead-lag damping, $(\gamma/8)[(2C_{d_o}/a) + \theta\phi]$, flapping motion is highly stabilizing. For blade elliptical motion with thickness ratio ρ and tilted from the lead-lag plane by an angle δ, the flapping component of the mode shape is

$$\phi_\beta = \delta + i\rho \tag{8}$$

where δ and ρ are assumed small. The generalized damping of this mode is determined in the same manner as is the generalized mass or stiffness: the damping matrix is pre- and post-multiplied by the mode shape.

7

133

$$-2\eta = <\phi_\beta \quad 1>[D]\begin{Bmatrix} \phi_\beta \\ 1 \end{Bmatrix}^* \tag{9a}$$

$$\eta = \frac{\gamma}{16}\left[-2\frac{C_{d_0}}{a} + \frac{(\theta - \phi)^2}{4}\right] - \frac{\gamma}{16}\left[\left(\delta - \frac{\theta + \phi}{2}\right)^2 + \rho^2\right] \tag{9b}$$

The parameter η is the real portion of the eigenvalue. The first bracketed term in equation (9b) is the negative damping from the portion of the motion parallel to the $(\theta + \phi)/2$ axis. The second term is the positive flap damping obtained from the portion of the motion perpendicular to the $(\theta + \phi)/2$ axis. Equation (9b) gives the quantitative effect of mode shape on lead-lag damping. Motions along the $(\theta + \phi)/2$ axis are least stable, and deviations from this axis (either in angle or ellipse thickness ratio) stabilize the motion by utilizing the large flap damping.

ELASTIC COUPLING

The previous discussion implies that coupling between flap and lead-lag motion will be destabilizing if it tends to align blade motions with the $(\theta + \phi)/2$ axis. One effect that can produce such a coupling is the amount of elastic (structural) coupling between flap and lead-lag. This effect is represented mathematically by the off-diagonal terms of the stiffness matrix. For small pitch angles, the stiffness matrix of the spring model in reference 1 may be approximated by

$$[K] = \begin{bmatrix} p^2 & \Delta \\ \Delta & \omega_\zeta^2 \end{bmatrix} \tag{10}$$

where

$$\left. \begin{aligned} \Delta &\simeq R\theta(\omega_\zeta^2 - p^2 + 1) \\ 0 &\leq R \leq 1 \end{aligned} \right\} \tag{11}$$

and R is an elastic coupling parameter. For this discussion Δ need not be restricted to this form, and in a later section the effects of pitch-flap and pitch-lag coupling on the stiffness matrix will be considered.

Because of the elastic coupling Δ, the natural vibrations for the blade rotating in a vacuum will be inclined with respect to the lead-lag plane by an angle δ_m, as shown in figure 4. For small Δ and $\omega_\zeta \neq p$, this angle is given by

$$\delta_m = \frac{\Delta}{\omega_\zeta^2 - p^2} \tag{12}$$

8

134

The inclination of the mode in a vacuum δ_m is not generally equivalent to the inclination of the mode including aerodynamics δ. For the special case of $\delta_m = (\theta + \phi)/2$ and $[G] = 0$, however, aerodynamic coupling is eliminated and δ does equal δ_m. Thus, the least stable condition occurs when δ and δ_m are aligned with the $(\theta + \phi)/2$ axis

$$\Delta\Big|_{\text{least stable}} = \frac{(\omega_\zeta^2 - p^2)(\theta + \phi)}{2} \tag{13}$$

For example, the least stable condition for the approximation in equation (11) is

$$R\Big|_{\text{least stable}} = \frac{\left(1 + \dfrac{\phi}{\theta}\right)(\omega_\zeta^2 - p^2)}{2(\omega_\zeta^2 - p^2 + 1)} \tag{14}$$

A similar result that was obtained in reference 1 from Routh's criteria, is that the smallest $(\theta - \phi)$ for instability occurs when equation (14) is satisfied.

A quantitative expression for the relation between elastic coupling and blade damping can be obtained by applying the mode shape component ϕ_β, equation (4b), to the damping expression in equation (9b). Assuming again that $[G] = 0$, ϕ_β is given by

$$\phi_\beta = \delta + i\varrho = \frac{\theta + \phi}{2} + \frac{\left[\Delta - \dfrac{\theta + \phi}{2}(\omega_\zeta^2 - p^2)\right]}{(\omega_\zeta^2 - p^2)^2 + \left(\dfrac{\gamma}{8}\omega_\zeta\right)^2}\left[(\omega_\zeta^2 - p^2) + i\frac{\gamma}{8}\omega_\zeta\right] \tag{15}$$

Equation (15) shows that an inclination of the modal axis δ_m with respect to the $(\theta + \phi)/2$ axis results in elliptical blade motions. An expression for the lead-lag damping can be obtained by substituting equation (15) into equation (9b).

$$-\frac{16}{\gamma}\eta = 2\frac{C_{d_0}}{a} - \frac{(\theta - \phi)^2}{4} + \frac{\left[\Delta - \dfrac{\theta + \phi}{2}(\omega_\zeta^2 - p^2)\right]^2}{(\omega_\zeta^2 - p^2)^2 + \left(\dfrac{\gamma}{8}\omega_\zeta\right)^2} \tag{16}$$

Equation (16) contains two components of damping: (1) the minimal possible damping $2(C_{d_0}/a) - (\theta - \phi)^2/4$, and (2) the stabilizing effect of separating the δ_m axis and the $(\theta + \phi)/2$ axis. Equation (16) also shows that above or below certain critical values of Δ (or δ_m) no instability is possible. The blade motion is always stable when

$$\left|\frac{\Delta}{\omega_\zeta^2 - p^2} - \frac{\theta + \phi}{2}\right| > \frac{\theta - \phi}{2}\sqrt{1 + \left(\frac{\dfrac{\gamma}{8}\omega_\zeta}{\omega_\zeta^2 - p^2}\right)^2}$$

9

This is illustrated in figure 5 which indicates regions of possible instability when $p = \sqrt{4/3}$, $\gamma = 8$. Instabilities are only possible when the modal axis δ_m is sufficiently close to the $(\theta + \phi)/2$ axis, and the least stable condition occurs when $\delta_m = (\theta + \phi)/2$. At $\omega_\zeta = p$, the definition for δ_m breaks down and instabilities appear to be possible at all values of δ_m. In terms of Δ at $\omega_\zeta = p$, however, instabilities are only possible when

$$|\Delta| < \frac{\gamma}{16} (\theta - \phi)\omega_\zeta$$

The least stable condition occurs when $\Delta = 0$.

Also shown in figure 5 are lines of constant R in the δ_m, $\omega_\zeta^2 - p^2$ plane. For $\phi/\theta < R < 1$, instabilities can only occur when ω_ζ is above a critical value. For R values in the upper half of this region, $[1 + (\phi/\theta)]/2 < R < 1$, the least stable condition $\delta_m = (\theta + \phi)/2$ is never obtained; but in the lower half of the region, $\phi/\theta < R < [1 + (\phi/\theta)]/2$, the least stable condition is obtained for some finite value of ω_ζ. For $R < \phi/\theta$, instabilities can only occur when ω_ζ lies between upper and lower critical values.

When $\theta + \phi$ and $\theta - \phi$ are positive, which is the case for hover or axial flight, instabilities are not possible for sufficiently soft inplane rotors with $0 < R < 1$. Blade motion is always stable when

$$p^2 - \omega_\zeta^2 > \frac{\gamma}{16} \omega_\zeta \frac{\theta - \phi}{\sqrt{\theta\phi}}$$

Thus, most physically realistic soft inplane configurations are stable in hover. When $\theta + \phi$ is negative, however, such as is the case in autorotation conditions, the stability boundaries in figure 5 will move down with respect to the constant R contours; and potential instabilities can occur for some realistic soft inplane configurations, $\omega_\zeta < p$.

CORIOLIS COUPLING

Another effect that can couple flap and lead-lag motion is the Coriolis matrix [G]. From equation (1), this matrix is given by

$$[G] = \begin{bmatrix} 0 & \vdots & 2\beta_0 - \frac{3\gamma}{16}(\theta - \phi) \\ \cdots & \vdots & \cdots \\ -2\beta_0 + \frac{3\gamma}{16}(\theta - \phi) & \vdots & 0 \end{bmatrix} \tag{17}$$

10

where β_0 is the equilibrium coning angle. To the order considered in this paper, β_0 is

$$\beta_0 = \frac{p^2 - 1}{p^2} \beta_{pc} + \frac{\gamma}{8p^2} (\theta - \phi) \qquad (18)$$

where β_{pc} is the blade precone. The β_0 portion of [G] is the gyroscopic Coriolis term due to rotational effects. The $(3\gamma/16)(\theta - \phi)$ portion of [G] is an apparent Coriolis term due to the conservative portion of the aerodynamic coupling.

The matrix [G] is antisymmetric and is, therefore, unaffected by coordinate transformations. Thus, [G] will alter the response even when the model axis is aligned with the $(\theta + \phi)/2$ axis. In terms of the instability mechanism described earlier, the blade motion is least stable when [G] = 0 and the coupling is minimized. From equations (17) and (18), this condition occurs when

$$\left.\begin{array}{l} \beta_0 = \dfrac{3}{32} \gamma (\theta - \phi) \\[3mm] \beta_{pc} = \dfrac{\gamma}{8} (\theta - \phi) \dfrac{3p^2 - 4}{4(p^2 - 1)} \end{array}\right\} \qquad (19)$$

For $\beta_{pc} = 0$, the minimum damping condition becomes $p = \sqrt{4/3}$ for all values of $(\theta - \phi)$. This same result was obtained in reference 1 using a different method. Thus, the least stable condition occurs when all Coriolis coupling is eliminated by the equilibrium coning.

The quantitative increase in damping when β_{pc} is not given by equation (19) can be found from the contribution of [G] to the mode shape ϕ_β, equation (4b).

$$\phi_\beta \bigg|_{\text{due to [G]}} = \omega_\zeta \frac{\left[2\beta_0 - \frac{3\gamma}{16} (\theta - \phi)\right]}{(\omega_\zeta^2 - p^2)^2 + \left(\frac{\gamma}{8} \omega_\zeta\right)^2} \left[- \frac{\gamma}{8} \omega_\zeta + i(\omega_\zeta^2 - p^2)\right] \qquad (20)$$

The contribution to ϕ_β given in equation (20) may be added directly to the contribution in equation (15) because β_0, θ, and ϕ are small quantities. Substitution of the combined mode into equation (9b) gives the contribution of the Coriolis terms to the blade damping.

$$-\frac{16}{\gamma} \eta \bigg|_{\text{due to [G]}} = + \frac{\omega_\zeta^2 \left[2\beta_0 - \frac{3\gamma}{16} (\theta - \phi)\right]^2}{(\omega_\zeta^2 - p^2)^2 + \left(\frac{\gamma}{8} \omega_\zeta\right)^2} \qquad (21)$$

11

137

Of course this damping is only indirectly due to the conservative Coriolis forces and is a direct result of the flap damping. An interesting fact is that the damping due to [G] and the damping due to [K] are uncoupled. This is because the mode shape contributions of [K] and [G] are orthogonal. Each effect provides positive damping independent of the other, and neither of the terms can provide negative damping to cancel the effect of the other.

As in the case with elastic coupling, there is a range of Coriolis coupling for which the mode shape is so far from the $(\theta + \phi)/2$ axis that no instability is possible. From equations (16) and (21), this condition is

$$\left| \frac{16}{\gamma} \beta_0 - \frac{3}{2} (\theta - \phi) \right| > \frac{\theta - \phi}{2} \sqrt{1 + \frac{(\omega_\zeta^2 - p^2)^2}{\left(\frac{\gamma}{8} \omega_\zeta\right)^2}} \tag{22a}$$

For the special cases $\Delta = 0$ or $\omega_\zeta = p$, a more restrictive criterion is obtained.

$$\left| \frac{16}{\gamma} \beta_0 - \frac{3}{2} (\theta - \phi) \right| > \frac{\theta - \phi}{2} \tag{22b}$$

This formula can be written in terms of β_{pc} and p^2 from equation (18). Thus, for $p^2 > 1$, no instability is possible for

$$\left. \begin{array}{l} \beta_{pc} > \frac{\gamma}{8} (\theta - \phi) \\[3mm] \beta_{pc} < \frac{\gamma}{16} (\theta - \phi) \frac{p^2 - 2}{p^2 - 1} \end{array} \right\} \tag{23}$$

Figure 6 shows the regions for which no instabilities are possible when $\Delta(\omega_\zeta^2 - p^2) = 0$. Also shown is the contour of the least stable condition, equation (19). When $\Delta(\omega_\zeta^2 - p^2) \neq 0$, the area of possible instabilities is slightly enlarged. Thus, the Coriolis matrix [G] is a stabilizing influence. The least stable condition is [G] = 0 and, for sufficiently large [G], no instabilities are possible.

The damping expression, including elastic and Coriolis coupling terms, can be written from equations (16) and (21).

$$\eta = -\frac{\gamma}{16} \left[2 \frac{C_{do}}{a} - \frac{(\theta - \phi)^2}{4} \right]$$
$$-\frac{\gamma}{16} \frac{(\omega_\zeta^2 - p^2)^2 \left(\frac{\Delta}{\omega_\zeta^2 - p^2} - \frac{\theta + \phi}{2} \right)^2 + \left(\frac{\gamma}{8} \omega_\zeta \right)^2 \left[\frac{16}{\gamma} \beta_0 - \frac{3}{2} (\theta - \phi) \right]^2}{(\omega_\zeta^2 - p^2)^2 + \left(\frac{\gamma}{8} \omega_\zeta \right)^2} \tag{24}$$

12

Equation (24) shows that curves of constant damping form ellipses in the $(16/\gamma)\beta_0$, $\Delta/(\omega_\zeta^2 - p^2)$ plane. For example, the family of ellipses having only profile drag damping, $\eta = -(\gamma/8)(C_{d_0}/a)$, is illustrated in figure 7. The thickness ratio of each ellipse in this family is $(\gamma/8)\omega_\zeta/(\omega_\zeta^2 - p^2)$. Every ellipse also passes through the same four points,

$$\frac{16}{\gamma} \beta_0 = (\theta - \phi), \; 2(\theta - \phi)$$

$$\delta_m = \frac{\Delta}{\omega_\zeta^2 - p^2} = \phi, \; \theta$$

and no ellipse contains any of the four shaded areas. Thus, the area outside of the unshaded cross is always stable.

PITCH-FLAP AND PITCH-LAG COUPLING

Pitch-flap coupling θ_β and pitch-lag coupling θ_ζ are parameters that describe the pitching motion of the rotor blade due to flap or lead-lag deflections.

$$\delta\theta = \theta_\beta\beta + \theta_\zeta\zeta \tag{25}$$

These parameters are defined so that positive flap (upward) and positive lead-lag (forward) motion produce positive pitch. Their effect on the flap-lag equations is seen in the stiffness matrix from equation (1)

$$[K] = \begin{bmatrix} p^2 - \frac{\gamma}{8}\theta_\beta & \vdots & \Delta - \frac{\gamma}{8}\theta_\zeta \\ - - - - - - & \vdots & - - - - - \\ \Delta - \frac{\gamma}{8}\bar{\theta}_\beta & \vdots & \omega_\zeta^2 \end{bmatrix} \tag{26}$$

where $\bar{\theta}_\beta \equiv [\theta + (8/\gamma)(\beta_0 - \beta_{pc})\Delta_\theta]\theta_\beta$. The effect of θ_β on the K_{11} term is usually treated by defining an equivalent flapping frequency

$$\bar{p}^2 \equiv p^2 - \frac{\gamma}{8}\theta_\beta$$

It should be noted, however, that the equilibrium formula, equation (18), is still valid in its present form in terms of p^2 and $(\theta - \phi)$. It may be rewritten, however, in terms of $\bar{p}^2$ and $(\theta_0 - \phi)$.

13

$$\beta_O = \frac{\bar{p}^2 - 1}{\bar{p}^2} \beta_{pc} + \frac{\gamma}{8\bar{p}^2} (\theta_O - \phi)$$

The coefficients in equation (1) must be expressed in terms of the total equilibrium pitch angle, $\theta = \theta_O + \theta_\beta(\beta_O - \beta_{pc})$. Thus, pitch-flap coupling affects the blade dynamics by changing the flapping frequency and the blade equilibrium.

Another effect of θ_β and θ_ζ is the coupling produced in the off-diagonal terms K_{12} and K_{21}. First, the pitch-lag coupling θ_ζ changes the mode shape by altering K_{12}, equation (4b). This effect can be included in the analysis by replacing Δ with $\Delta - (\gamma/8)\theta_\zeta$ in equation (24). A second effect of θ_ζ and θ_β is that they produce an asymmetric or nonconservative stiffness matrix. The energy dissipated or added by this asymmetry can be approximated by integrating the dot product of force and distance around a closed path, figure 8. The integration yields

$$\text{Energy dissipated} = \oint (F_1 \, dx_1 + F_2 \, dx_2)$$

$$= \oint (K_{11}x_1 \, dx_1 + K_{22}x_2 \, dx_2 + K_{12}x_2 \, dx_1 + K_{21}x_1 \, dx_2)$$

$$= \oint \left[K_{11} \, d\left(\frac{1}{2} x_1^2\right) + K_{22} \, d\left(\frac{1}{2} x_2^2\right) + K_{12}(x_2 \, dx_1) + K_{21}(x_1 \, dx_2) \right]$$

The energy dissipated can be evaluated from the following relations: (1) the integral around a closed contour of a perfect differential is zero, (2) the integration of $x_1 \, dx_2$ is the area enclosed within the contour, and (3) the integration of $x_2 \, dx_1$ is the negative of the enclosed area.

$$\text{Energy dissipated} = (K_{21} - K_{12}) \text{ (enclosed area)} \tag{27}$$

The area is taken as positive for integration in a clockwise direction. Thus, the nonconservative or antisymmetric portion of [K] may either dissipate or add energy.

For the particular case of flap-lag dynamics, the enclosed area is approximated by the area of the ellipse of motion $\rho\pi$; and the antisymmetric stiffness term is $K_{21} - K_{12} = (\gamma/8)(\bar{\theta}_\beta + \theta_\zeta)$. Thus, the damping contribution due to the nonconservative terms is

$$\eta\big|_{\text{nonconservative stiffness}} = -\frac{\text{Energy dissipated}}{2\pi\omega_\zeta} = -\frac{\gamma}{16} \frac{\rho}{\omega_\zeta} (\bar{\theta}_\beta + \theta_\zeta) \tag{28}$$

14

Thus, energy is either added or dissipated depending on the sign of $\bar{\theta}_\beta + \theta_\zeta$ and the sense of the motion ($\rho > 0$ clockwise, $\rho < 0$ counterclockwise). By taking $\Delta = \Delta - (\gamma/8)\omega_\zeta$ in equations (24) and (4b), and adding the nonconservative stiffness contribution from equation (28), one obtains the complete expression for lead-lag damping, where $\eta = \operatorname{Re} \in$

$$-\frac{16}{\gamma}\eta = \left[2\frac{c_{d_0}}{a} - \frac{(\theta - \phi)^2}{(2)^2}\right] + \frac{\left[\Delta - \frac{\theta + \phi}{2}(\omega_\zeta^2 - \bar{p}^2)\right]^2 + \omega_\zeta^2\left[2\beta_0 - \frac{3\gamma}{16}(\theta - \phi)\right]^2}{(\omega_\zeta^2 - \bar{p}^2)^2 + \left(\frac{\gamma}{8}\omega_\zeta\right)^2}$$

$$+ \frac{\frac{\gamma}{8}(\bar{\theta}_\beta - \theta_\zeta)\left[\Delta - \frac{\theta + \phi}{2}(\omega_\zeta^2 - \bar{p}^2)\right] + (\bar{\theta}_\beta + \theta_\zeta)(\omega_\zeta^2 - \bar{p}^2)\left[2\beta_0 - \frac{3\gamma}{16}(\theta - \phi)\right] - \left(\frac{\gamma}{8}\right)^2\bar{\theta}_\beta\theta_\zeta}{(\omega_\zeta^2 - \bar{p}^2)^2 + \left(\frac{\gamma}{8}\omega_\zeta\right)^2}$$

$$(29)$$

The second line of equation (29) represents the effect of pitch-flap and pitch-lag coupling on blade damping.

The effect of pitch-flap coupling is entirely due to the nonconservative terms. Thus, for clockwise motion in the x_1, x_2 plane, positive $\bar{\theta}_\beta$ is stabilizing. Equations (15) and (20) show that the motion is clockwise when $\rho > 0$ or

$$(\omega_\zeta^2 - \bar{p}^2)\left\{\left[\frac{\Delta - \frac{\gamma}{8}\theta_\zeta}{\omega_\zeta^2 - \bar{p}^2} - \frac{\theta + \phi}{2}\right] + \left[\frac{16}{\gamma}\beta_0 - \frac{3}{2}(\theta - \phi)\right]\right\} > 0 \qquad (30)$$

which agrees with equation (29). This effect is illustrated in figure 9. There is a straight line that divides the $\bar{\delta}_m$, $(16/\gamma)\beta_0$ plane into two regions in which blade motions are either clockwise or counterclockwise. Along this straight line boundary $\rho = 0$ and blade motions enclose no area. Thus, on this boundary pitch-flap coupling has no effect. Of interest is the fact that the minimum damping point with $\theta_\beta = \theta_\zeta = 0$ is on this boundary and also represents a condition unaffected by θ_β.

For pitch-lag coupling, there are nonconservative stiffness terms and elastic coupling terms that affect the damping. When both effects are included, the boundary between stabilizing and destabilizing regions is a straight line in the $\bar{\delta}_m$, $(16/\gamma)\beta_0$ plane. This effect is illustrated in figure 10 which gives the total effect of θ_ζ on blade damping except for the $\theta_\zeta\theta_\beta$ coupling effect already treated in equation (30). The boundary between the stabilizing and destabilizing regions is perpendicular to the θ_β boundary in figure 9 and passes through the same minimum damping point. Thus, at the condition of minimum damping with $\theta_\beta = \theta_\zeta = 0$, there is no effect of θ_β or θ_ζ alone, although there is a coupling effect if θ_β and θ_ζ are included together. There are, therefore, three factors that can change the effect of

15

θ_β or θ_ζ from stabilizing to destabilizing or vice versa: (1) the sign of $\bar{\theta}_\beta$ or θ_ζ, (2) the sign of $(\omega_\zeta^2 - \bar{p}^2)$, and (3) the region (i.e., half-plane) in which $(16/\gamma)\beta_o$ and δ_m (or $\bar{\delta}_m$) lie.
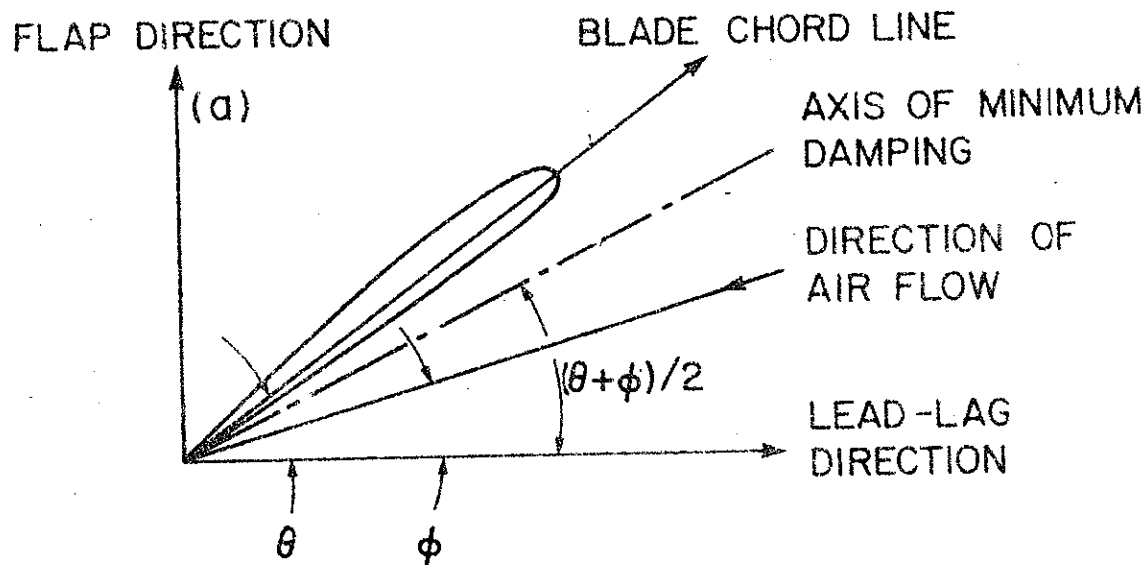
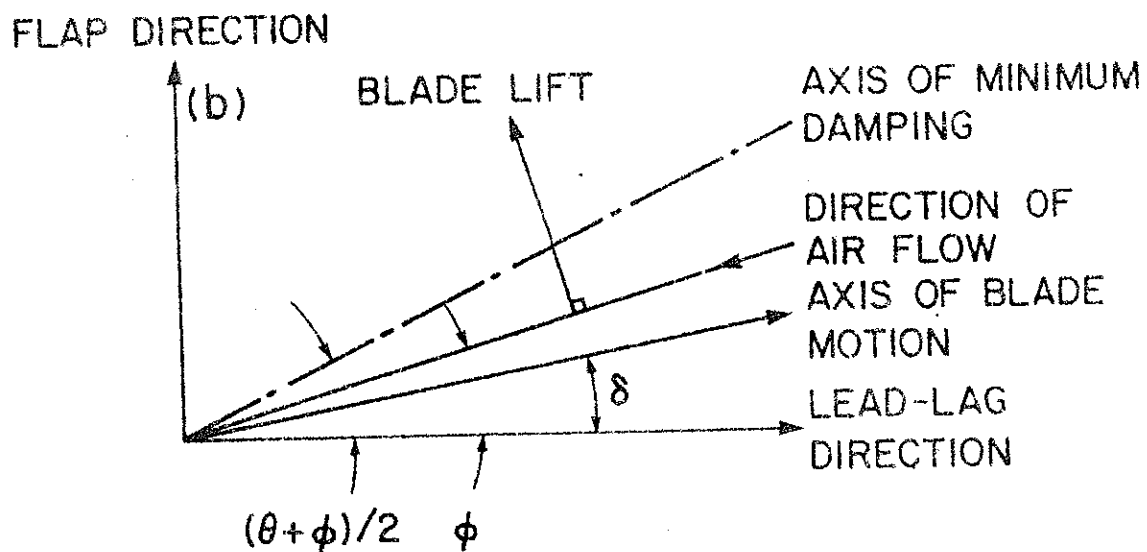## CONCLUSIONS

The following conclusions may be drawn from this analysis.

1. The destabilizing effect of aerodynamic forces that can occur when $(\theta - \phi) > 2\sqrt{2(C_{d_o}/a)}$ is maximum when the blade motion is in a straight line along the $(\theta + \phi)/2$ axis.

2. Coriolis and elastic coupling can move the mode shape with respect to the $(\theta + \phi)/2$ axis and thereby influence the blade stability.

3. The least stable condition occurs when the Coriolis terms are zero and when the elastic coupling terms align the rotating mode shape in a vacuum with the $(\theta + \phi)/2$ axis.

4. Pitch-lag coupling produces a change in the equivalent elastic axis, and pitch-flap and pitch-lag coupling introduce nonconservative stiffness terms that stabilize or destabilize the blade motion depending upon whether the motion is clockwise or counterclockwise.

REFERENCES

1. Ormiston, R. A. and Hodges, D. H.: Linear Flap-Lag Dynamics of Hingeless Helicopter Rotor Blades in Hover. J. American Helicopter Soc., vol. 17, no. 2, April 1972.

2. Zajac, E. E.: The Kelvin-Tait-Chetaev Theorem and Extensions. J. Astronaut. Sci., vol. 11, no. 2, Summer, 1964, pp. 46-49.

142

FLAP DIRECTION   BLADE CHORD LINE

(a)

AXIS OF MINIMUM DAMPING

DIRECTION OF AIR FLOW

$(\theta+\phi)/2$

LEAD-LAG DIRECTION

θ ϕ

(a) Motion geometry.

FLAP DIRECTION

(b)   BLADE LIFT

AXIS OF MINIMUM DAMPING

DIRECTION OF AIR FLOW

AXIS OF BLADE MOTION

δ

LEAD-LAG DIRECTION

$(\theta+\phi)/2$ ϕ

(b) Force geometry.

Figure 1.- Geometry of blade motion and aerodynamic force.

17

143
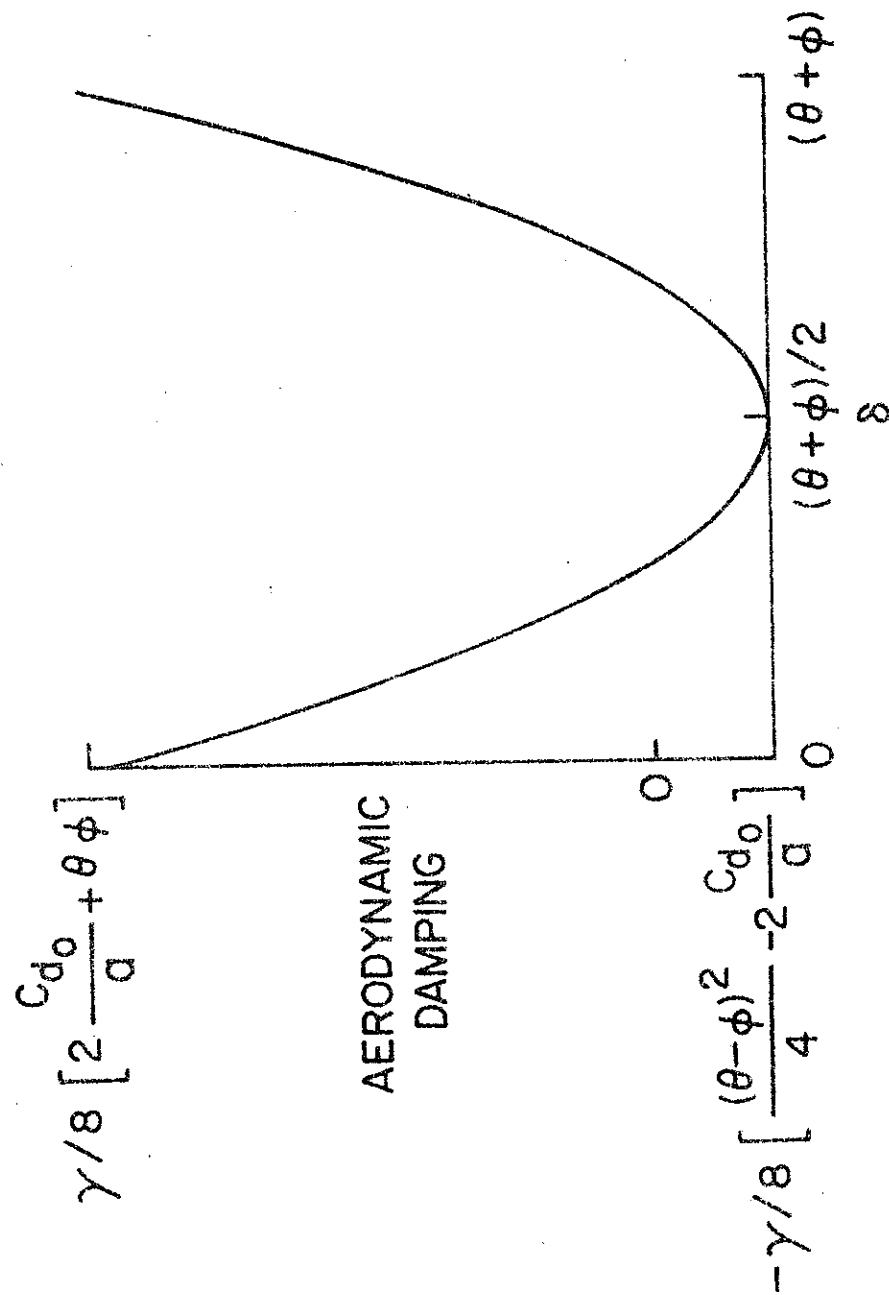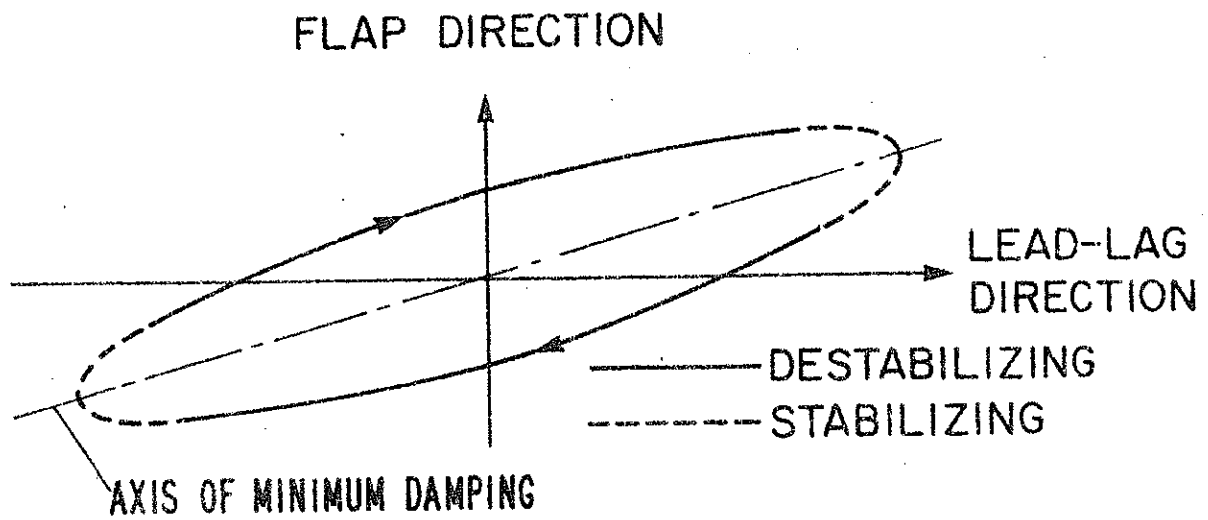
Figure 2.- Aerodynamic damping coefficient for motion in δ direction.

FLAP DIRECTION

LEAD–LAG DIRECTION

——————— DESTABILIZING

— — — — — STABILIZING

AXIS OF MINIMUM DAMPING

Figure 3.- Elliptical blade motions.

FLAP DIRECTION

δ_m

LEAD–LAG DIRECTION

DIRECTION OF NATURAL VIBRATIONS IN VACUUM
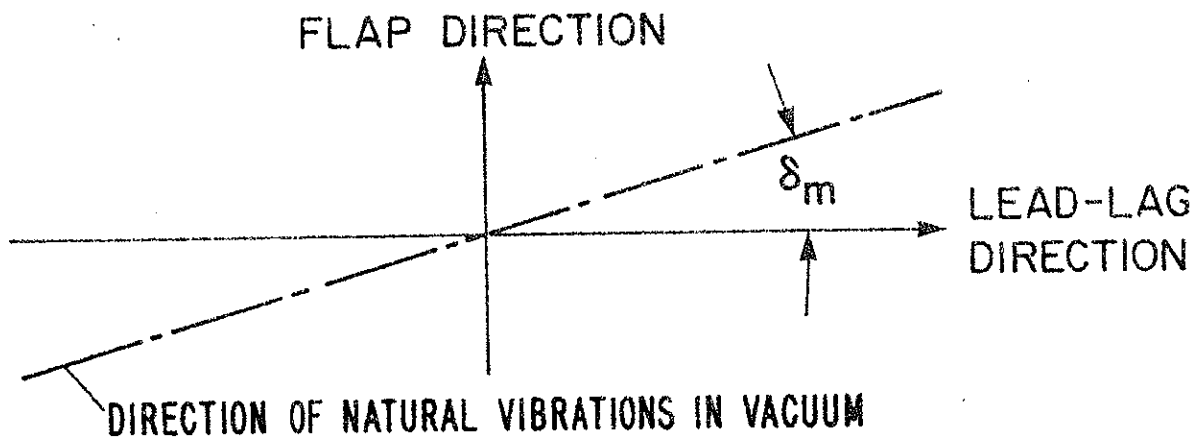
Figure 4.- Rotating mode shape in vacuum.

19
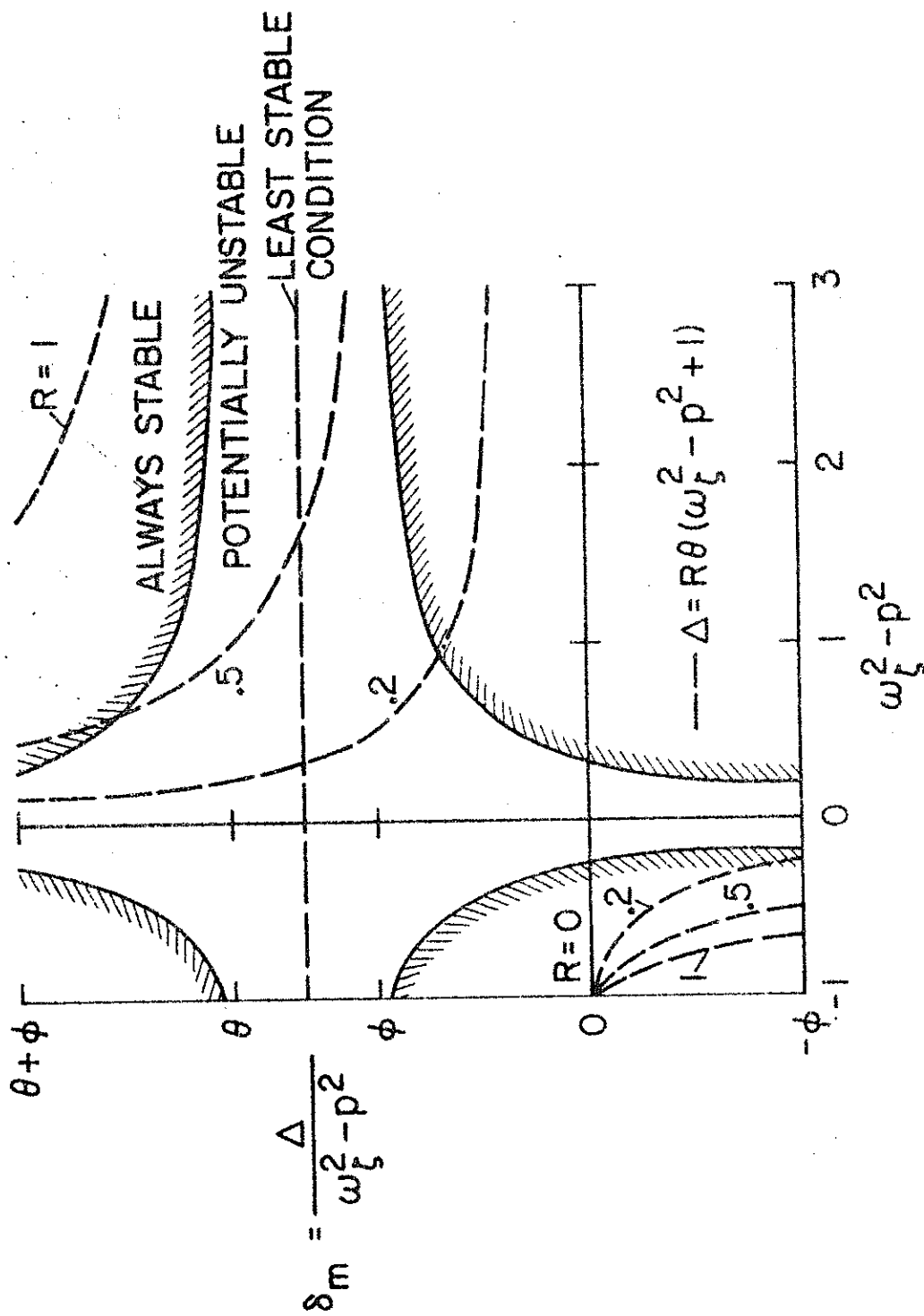
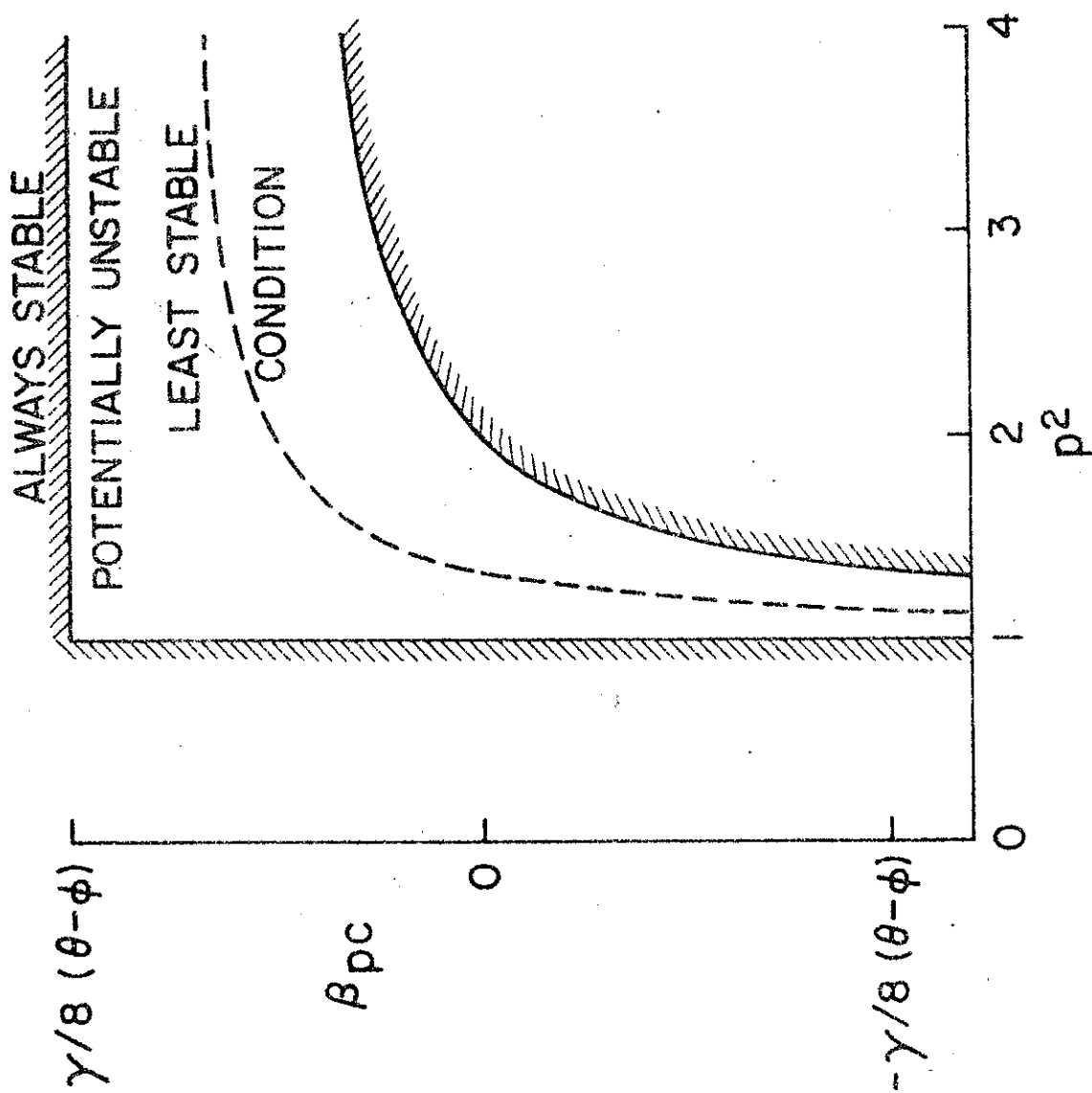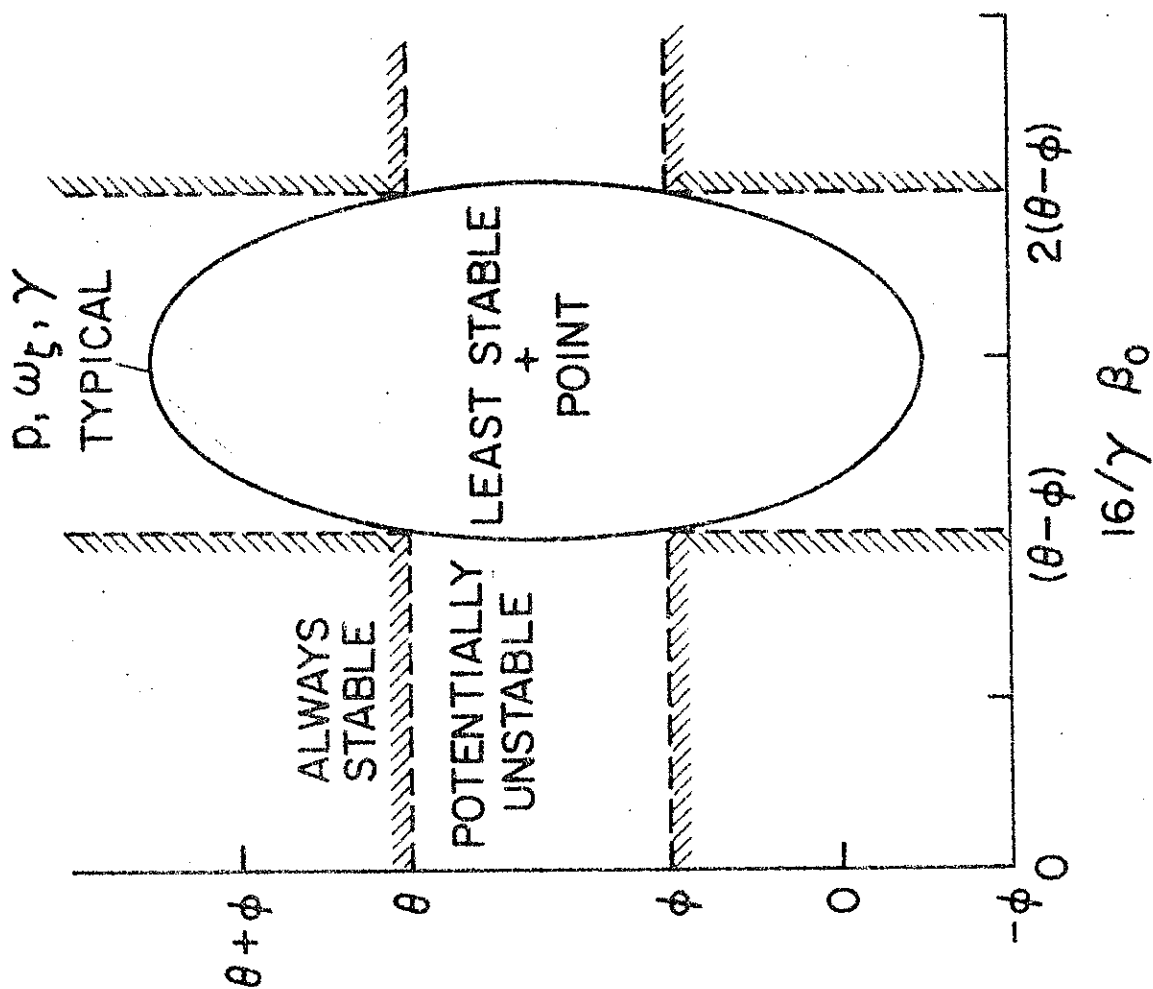Figure 5.- Effect of elastic coupling on regions of potentially unstable motion, $\gamma = 8$, $p = \sqrt{4/3}$. No pitch coupling.

Figure 6.- Effect of Coriolis coupling when $\Delta(\omega_\zeta^2 - p^2) = 0$. No pitch coupling.

Figure 7.- Ellipse of constant damping $n = -(\gamma/8)(C_{d_0}/a)$, and regions of potentially unstable motion. No pitch coupling.
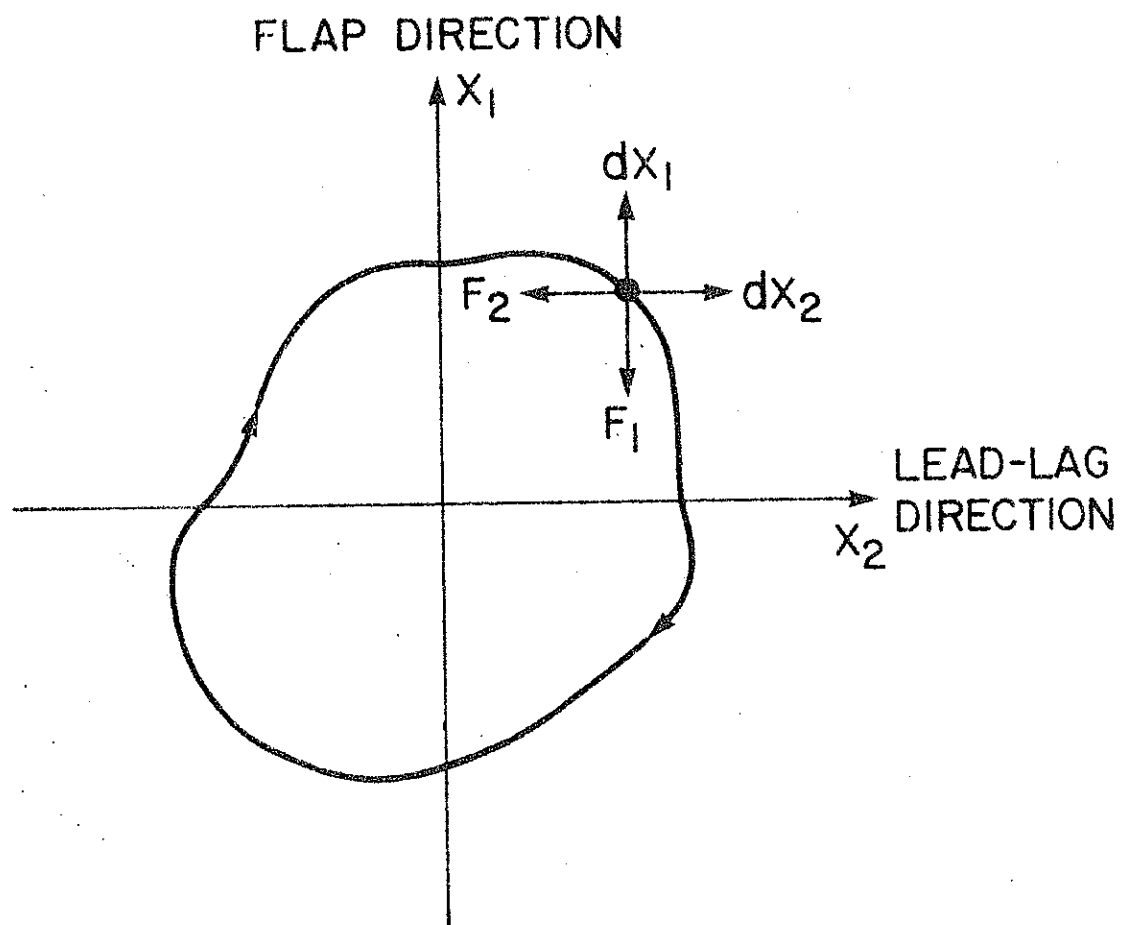
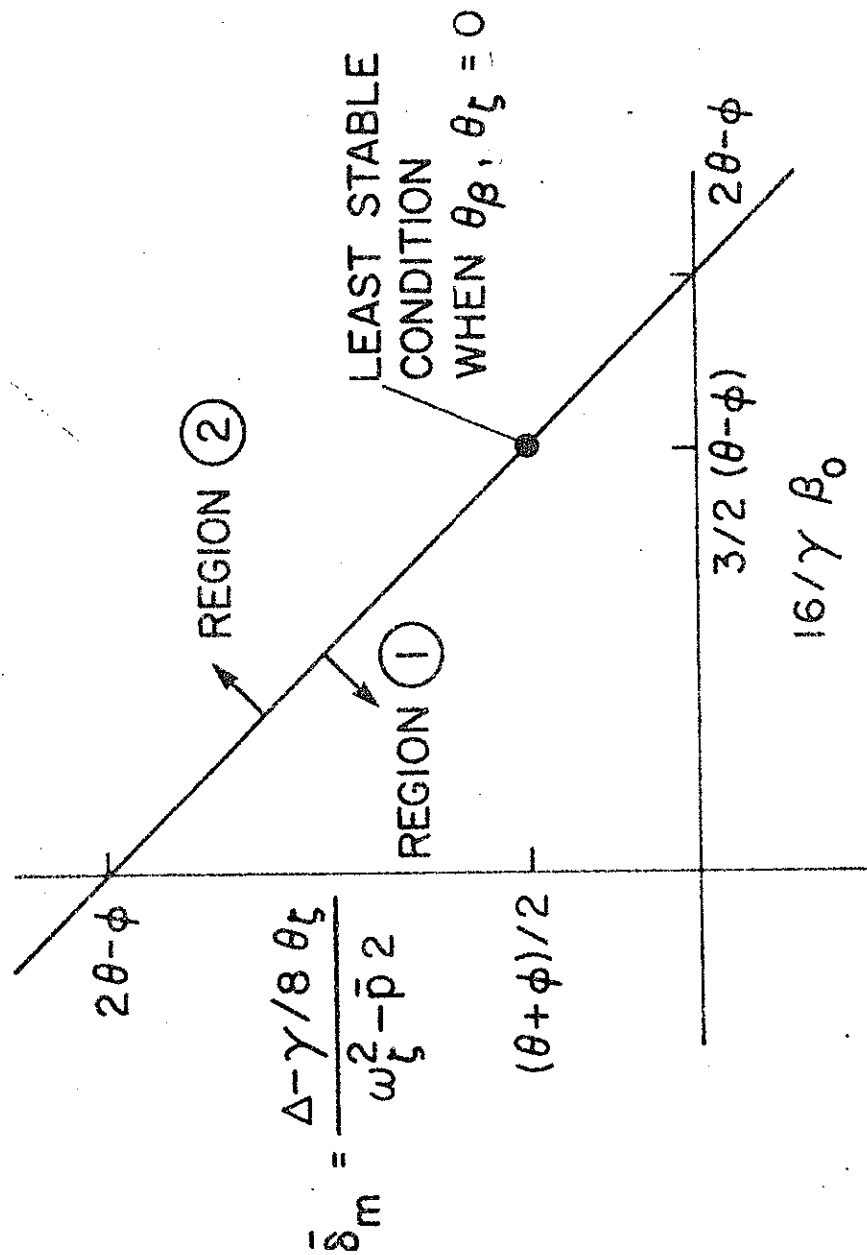Figure 8.- Energy dissipated for motion around a closed contour.

Figure 9.- Effect of pitch-flap coupling. Blade motion is destabilized in region $\left\{\begin{array}{c}①\\②\end{array}\right\}$ when $(\omega_\zeta^2 - \bar{p}^2)\bar{\theta}_\beta \left\{\begin{array}{c}>0\\<0\end{array}\right\}$.
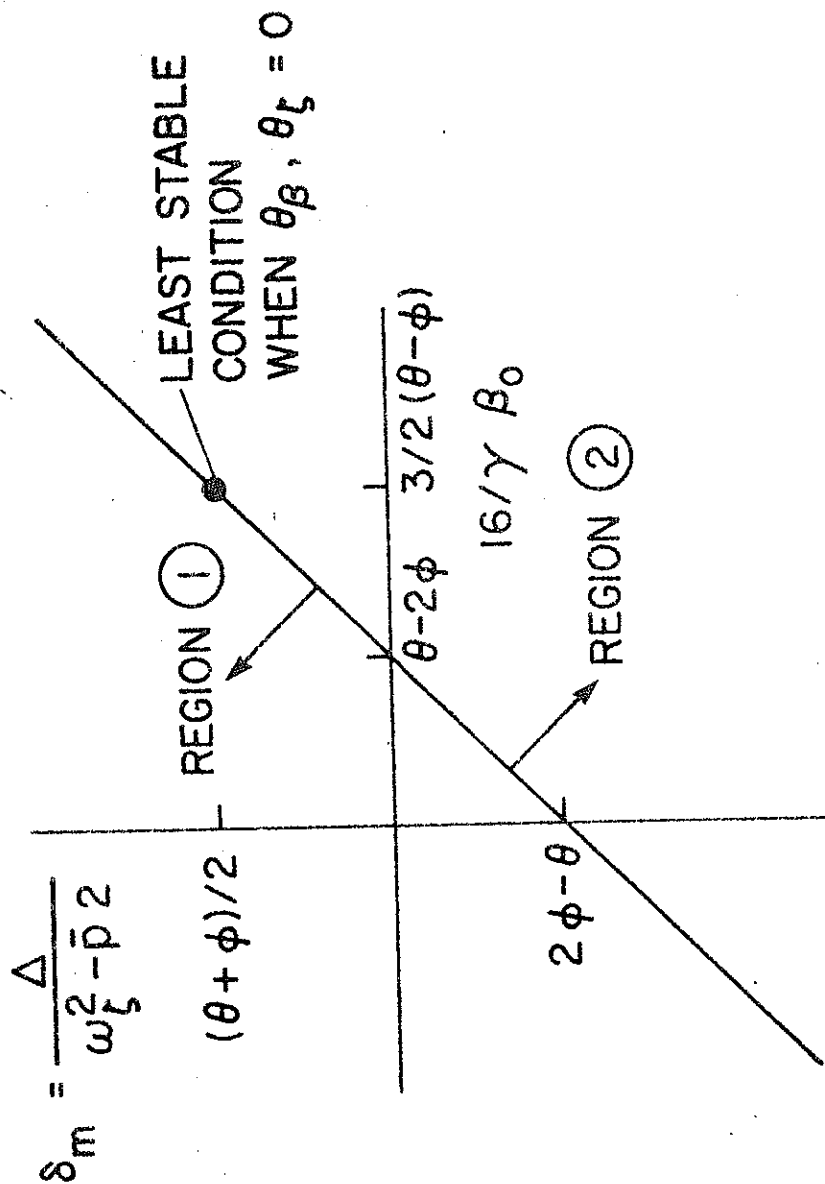
Figure 10.- Effect of pitch-lag coupling. Blade motion is destabilized in region $\left\{\begin{matrix} \textcircled{1} \\ \textcircled{2} \end{matrix}\right\}$ when $(\omega_\zeta^2 - \bar{p}^2)\theta_\zeta \left\{\begin{matrix} >0 \\ <0 \end{matrix}\right\}$.